AD-A218 497

A LINEAR ANALYSIS OF MONSOON BASE STATES

ASSOCIATED WITH BANDED CONVECTION

DTIC
S **ELECTE**
FEB 2 3 1990
D
D

John Russell Roadcap, B.S., M. Pr. Met.

A Digest Presented to the Faculty of the Graduate
School of Saint Louis University in Partial
Fulfillment of the Requirements for the
Degree of Doctor of Philosophy

1989

90 02 21 089

REPORT DOCUMENTATION PAGE

1a. REPORT SECURITY CLASSIFICATION UNCLASSIFIED		1b. RESTRICTIVE MARKINGS NONE
2a. SECURITY CLASSIFICATION AUTHORITY		3. DISTRIBUTION / AVAILABILITY OF REPORT APPROVED FOR PUBLIC RELEASE; DISTRIBUTION UNLIMITED.
2b. DECLASSIFICATION / DOWNGRADING SCHEDULE		
4. PERFORMING ORGANIZATION REPORT NUMBER(S)		5. MONITORING ORGANIZATION REPORT NUMBER(S) AFIT/CI/CIA- 89-042

6a. NAME OF PERFORMING ORGANIZATION AFIT STUDENT AT SAINT LOUIS UNIVERSITY	6b. OFFICE SYMBOL (If applicable)	7a. NAME OF MONITORING ORGANIZATION AFIT/CIA
6c. ADDRESS (City, State, and ZIP Code)		7b. ADDRESS (City, State, and ZIP Code) Wright-Patterson AFB OH 45433-6583
8a. NAME OF FUNDING / SPONSORING ORGANIZATION	8b. OFFICE SYMBOL (If applicable)	9. PROCUREMENT INSTRUMENT IDENTIFICATION NUMBER

8c. ADDRESS (City, State, and ZIP Code)	10. SOURCE OF FUNDING NUMBERS			
	PROGRAM ELEMENT NO.	PROJECT NO.	TASK NO.	WORK UNIT ACCESSION NO.

11. TITLE (Include Security Classification) (UNCLASSIFIED)
A Linear Analysis of Monsoon Base States Associated with Banded Convection

12. PERSONAL AUTHOR(S)
John Russell Roadcap

13a. TYPE OF REPORT THESIS/DISSERTATION	13b. TIME COVERED FROM _____ TO _____	14. DATE OF REPORT (Year, Month, Day) 1989	15. PAGE COUNT 252

16. SUPPLEMENTARY NOTATION APPROVED FOR PUBLIC RELEASE IAW AFR 190-1
ERNEST A. HAYGOOD, 1st Lt, USAF
Executive Officer, Civilian Institution Programs

17. COSATI CODES			18. SUBJECT TERMS (Continue on reverse if necessary and identify by block number)
FIELD	GROUP	SUB-GROUP	

19. ABSTRACT (Continue on reverse if necessary and identify by block number)

20. DISTRIBUTION / AVAILABILITY OF ABSTRACT ☒ UNCLASSIFIED/UNLIMITED ☐ SAME AS RPT. ☐ DTIC USERS	21. ABSTRACT SECURITY CLASSIFICATION UNCLASSIFIED	
22a. NAME OF RESPONSIBLE INDIVIDUAL ERNEST A. HAYGOOD, 1st Lt, USAF	22b. TELEPHONE (Include Area Code) (513) 255-2259	22c. OFFICE SYMBOL AFIT/CI

A LINEAR ANALYSIS OF MONSOON BASE STATES

ASSOCIATED WITH BANDED CONVECTION

John Russell Roadcap, B.S., M. Pr. Met.

A Dissertation Presented to the Faculty of the Graduate
School of Saint Louis University in Partial
Fulfillment of the Requirements for the
Degree of Doctor of Philosophy

1989

A-1

DIGEST

The response of a linearized system of anelastic perturbation equations to varied wind, temperature, moisture, and diabatic heating profiles representative of base states found during the Arabian Sea monsoon is investigated as an eigenvalue problem. The diabatic heating profile for deep convection is parameterized using the Anthes scheme which is driven by a 1DSS cloud model. Shallow non-precipitating convection is parameterized using the Betts two layer cloud model. The base state wind profiles are fit with a least squares curve whose order may vary. Eddy diffusion coefficients are determined from the cloud model using a Smagorinsky-Lilly type formulation. Moisture is accessed into the linear model via either boundary layer moisture accession or the vertically- integrated advection over the cloud depth. Sensible warming, a consequence of environmental subsidence, and cooling in the cloud layer below 2 km, a result of the moist downdrafts, are included in the calculations.

Results suggest the shapes of the convective heating and horizontal wind profiles are crucial in determining the onset of the longitudinal stationary mode as the precipitation efficiency is increased. Stationary longitudinal modes are associated with a minimum of flux Richardson number in the wavenumber domain. Including sensible heat transports in the cumulus

1

2

parameterization shifts the convective heating maximum to a higher level and delays the onset of the stationary mode. The stationary mode onset (critical point) is characterized by sharp reductions in the flux Richardson number and phase speed for the longitudinal mode. For deep convection, the shear-parallel momentum flux remains down-gradient through the stationary mode onset while the shear-perpendicular momentum flux becomes up-gradient at the onset of the stationary mode. Analysis of the energy transfer spectra suggests that kinetic energy conversion is down-scale for both longitudinal and transverse modes prior to the critical point but becomes up-scale for transverse modes after the onset of stationarity.

COMMITTEE IN CHARGE OF CANDIDACY:

Professor Gandikota V. Rao,
    Chairperson and Advisor

Assistant Professor Lawrence Coy

Professor Yeong-Jer Lin

ACKNOWLEDGMENTS

TABLE OF CONTENTS

iv

LIST OF TABLES

LIST OF ILLUSTRATIONS

I. Introduction

The arrangement of clouds and convection in a horizontal row or band structure is a commonly-observed phenomenon. This arrangement is of utmost interest from a basic and applied scientific point of view. Such organization is especially prevalent in the Arabian Sea region during monsoon (Rao, 1976). In addition to the shallow non-precipitating cloud bands over the western Arabian Sea, deep convective bands are often observed over the eastern Arabian Sea. The bands' kinematic and thermodynamic structures are now beginning to be analyzed (Benson and Rao, 1987; Hor, 1988) and simulated using a numerical cloud model (Hor, 1988).

Past theoretical studies have included an examination of the vertical wind profile, stability of the stratification, diffusion coefficients and the amount and vertical distribution of the latent heat release. A direct extrapolation of these studies to the Arabian Sea should be questioned, however. The Arabian Sea exhibits a strong monsoonal signal. In June, after the establishment of the Indian monsoon, an intense low-level westerly jet exists near 850 mb and an equally if not more intense tropical easterly jet (TEJ) exists at 150 mb. A significant inversion is present in the western Arabian Sea while it is diluted in the eastern area. The sea surface temperatures are relatively cooler in the western Arabian Sea. A shallow

1

convection is noticed in the west, while longitudinally-arranged (parallel to the east-west shear) bands of deep convection develop in the eastern Arabian Sea. New research is demanded to explain the differences between the western and eastern Arabian Sea.

Considerable interest in deep tropical cloud bands (in addition to those associated with the tropical cyclone circulation) has emerged over the last decade with the completion of GATE, MONEX, and AMEX. It therefore seems appropriate to begin a basic investigation of the MONEX bands by employing linear theory through which closed form solutions may be obtained.

II. The Problem

a. Physical Description

The Arabian Sea troposphere during monsoon is character-
ized by strong westerly flow in the low levels due to the
Somali jet. The mean June westerly jet at Minicoy (8N, 73E),
for example, has a maximum of 20-30 m/s near 1 km MSL. Above
this level, the easterly component increases steadily, in an
almost linear fashion, reaching a peak of 50 m/s at 16 km. The
v component is considerably smaller in magnitude at all levels
than the u component. These features are evident in the E.
Arabian Sea wind base state. On climatological means, the
overriding feature of the flow is the Poiseuille-like structure
below 2 km and the Couette-like structure above. The latitudi-
nal extent enclosed by the 20 m/s isotach on the 850 mb pres-
sure surface in July is about 800 km. Soundings show deep
moisture with strong convective instability below 700 mb (see
chapter 5). Simple plume cloud models suggest bubbles given an
initial impulse will rise through large depths of the tropo-
sphere. At the surface, vapor contents are in excess of 20
g/kg providing a rich fuel supply for deep convection. The
large shearing wind speeds associated with a deep, moist layer
and convective instability provide a unique environment for
analysis and analytical investigation.

Satellite data indicate extensive offshore convection

3

(west of the Indian coast) during the monsoon not associated with local circulations such as the land sea breeze. Grossman and Durran (1984) provided a case study of monsoon convection for 24 June 1979 which was considered characteristic of fully-developed flow. The convective area appeared to be stationary with a thick anvil shearing to the west for about 200 km due to strong easterly winds in the upper troposphere. Boundary layer wind speeds increased as one proceeded upstream (westerly) away from the Indian coast (Fig. 2.1). West of the anvil region, cumulus convection is encountered which becomes increasingly inversion-capped towards the west (400-600 km offshore). Their description is well-reflected in the DMSP photos taken during this time (see chapter VIII).

However, a distinction between the western and eastern Arabian Seas with respect to their vertical shear, thermodynamic profile, and sea surface temperature seems necessary. Both Holt and SethuRaman (1985) and Grossman and Durran (1984) have documented that during the monsoon the low-level jet is stronger over the western half than the eastern half. The P-3 sawtooth runs in the western Arabian Sea on 24 June vividly show rough seas and visibility restrictions due to sea spray caused by strong winds. The subcloud layer is well mixed and deeper over the western Arabian Sea. A capping inversion limits the convective growth over the west. (Fig. 2.2)

The eastern Arabian Sea, on the other hand, is conditionally unstable above the subcloud layer with deep convection
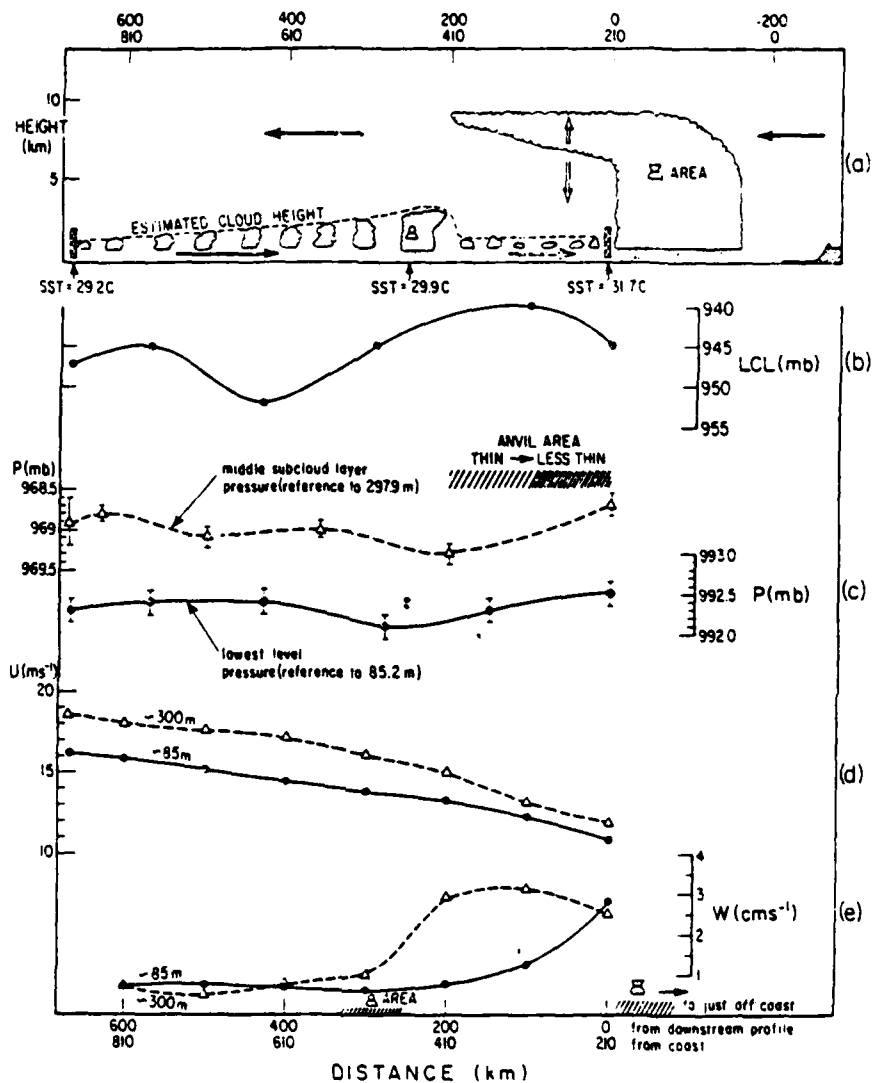
Fig. 2.1 Along stream cross section of (a) observed convective cloudiness, (b) LCL, (c) observed static pressure compensated for diurnal and anvil effects, (d) observed mean horizontal winds, and (e) estimated vertical velocity for Arabian Sea on 24 June 1979 Grossman and Durran (1984)
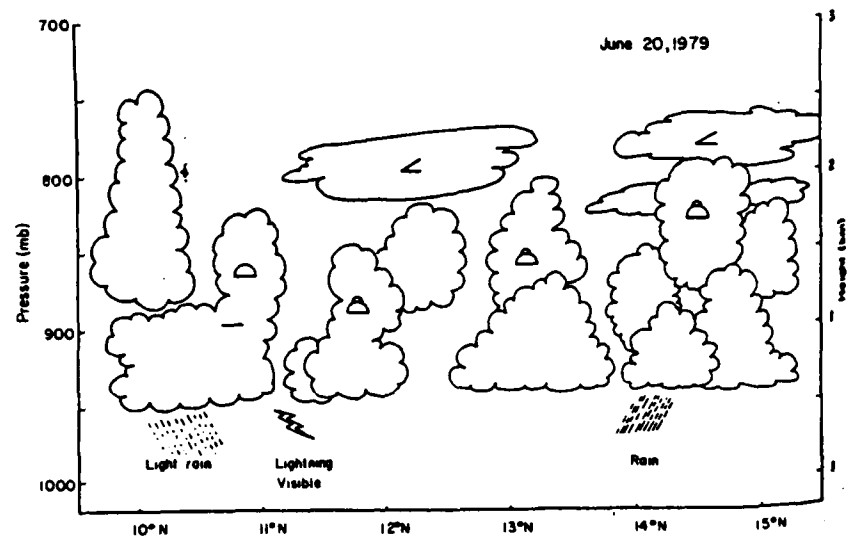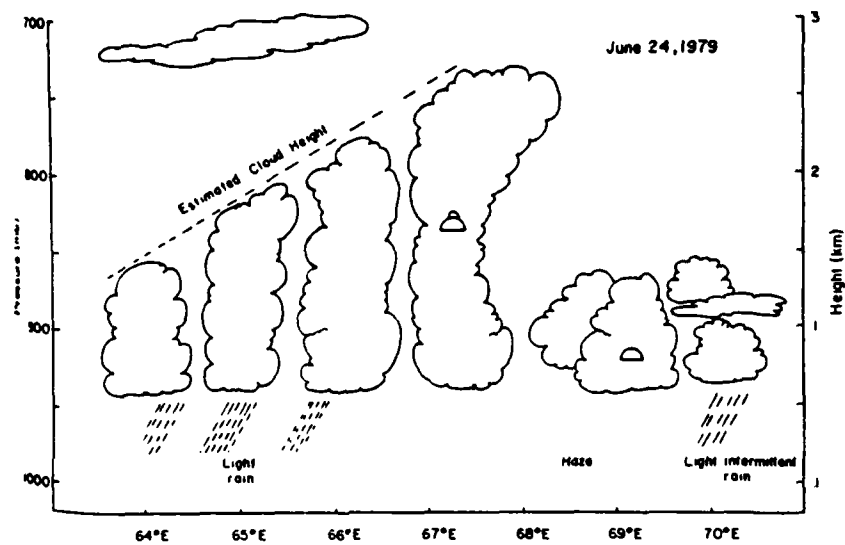
Fig. 2.2 Cross-Section of Observed Cloud Structure for 20 (a)
and 24 (b) June 1979 for the Arabian Sea (Holt and
SethuRaman, 1985)

6

observed and exhibits in general a weaker but more elevated jet (Holt and SethuRaman, 1985). The mixed layer depth is also suppressed --most likely due to low-level outflow of downdrafts spreading over the relatively warm sea surface. Finally the sea surface temperature differences are higher in the eastern Arabian Sea than the western Arabian Sea. This implies a larger latent heat contribution from the air-sea lower boundary.

These observations suggest a distinction be included in the base state variables between western and eastern Arabian Sea. The western base state would be characterized by a sharper and lower (in height) jet nose along with a more shallow latent heating distribution and more stable lapse rate. The eastern base state would exhibit an elevated but weaker low level jet, more conditionally unstable lapse rate, and a greater contribution to heating because of deep convection. Furthermore, we might expect the central Arabian Sea ($\sim$65E) to serve as a transition zone between the two regimes.

It is evident from routine satellite imagery that convection, especially in the eastern and central Arabian Sea, tends to form in E-W bands. Aircraft investigations have also confirmed this mode. Benson and Rao (1987) described the characteristics of a convective cloud cluster over the eastern Arabian Sea on 20 June 1979. Their analysis revealed the existence of several cloud bands within the cluster. They noted the cloud bands were quasi-stationary whose life spans

were restricted perhaps by the vertical distribution of the base state winds. They suggested that new bands are initiated as exhaust air is pushed ahead of the source band and recovers its thermodynamic energy because of sensible and latent heat transfers from the sea surface. According to their analysis, these new cloud bands were aligned parallel to the low-level flow.

Benson and Rao's conceptual model of the Arabian Sea cloud band differed somewhat from those observed during GATE. In the Arabian Sea cloud band, anvils are sheared to the west over top of the high- energy low-level westerly flow. The MONEX environment for cloud bands is characterized by SSTs slightly higher than those of the GATE environment and boundary layer specific humidity values about 2 g/kg higher than observed during the GATE band activity. Correspondingly, the inflow air feeding the Arabian Sea cloud band has higher θ_w values than the GATE inflow air. Finally, the Arabian Sea squall lines tended to be quasi-stationary and parallel to the low-level flow. The GATE cloud lines in many instances were aligned normal to the environmental flow.

b. Hypothesis

It is hypothesized that the base state temperature, moisture, and vertical wind distribution exercise primary control over the observed Arabian Sea convection band characteristics. By using base states associated with previously-observed con-

vection during MONEX 79, the response of the linear system (consisting of anelastic perturbation equations') can be studied and compared qualitatively to the general band features. Such features include orientation angle in the wavenumber domain relative to the shear, phase speed, growth rates,vertical structure, and spacing. Input parameters which can be varied (besides the base state itself) include characteristic cloud core size, latent heat depth and distribution, precipitation efficiency, eddy diffusion, detail of the wind profile, type of moisture accession, and surface fluxes. Also, correlation quantities (e.g., $\overline{u'w'}$) produced by the analytical model will be compared with those of previous analytical and observational researchers.

Furthermore, it is proposed that the different characteristics of convection observed over the western, central, and eastern Arabian Sea can be attributed to the different wind and thermodynamic regimes associated with these respective areal base states.

To accomplish the above, both representative data and an analytical model which includes (within mathematical and computing limitations) as fully as possible the basic physical processes associated with deep tropical convection will be used. The remainder of this dissertation describes an attempt to accomplish this task.

III. Review of Related Literature

a. Physical Analyses

The observation of banded cloud structures first became prominent with the development of aviation (Kuettner, 1971). Malkus and Riehl (1964), based on their photo-reconnaissance, noted that tropical convective bands in the Pacific tend to occur in highly selective patterns. For the most part, cumuli were aligned in streets but taller clouds were often observed in rows at large angles to the low-level wind. Satellites (manned and unmanned) have also during the past 30 years provided a tremendous amount of information concerning the occurrence of cloud bands and streets. Kuettner (1971) noted the spacing of shallow cloud bands in the BOMEX project (1969) ranged from 2 to 8 km for a layer depth of 0.8 to 2 km with alignment along the mean wind of the layer. However, for more vigorous convection, Malkus and Riehl found the tall clouds to be spaced between 30-100 km.

In part as a result of the above, interest has increased concerning the nature of deep cloud bands and lines (LeMone et al., 1984). Barnes and Sieckman (1984) studied the environment of fast- and slow-moving mesoscale convective cloud lines observed during the GATE (1974) experiment. Their analyses showed that the vertical shear of the horizontal wind is normal to the leading edge of convection in fast-moving lines but

10

parallel to the leading edge of the slow-moving lines. Also, the GATE fast- moving lines had a more pronounced minimum in θ_e at 700 mb. While the environmental differences between the two types of GATE lines were small relative to the corresponding differences of their mid-latitude counterparts, they suggested that these small differences may be critical to the organization of convection (e.g., streets, bands, etc.) and to the characteristics of convection (shallow, deep, propagating or stationary, etc.)

Dudhia and Moncrieff (1987) numerically simulated a quasi-stationary tropical convective band using a 3-dimensional model and an initial structure using a ship-based sounding located near the band. They noted environmental conditions favorable for formation were lower tropospheric easterly shear and a deep layer of conditional instability. However, the quasi-stationary band required large-scale forcing throughout its development implying that the growing convection is continually responding to larger-scale convergence and the energy supplied by the larger scale is very important in supporting the convection. However, a propagating band can maintain itself even in the region occupied by the quasi-stationary system without such forcing.

Benson and Rao (1987) analyzed the convective bands associated with the Arabian Sea cloud cluster. In comparison with those studied during GATE, the monsoon bands' anvil clouds were sheared towards the west over the low-level westerly flow

(Grossman and Durran, 1984). This was in contrast to the GATE bands whose inflow was protected from the subsidence beneath the anvil. Also, the vertical shear in the Arabian Sea regime was considerably stronger (westerly flow in the low levels with easterly flow aloft) but the bands studied were quasi-stationary and parallel to the lower tropospheric wind shear. Hor (1988) in his PhD dissertation noted in the Eastern Arabian Sea momentum transports were down-gradient above 3 km but up-gradient throughout the cloud layer in the Central Arabian Sea. Furthermore, he observed that the large-scale flow received its kinetic energy from the cloud bands over the Central Arabian Sea but transferred its energy to the EAS cloud bands.

b. Previous Theoretical Investigations

Theoretical investigations into the dynamical causes and behavior of cloud bands in the atmosphere have to some extent paralleled the development of numerical methods and computing capabilities. Kuo (1963) provided the first analytical investigation into cloud streets. Performing a linear stability analysis of the basic equations using the Boussinesq approximation, Kuo studied the behavior of small perturbations in a plane Couette flow within a dry stably- and unstably-stratified fluid. He found that below a critical negative Richardson number, two unstable regions existed --one which contained long, stationary amplifying waves and the other region containing transient gravity waves. The frequently-observed shallow

cloud streets or rows were attributed to the stationary (with respect to the basic flow) mode. Asai (1970) also studied the role of plane Couette flow within an unstable "dry" fluid stratification. He showed that the vertical transfer of horizontal momentum is controlled by the orientation of the bands in the horizontal plane with respect to the mean shear vector (sometimes called "three-dimensionality of the convection"). In particular, the upward transfer of horizontal momentum tends to intensify the shear of the basic flow when the perturbations' mode is transverse (aligned perpendicular to the mean flow). However, for longitudinal perturbations aligned parallel to the mean flow, the kinetic energy of the basic flow is transferred to the perturbation through downward transfer of momentum. Asai (1970b) also showed that unstable perturbations of thermal origin are more likely to yield a longitudinal mode while perturbations of inertial origin favor a transverse mode. Here, the term "thermal" implies gravitational instability associated with buoyancy while the term "inertial" refers to inflection point instability associated with a parabolic wind profile. Eymard (1985) used the observed mean wind and temperature profiles in a tropical (Ivory Coast) boundary layer and compared Asai's model results with the observed convective organization. He concluded that the wind shear was the principal cause of convective organization. However, the organizing effect of the shear depends both on the static stability and shear or on the Richardson number.

Rosmond (1973) was one of the first to include latent heating in the linear stability analyses. His model involved only two layers and his perturbation heating attempted to simulate the effects of non-precipitating growing cumuli in a shallow layer. Sun (1978) employed the linearized anelastic perturbation equations and a 20-layer model to perform the linear stability analyses of deep convection. Including a base state wind and temperature profile, Sun parameterized latent heating through a "Wave -CISK" (Conditional Instability of the Second Kind) scheme whereby the heating was created through the vertically-integrated moisture advection within the conditionally unstable layer. The heat was partitioned somewhat arbitrarily in the vertical by a sinusoidal function. In this manner, he could control the depth and vertical distribution of convective heating which was not possible in Rosmond's model due to the limited number of levels. Sun also included non-isotropic eddy diffusivities to ensure a short wave cutoff as suggested by Priestley (1962). In his work, Sun found that the depth and magnitude of convective heating were critical in determining the orientation of the dominant mode. For large (small) flux Richardson numbers, he found the most unstable mode of convection to be parallel (perpendicular) to the shear when making a comparison between dominant modes associated with individual base states. In a practical sense, the transverse mode became dominant if deep convection extended into a more stable layer or if the moisture supply feeding the convection became weak.

c. Notes on CISK and Wave-CISK

It seems appropriate to conduct a brief discussion of the general concepts of Conditional Instability of the Second Kind or "CISK" and their application to the problem under study. One general definition of CISK might be the mutual cooperation of cumulus-scale convection and the larger-scale disturbance in nourishing each other through the convergence of moisture (requiring eventual phase change) into the disturbance domain.

Conventional CISK formulations were first introduced by Charney and Eliassen (1964) and Ooyama (1964) where surface friction served as an indirect driver by feeding moisture through Ekman pumping into a balanced vortex. While confining the frictional effect to a surface boundary layer, Charney and Eliassen considered the accession of cloud moisture into a vertical column through the entire atmospheric depth. Ooyama (1964) considered only the pumping of moisture from a shallow layer into the environmental layer above. That is, the shallow layer served as an entraining moist layer feeding the towers detraining above in the environmental layer. According to Syono and Yamasaki (1966), a similar closure was first proposed by Syono as early as 1944 for precipitation rates in typhoons. Ooyama (1969) elaborated more on the differences of approach between himself and Charney and Eliassen. He stated that by including convergence of moisture at every level as Charney and Eliassen did, convective activity might be allowed in convectively -stable mid-tropospheric air. In nature, according to

Ooyama, the major contribution to the total convergence of water vapor in a vertical column should come from convergence in the boundary layer. In turn, the BL moisture supply was furnished by the large sea areal expanse under the influence of the tropical cyclone circulation. The Ooyama scheme for diabatic mass flux was adopted subsequently in CISK studies by Ogura (1964), Kuo (1965), and Koss (1976).

The concept of Wave-CISK was formally introduced by Lindzen (1974) although Yamasaki may have originated the concept. In Wave-CISK, low-level convergence is due to inviscid wave fields rather than to Ekman pumping. These waves in turn then give rise to mean cumulus activity. With Wave-CISK, internal friction serves to diminish wave convergence and thus cumulus heating which is tied to the low-level pumping. The Wave-CISK concept was tied to a linear model of moist convective instability by Raymond (1975) who suggested that propagating convective storms take the form of convectively-forced gravity waves. The group velocity associated with this packet of gravity waves represents the propagation velocity curve. Other tropical Wave-CISK studies such as Stevens and Lindzen (1978), Koss (1976), and Wang and Barcilon (1986) tied the cumulus heating to the vertical motions at the top of the sub-cloud layer while Stark (1976), Sun (1978), and Rosmond (1973) formulated convective heating in terms of the moisture convergence extending through the cloud layer depth or through the entire atmosphere.

Another topic of some uncertainty among CISK studies is the cause of the "short-wave cut-off". According to Frank (1987), linear CISK theory essentially predicts the existence of cumulus clouds because the maximum growth rates appear at the smallest wavelengths. As noted by Chang and Williams (1974), the original CISK models of Charney and Eliassen (1964) and Ooyama (1964) exhibited increase in growth rate with decreased horizontal scale while exhibiting no preferred maximum. One method to control this problem is to introduce horizontal diffusion or lateral mixing into the model. This procedure was invoked by Koss (1976), Sun (1978), and Rosmond (1973). As suggested by Priestley (1962) and Agee (1975), a horizontal to vertical diffusion ratio of 100 was used by both Rosmond and Sun. Another method suggested by Chang and Williams is the Ekman damping of small scales in a stratified atmosphere. This is accomplished by introducing a temperature fluctuation at the top of the Ekman layer. Mak (1982) induced a short-wave cutoff in an analytical investigation of moist quasi-geostrophic baroclinic instability by expressing the diabatic heating term strictly in terms of the vorticity field of the disturbance instead of the vertical velocity field as is often done. Wang and Barcilon (1986), however, criticized Mak's approach since it neglected the low-level convergence directly induced by latent heat release and was inconsistent with the fact that low-level convergence is partly driven by latent heat.

The nature and sensitivity of CISK results to the vertical heating profile have received considerable discussion. Previous CISK studies have shown strong sensitivity to the diabatic heating profile --both its shape and the model's vertical resolution. This implies CISK results are very sensitive to the particular cumulus parameterization used and the number of model levels. For example, Syono and Yamasaki (1966), Koss (1976), Sun (1978), Mak (1982), and Wang (1987) have previously discussed these matters. Stark (1976) apparently introduced the first non-adiabatic CISK heating profile that was linked to the observed atmosphere thermodynamic structure as well as to the vertical velocity fields contained within the entire cloud vertical domain. Others, like Sun, Wang, and Koss used analytical profiles. As noted by Stark (1976), however, it seems unreasonable that the heating profile be described independent of the thermodynamic structure of the base state. Commenting in part on Syono and Yamasaki's results, Sun (1978) noted that a shift of the heating distribution to higher levels in the atmosphere was more likely to produce propagating waves for a given base state while heating distributions weighted more to the lower atmosphere more likely would produce a stationary mode. However, in the former case which is often associated with deep clouds, a very large moisture supply could still result in a stationary mode. With respect to vertical resolution, Stark (1976) stated that by increasing the vertical resolution, the model's sensitivity to the discrete vertical specification of the dependent variables is reduced. Wang

(1987), by employing a continuously-stratified (in the verti-
cal) hydrostatically balanced model with a variable analytical
vertical heating profile, showed that lower cloud tops result
in growth in shorter waves and slower wave propagation. By
fixing the cloud top and base, Wang's results indicated that
heating with a maximum below the cloud center had a similar
influence to that of a lower cloud top while increasing the
cloud top increased the growth rate but also increased the wave
speed.

Uncertainties in the vertical heating profile have not
only plagued CISK studies but also hurricane modelers.
Rosenthal (1979), using an axisymmetric hurricane model, showed
that growth of the hurricane scale is significantly affected
when the details of the cumulus parameterization scheme (cloud
model and form of the cloud spectrum) are altered. This is
because the major driving force in a hurricane is the release
of latent heat in organized cumulus convection. For non-linear
initial value problems, cumulus clouds may be directly included
through the cloud vapor and water budget terms in the model's
governing equations if sufficiently small grid spacing is
employed. For the linear boundary-value problem posed by CISK
or Wave-CISK, the direct approach is not feasible.

A basic assumption of the Wave-CISK process is one of
quasi-equilibrium between the cumulus-scale convection and the
larger mesoscale development. That is, the diabatic heating
induced by cloud scale motion is instantly related to the

moisture convergence of the larger-scale wave flow. This assumption is intrinsic to the typical unconditional diabatic heating closure of the thermodynamic energy equation. Here, "unconditional" implies warming in the upward branch and cooling in the downward branch of the periodic flow structures. Xu and Clark (1984) questioned the validity of the quasi- equilibrium assumption, stating that it was only reasonable if the life cycle of cumulus clouds is negligibly small compared to the time scale associated with changes in the mesoscale motion. They noted that eigenmodes of Wave-CISK are propagating structures which move past the cumulus towers, thus spreading the released latent heat only over a certain region of the wave pattern. For mesoscale Wave-CISK, a typical perturbation period of the mesoscale convective system (MCS) is about two hours while the typical life cycle of the cumulus cloud is about 30 minutes. Thus, the estimated phase (or time) lag of the cumulus cloud with the CISK eigenmode is not insignificant. In supporting the concept of mesoscale weather modification, Fritsch (1986), however, disputes this contention. He states that the mesoscale environment and the characteristics of individual clouds are inseparably linked as a single functioning unit. Furthermore, the mesoscale environment responds quickly and strongly to heating from moist convection and has a correspondingly large impact in determining the location and amount of convection. In addition, Fritsch states that the role of moist downdrafts and microphysical processes in the stratiform middle levels of cloud systems needs more

consideration. Yamasaki (1984), using an explicit cumulus representation, noted that downdraft and cooling due to the evaporation of convective clouds played an important role in organizing the mesoscale disturbance by forming clouds through interaction of the larger-scale flow and the small-scale down-drafts associated with the evaporation of falling rain.

A final note clarifying scale definition is in order. The vertical distribution of heating sought from the cumulus param-eterization scheme should be representative of the mean "cloud-scale." This "cloud-scale" includes both the updrafts and downdrafts of the individual convective cores or towers and their environment. In general, the vertical velocities associ-ated with this "cloud-scale" will be much larger than those associated with the synoptic scale but much smaller than those associated with the individual convective towers. In the linear model formulation to be discussed subsequently, the vertical velocity formulation in the diabatic heating term is representative of the mean "cloud-scale." Because of the Fourier transforms, both ascending and descending branches will appear in the solution introducing the so-called "uncondi-tional" heating intrinsic to eigenvalue problems. However, both branches are representative of the banding pattern and may be considered as belonging to the mean "cloud-scale" properties such that the ratio of cloudy area to total area "a" is 1.0. The "cloud-scale" will encompass the lower portions of the mesoscale wavelengths.

IV.   The Linear Model

a.   Introduction

The approach for this study is to employ a linear system of perturbation equations and determine analytical solutions for this system using a normal mode assumption. The basic solution procedures follow those of Chandrasekhar (1961) with the exception that the solutions are obtained using a numerical algorithm for the resulting eigenvalue problem. The system may be considered to represent an infinite domain boundary value problem where boundary conditions are required for the upper and lower boundaries only.

A linear stability analysis involves using the linearized perturbation forms of the hydrodynamic equations and determining whether this system, when defined by certain "base state" parameters such as the prevailing velocity field and temperature gradient, is stable or unstable to small disturbances. Specifically, we ask, if the system is initially at rest and then disturbed will the disturbance gradually die down or will the disturbance grow in amplitude in such a way that the system progressively departs from the initial state and never reverts to it (Chandrasekhar, 1961)? In the former case, the system is stable; in the latter case it is unstable.

In obtaining the linearized perturbation equations from

the equation of motion, we neglect all products and powers (higher than the first) and retain only terms which are linear in them. We presuppose that the perturbations or disturbances are infinitesimal. Furthermore, the base state parameters governing the system are considered steady-state and functions of only one dimension (for example, the z axis). To practically investigate the reaction of a linear system to all possible disturbances, we analyze the perturbation in terms of two-dimensional periodic waves:

$$a(x,y,z,t) = \int_{-\infty}^{+\infty} \int_{-\infty}^{+\infty} A_k(z,t)\exp(ik_x x + ik_y y)dk_x dk_y \qquad (1)$$

where A_k is the double Fourier transform of a and

$$k = (k_x^2 + k_y^2)^{1/2}$$

To eliminate the dependence on time, we use the following equation:

$$A_{k\sigma}(z) = \int_{-\infty}^{+\infty} A_k(z,t)\exp(-\sigma t)dt \qquad (2)$$

where $A_{k\sigma}(z)$ is the Laplace transform of $A_k(z,t)$ and

$$\sigma = \sigma_r + i\sigma_i$$

where σ is a frequency. It is apparent that the complex frequency $\sigma(k)$ will depend not only on the modes k but also on the base state parameters. The condition for stability is that σ_r

will be negative for all k. If $\sigma_r(k) = 0$ implies $\sigma_i(k) = 0$, then the onset of convection will be stationary. If $\sigma_i(k) \neq 0$, then convection will develop with some degree of overstability or oscillatory motion.

By invoking the above transform definitions, we obtain solutions which possess the transform properties of linearity, symmetry, etc. and allow for rapid transition between the two domains. Furthermore, we may invoke the Convolution and Correlation theorems respectively:

$$a(1)*b(1) = \int_{-\infty}^{+\infty} a(r)b(1-r)dr \quad \longleftrightarrow \quad A(k) \cdot B(k) \tag{3}$$

$$\int_{-\infty}^{+\infty} a(r) \cdot b(1+r)dr \quad \longleftrightarrow \quad A^*(k) \cdot B(k) \tag{4}$$

where r is a dummy function for wavelength and 1 becomes a shift along the r axis. * signifies a complex conjugate. (4) will be of special importance when correlation quantities such as Reynolds fluxes are desired from the spectral or transform quantities.

Obtaining solutions to systems of linear differential equations is often preferred as a first step in the study of a problem since exact solutions are possible (within the limitations of the linear algorithm and parameterization procedures used) which are free of computational error associated with numerical methods. Linearized models can provide physical

insight into the fundamental qualitative aspects of the circulation system under investigation. Furthermore, an accurate nonlinear numerical model must be able to reproduce the linear results closely when the products of the dependent variables are small (Pielke, 1984).

By the application of the linear perturbation approach, all initial disturbances are assumed to be infinitesimal relative to the base state mean properties. The eigenvalue analysis of a system gives at an instant of time t_o the instantaneous behavior of the modes supported by the system. However, to initiate growth in the model studied here requires the introduction of a convective heating profile which pre-supposes the existence of well-developed convective towers or cores. Some credence is lent to the linearization procedure through the scale separation of the modeled band systems (spacing ~ 10 - 30 km which is imposed by the anisotropy of heat and momentum diffusion) and the convective core radius (~ 1 km). Through use of a three scale division including synoptic scale (base state), cloud scale (eigenfunction), and unresolved core or tower scale (1DSS cloud model), the linear assumption becomes more plausible.

By neglecting finite amplitude disturbances, we are also neglecting the advection of heat and momentum by the disturbance as well as the evolution of its amplitude. To account for these finite amplitudes requires the use of numerical techniques for the nonlinear system. This is not a straight-

forward matter since the non-linear advective terms prove in practice to be difficult to handle without imposing diffusion or filtering. Such methods may require considerable time and experimentation before implementation of an "appropriate" procedure for non-linear instability is possible. Furthermore, the raw output from such a model may preclude simple understanding of the physical processes behind the results, especially for an inexperienced investigator.

b. The Governing Equations

The following notation is employed for the linear model equations (excluding cloud model and other ancillary subroutines) throughout the text unless otherwise stated:

(1) primed variables represent dimensional quantities

(2) variables with an overbar represent mean or base state quantities

(3) lower case meteorological variables such as w , θ , p , u , v , ζ etc. denote perturbation variables except as noted. Asterisked lower case variables represent non-dimensional perturbation variables.

(4) other unprimed variables denote dimensionless quantities

(5) capitalized meteorological variables with no primes or overbars represent transform quantities. Asterisked capitalized variables denote complex conjugates.

(6) constants such as f, f^*, ν_h etc. remain in lower case form with no primes or overbars. Characteristic numbers such as the Rossby number, Prandtl number, etc. are written in standard format.

The approximate linearized anelastic perturbation equations for which solutions are sought are:

$$\frac{\partial \overline{\rho_o}'u'}{\partial t'} + \overline{U}'\frac{\partial \overline{\rho_o}'u'}{\partial x'} + \overline{V}'\frac{\partial \overline{\rho_o}'u'}{\partial y'} + \overline{\rho_o}'w'\frac{\partial \overline{U}'}{\partial z'} = \tag{5}$$

$$- \frac{\partial p'}{\partial x'} + f\overline{\rho_o}'(\overline{V}' + v') - f^*\overline{\rho_o}'w' +$$

$$\nu_h \left[\frac{\partial^2 \overline{\rho_o}'u'}{\partial x'^2} + \frac{\partial^2 \overline{\rho_o}'u'}{\partial y'^2}\right] + \nu_z \left[\frac{\partial^2 \overline{\rho_o}'(\overline{U}' + u')}{\partial z'^2}\right]$$

$$\frac{\partial \overline{\rho_o}'v'}{\partial t'} + \overline{U}'\frac{\partial \overline{\rho_o}'v'}{\partial x'} + \overline{V}'\frac{\partial \overline{\rho_o}'v'}{\partial y'} + \overline{\rho_o}'w'\frac{\partial \overline{V}'}{\partial z'} = \tag{6}$$

$$- \frac{\partial p'}{\partial y'} - f\overline{\rho_o}'(\overline{U}' + u') + \nu_h \left[\frac{\partial^2 \overline{\rho_o}'v'}{\partial x'^2} + \frac{\partial^2 \overline{\rho_o}'v'}{\partial y'^2}\right] +$$

$$\nu_z \left[\frac{\partial^2 \overline{\rho_o}'(\overline{V}' + v')}{\partial z'^2}\right]$$

$$\frac{\partial \overline{\rho_o}'w'}{\partial t'} + \overline{U}'\frac{\partial \overline{\rho_o}'w'}{\partial x'} + \overline{V}'\frac{\partial \overline{\rho_o}'w'}{\partial y'} = \tag{7}$$

$$- \frac{\partial p'}{\partial z} + g\alpha\overline{\rho_o}'\theta' + f^*\overline{\rho_o}'(\overline{U}' + u') +$$

$$\nu_h \left[\frac{\partial^2 \overline{\rho_o}'w'}{\partial x'^2} + \frac{\partial^2 \overline{\rho_o}'w'}{\partial y'^2}\right] + \nu_z \left[\frac{\partial^2 \overline{\rho_o}'(w')}{\partial z'^2}\right]$$

$$\frac{\partial \overline{\rho_o}'u'}{\partial x'} + \frac{\partial \overline{\rho_o}'v'}{\partial y'} + \frac{\partial \overline{\rho_o}'w'}{\partial z'} = 0 \tag{8}$$

$$\frac{\partial \overline{\rho_o}'\theta'}{\partial t'} + \overline{U}'\frac{\partial \overline{\rho_o}'\theta'}{\partial x'} + \overline{V}'\frac{\partial \overline{\rho_o}'\theta'}{\partial y'} + \overline{\rho_o}'w'\frac{\partial \overline{\theta}'}{\partial z'} = \tag{9}$$

$$Q' + \kappa_h \left[\frac{\partial^2 \overline{\rho_o}'\theta'}{\partial x'^2} + \frac{\partial^2 \overline{\rho_o}'\theta'}{\partial y'^2}\right] + \kappa_z \left[\frac{\partial^2 \overline{\rho_o}'(\theta')}{\partial z'^2}\right]$$

The equations are respectively, the u' , v' , and w' momentum equations, the continuity equation, and the thermodynamic energy equation. Sun (1978) derived these forms with the exception that his equations did not include the Coriolis terms. Consider $\overline{U}'$, $\overline{V}'$, and $\overline{\theta}'$ to be steady-state and horizontally-averaged terms. The mean vertical velocity $\overline{W}'$ = 0. The perturbation terms are sufficiently small so that terms involving their products may be neglected relative to the rest of the equation. Q' is a source term representing latent heat release. $\overline{\rho_o}'$ is the time invariant mean density which varies only in the vertical.

The adjective "anelastic" refers to the set of governing equations where density is allowed to vary in all terms of the equations of motion with the proviso $\frac{\partial \overline{\rho_o}'}{\partial t'}$ = 0 in the continuity equation. Th_ assumptions involved are that the percentage range in potential temperature is small and the time scale is small (greater than about 100 sec as set by the Brunt-Vaisala frequency) such that sound waves are not permitted. For shallow convection, the anelastic approximation reduces to the

Boussinesq form where density will vary only in the terms involving the external force (e.g. gravity).

In order to simplify the equations to a more tractable form for a solution, eliminate u', v', and p' from equations (5) - (7) while treating f, f^*, ν_z, ν_h, κ_h and κ_z as constants. These variables represent the Coriolis parameters and anisotropic diffusion terms (h denotes horizontal and z denotes vertical direction). The following method is used:

a. Take $\frac{\partial}{\partial x'}$, $\frac{\partial}{\partial z'}$ (u' momentum equation)

b. Take $\frac{\partial}{\partial y'}$, $\frac{\partial}{\partial z'}$ (v' momentum equation)

c. Take $\frac{\partial^2}{\partial x'^2} + \frac{\partial^2}{\partial y'^2}$ (w' momentum equation)

d. Take $\frac{\partial}{\partial z'}$ (anelastic continuity equation)

e. Use d. to eliminate u' and v' in a. and b.

f. Add a. and b.

Note that $\frac{\partial \overline{\rho_o' v'}}{\partial x'} - \frac{\partial \overline{\rho_o' u'}}{\partial y'} = \zeta'$. Invoking commutativity wherever possible, subtract f. from c. This step yields the following expression:

$$\left(\frac{\partial}{\partial t'} + \overline{U}'\frac{\partial}{\partial x'} + \overline{V}'\frac{\partial}{\partial y'}\right)\left(\nabla'^2_h \overline{\rho_o' w'}\right) - \frac{\partial^2 \overline{U}'}{\partial z'^2}\frac{\partial}{\partial x'}(\overline{\rho_o' w'}) - \qquad (10)$$

$$\frac{\partial^2 \overline{V}'}{\partial z'^2}\frac{\partial}{\partial y'}(\overline{\rho_o' w'}) =$$

$$g\alpha\nabla'^2_h(\overline{\rho_o}'\theta') - f^*\frac{\partial\zeta'}{\partial y'} - f\frac{\partial\zeta'}{\partial z'} + \nu_z\frac{\partial^2}{\partial z'^2}(\nabla'^2\overline{\rho_o}'w') + \nu_h\nabla'^2_h(\nabla'^2\overline{\rho_o}'w')$$

The vertical component of the vorticity equation can be derived by: $\frac{\partial}{\partial x'}$ (v' momentum equation) $- \frac{\partial}{\partial y'}$ (u' momentum equation). This yields:

$$\frac{\partial\zeta'}{\partial t'} + \overline{U}'\frac{\partial\zeta'}{\partial x'} + \overline{V}'\frac{\partial\zeta'}{\partial y'} + \frac{\partial\overline{V}'}{\partial z'}\frac{\partial\overline{\rho_o}'w'}{\partial x'} - \frac{\partial\overline{U}'}{\partial z'}\frac{\partial\overline{\rho_o}'w'}{\partial y'} = \qquad (11)$$

$$f\frac{\partial\overline{\rho_o}'w'}{\partial z'} + f^*\frac{\partial\overline{\rho_o}'w'}{\partial y'} + \nu_z\frac{\partial^2\zeta'}{\partial z'^2} + \nu_h\nabla'^2_h\zeta'$$

Thus equations (10), (9), and (11) yield three equations for three perturbation variables w', θ' , and ζ'.

b. 2. Non-Dimensionalization

Equations (9), (10), and (11) can be further generalized by using non- dimensional perturbation variables θ^*, w*, u*, v*, and ζ^* and the non-dimensional base state variables $\overline{\theta}$, $\overline{T}$, $\overline{U}$, $\overline{V}$, and developing the following relationships where unprimed terms represent the non-dimensional variables:

$$\overline{\rho_o}'\theta' = \rho_{oo}\Delta T\theta^* \ , \ \overline{\theta}' = \Delta T\overline{\theta} \ , \ \overline{T}' = \Delta T\overline{T}$$

$$\overline{\rho_o}'w' = \rho_{oo}U_Tw^* \ , \ \overline{U}' = U_T\overline{U}$$

$$\overline{\rho_o}'u' = \rho_{oo}U_Tu^* \ , \ \overline{V}' = U_T\overline{V}$$

$$\overline{\rho_o' v'} = \rho_{oo} U_T v^*$$

$$\zeta' = \frac{\partial \overline{\rho_o' v'}}{\partial x'} - \frac{\partial \overline{\rho_o' u'}}{\partial y'} = U_T \frac{\rho_{oo}}{H} \left(\frac{\partial v^*}{\partial x} - \frac{\partial u^*}{\partial y} \right) =$$

$$U_T \frac{\rho_{oo}}{H} \zeta^*$$

Here, ρ_{oo} is the surface density of the atmosphere, U_T and ΔT are the characteristic speed and potential temperature difference between the top and bottom of the fluid and H is the depth of the atmosphere under consideration. The characteristic time scale of the atmosphere is then:

$$\tau = \frac{H}{U_T} \; ; \; t' = \tau \cdot t$$

where t is the non-dimensional time.

Noting that

$$\nabla_h'^2 = \frac{1}{H^2} \nabla_h^2 \; ; \; \frac{\partial}{\partial x'} = \frac{1}{H} \frac{\partial}{\partial x} \; ; \; \frac{\partial}{\partial y'} = \frac{1}{H} \frac{\partial}{\partial y} \; ; \; \frac{\partial}{\partial z'} = \frac{1}{H} \frac{\partial}{\partial z'}$$

and

$$\frac{\partial}{\partial t'} = \frac{U_T}{H} \frac{\partial}{\partial t}$$

and substituting all of the above expressions into (10) yields the following non-dimensional perturbation form of the w' equation:

$$\left(\frac{\partial}{\partial t} + \bar{U}\frac{\partial}{\partial x} + \bar{V}\frac{\partial}{\partial y}\right)\nabla^2 w^* - \frac{\partial^2 \bar{U}}{\partial z^2}\frac{\partial w^*}{\partial x} - \frac{\partial^2 \bar{V}}{\partial z^2}\frac{\partial w^*}{\partial y} = \tag{12}$$

$$\frac{-1}{R_o^*}\frac{\partial \zeta^*}{\partial y} - \frac{1}{R_o}\frac{\partial \zeta^*}{\partial z} + R_i \nabla_h^2 \theta^* + \frac{1}{R_z}\frac{\partial^2}{\partial z^2}(\nabla^2 w^*) + \frac{1}{R_h}\nabla_h^2(\nabla^2 w^*)$$

Likewise, the same procedure can be applied to the θ' and ζ' equations (9) and (11) respectively to yield:

$$\left(\frac{\partial}{\partial t} + \bar{U}\frac{\partial}{\partial x} + \bar{V}\frac{\partial}{\partial y}\right)\theta^* + w^*\frac{\partial \bar{\theta}}{\partial z} = \tag{13}$$

$$\frac{H}{U_T \rho_{oo}\Delta T}\left(\frac{\overline{\rho_o'Q'\bar{\theta}}}{cp\,\bar{T}}\right) + \frac{1}{P_z R_z}\frac{\partial^2 \theta^*}{\partial z^2} + \frac{1}{P_h R_h}\nabla^2 \theta^*$$

for θ^*

and

$$\frac{\partial \zeta^*}{\partial t} + \bar{U}\frac{\partial \zeta^*}{\partial x} + \bar{V}\frac{\partial \zeta^*}{\partial y} + \frac{\partial \bar{V}}{\partial z}\frac{\partial w^*}{\partial x} - \frac{\partial \bar{U}}{\partial z}\frac{\partial w^*}{\partial y} = \tag{14}$$

$$\frac{1}{R_o}\frac{\partial w^*}{\partial z} + \frac{1}{R_o^*}\frac{\partial w^*}{\partial y} + \frac{1}{R_z}\frac{\partial^2 \zeta^*}{\partial z^2} + \frac{1}{R_h}\nabla_h^2 \zeta^*$$

for ζ^*

Non-dimensional terms which appear as a result of these substitutions include:

$$R_z = \frac{U_T H}{\nu_z} = \text{vertical Reynolds number}$$

$$R_h = \frac{U_T H}{\nu_h} = \text{horizontal Reynolds number}$$

$$P_h = \frac{\nu_h}{\kappa_h} = \text{horizontal Prandtl number}$$

$$P_z = \frac{\nu_z}{\kappa_z} = \text{vertical Prantdl number}$$

$$Ri = \frac{g\alpha\Delta TH}{U_T^2} = \text{bulk Richardson number}$$

where α is the volume expansion coefficient for air

$$Ro = \frac{U_T}{fH} = \text{sine Rossby number}$$

$$Ro* = \frac{U_T}{f^* H} = \text{cosine Rossby number}$$

b. 3. Transformation -- The Normal Mode Assumption

A normal mode assumption of the following form is introduced for the non-dimensional variables:

$$w^* = W(k_x, k_y, \sigma, z)\exp(ik_x + ik_y + \sigma t)$$

$$\theta^* = \Theta(k_x, k_y, \sigma, z)\exp(ik_x + ik_y + \sigma t)$$

$$\rho_o Q' = P_o f(k_x, k_y, \sigma, z)\exp(ik_x + ik_y + \sigma t)$$

$$u^* = U(k_x, k_y, \sigma, z)\exp(ik_x + ik_y + \sigma t)$$

$$v^* = V(k_x, k_y, \sigma, z)\exp(ik_x + ik_y + \sigma t)$$

$$\zeta^* = Z(k_x, k_y, \sigma, z)\exp(ik_x + ik_y + \sigma t)$$

where k_x and k_y are the non-dimensional horizontal wave numbers and σ is the non-dimensional frequency which may be complex.

That is,

$$k_x = \frac{2\pi H}{L_x}, \quad k_y = \frac{2\pi H}{L_y}$$

where L_x and L_y are the horizontal wavelengths in the x and y directions respectively.

The above expressions are then substituted into the previously-derived non-dimensional equations (12), (13), and (14). Thus, these equations are "mapped" into the horizontal wavenumber and frequency domain, reducing the partial differential equations to ordinary differential equations, and introducing the characteristic value problem for the separation variable σ.

This procedure produces the following transformed ordinary differential equations:

$$\{[(ik_x\bar{U} + ik_y\bar{V} + \sigma) - \frac{1}{R_z}\frac{d^2}{dz^2} - \frac{1}{R_h}(\nabla_h^2)]\nabla^2 \tag{15}$$

$$-i(k_x\frac{d^2\bar{U}}{dz^2} + k_y\frac{d^2\bar{V}}{dz^2})\}W + (\frac{1}{R_o^*}ik_y + \frac{1}{R_o}\frac{d}{dz})Z$$

$$+ Ri(k^2)\theta = 0 \text{ for } W$$

$$[\sigma + i(k_x\bar{U} + k_y\bar{V}) - \frac{1}{P_zR_z}\frac{d^2}{dz^2} - \frac{1}{R_hP_h}\nabla_h^2]\theta + W\frac{d\bar{\theta}}{dz} = \tag{16}$$

$$\frac{H \bar{\theta} (P_o f(z))}{\rho_{oo} U_T \Delta T c_p \bar{T}} \text{ for } \theta$$

$$[\sigma + i(k_x \bar{U} + k_y \bar{V}) - \frac{1}{R_z} \frac{d^2}{dz^2} - \frac{V_h^2}{R_h}]Z = \qquad (17)$$

$$[-i (k_x \frac{d\bar{V}}{dz} + (\frac{d\bar{U}}{dz} - \frac{1}{R_o^*})k_y) + \frac{1}{R_o} \frac{d}{dz}]W \text{ for } Z$$

In equation (16), $P_o f(z)$ is the vertical distribution of the latent heating magnitude. Its determination is discussed later in this text.

The boundary value problem now becomes one of solving (15), (16), and (17) for W, θ, and Z and then using these results to solve for other diagnostic quantities. Note that V_h^2 may also be written as $- k^2$ in the k domain.

c. Diagnostic Equations

1. Computing Other Transform Variables

Using the results from the solution of the system (15), (16), and (17) we can easily compute other diagnostic quantities by using the transform definition and the appropriate scaling procedures.

To compute U and V, note that

$$ik_x V(z) - ik_y U(z) = Z(z)$$

and

$$ik_x U(z) + ik_y V(z) + \frac{dW}{dz} = 0$$

Manipulating these expressions yields:

$$U = i \frac{(k_y Z + k_x \frac{dW}{dz})}{k^2} \tag{18}$$

$$V = -i \frac{(k_x Z - k_y \frac{dW}{dz})}{k^2} \tag{19}$$

Having U and V, the horizontal non-dimensional divergence is:

$$\nabla_h \cdot V \langle -\rangle \; ik_y V + ik_x U \tag{20}$$

$$X = ik_y W - \frac{dV}{dz} \tag{21}$$

Reynolds stresses can be defined in terms of time or space mean correlation of two fluctuating quantities. For perturbed quantities describing the secondary flow, their cross-correlation at some point 1 is:

$$z(1) = \int_{-\infty}^{+\infty} w(r) \cdot \theta(1 + r) dr \; \langle -\rangle \; W^* \theta \tag{22}$$

where * denotes a complex conjugate. Other flux quantities may be represented in a similar manner. Details of computation are described in a later section.

Perturbation pressure P can also be obtained diagnostically but requires a bit more effort. To avoid excessive algebra, the derivation procedure will be described with only the salient results presented. The procedure is as follows:

Take $\frac{\partial}{\partial x'}$ (5), $\frac{\partial}{\partial y'}$ (6), $\frac{\partial}{\partial z'}$ (7)

This results in an expression for $\nabla^2 p'$ and after some manipulations we get:

$$\nabla^2 p' = \Phi \text{ (Poisson's Eqn.) where} \tag{23}$$

$$\Phi = -2\left(\frac{\partial \overline{\rho_o' w'}}{\partial x'} \frac{\partial \overline{U'}}{\partial z'} + \frac{\partial \overline{\rho_o' w'}}{\partial y'} \frac{d\overline{V}}{dz}\right) + g\alpha \frac{\partial \overline{\rho_o' \theta'}}{\partial z'} + f\zeta'$$

$$+ f^*\left(\frac{\partial \overline{\rho_o' \overline{U'}}}{\partial z'} + \frac{\partial \overline{\rho_o' u'}}{\partial z'} - \frac{\partial \overline{\rho_o' w'}}{\partial x'}\right) + \frac{\partial^3 \overline{\rho_o' w'}}{\partial z'^3}(\nu_z - \nu_h)$$

After substitution of the following scaling relations into (23):

$$\overline{\rho_o' w'} = \rho_{oo} U_T w^* , \quad \overline{\rho_o' u'} = \rho_{oo} U_T u^* , \quad \overline{\rho_o' \theta'} = \rho_{oo} \Delta T \theta^* ,$$

$$\zeta' = U_T \rho_{oo} \zeta^*/H, \quad \overline{U'} = U_T \overline{U} , \quad \overline{V'} = U_T \overline{V}$$

$$p' = P_{oo} p^*$$

where P_{oo} = a reference pressure

the non-dimensional form is yielded:

$$\nabla^2 p^* = \left[\frac{\rho_{oo} U_T^2}{P_{oo}}\right] \cdot \left\{-2\left[\frac{\partial w^*}{\partial x} \frac{\partial \overline{U}}{\partial z} + \frac{\partial w^*}{\partial y} \frac{\partial \overline{V}}{\partial z} + R_i \frac{\partial \theta^*}{\partial z} + \frac{\zeta^*}{R_o} + \right.\right. \tag{24}$$

$$\frac{1}{R_o^*}[\frac{\partial \bar{U}}{\partial z} + \frac{\partial u^*}{\partial z} - \frac{\partial w^*}{\partial x}] + [\frac{R_h - R_z}{R_z} \cdot \frac{1}{R_h}] \cdot \frac{\partial^3 w^*}{\partial z^3}\}$$

where the non-dimensional numbers have their previously defined meaning. Writing (24) in transform form yields:

$$[\frac{d^2}{dz^2} - k^2]P = [\frac{\rho_{oo}U_T^2}{P_{oo}}] \tag{25}$$

$$\cdot \{-2[k_x W \frac{d\bar{U}}{dz} + k_y W \cdot \frac{d\bar{V}}{dz}] + R_i \frac{d\bar{\theta}}{dz} +$$

$$\frac{Z}{R_o} + \frac{1}{R_o^*}[\frac{d\bar{U}}{dz} + \frac{\partial U}{\partial z} - ik_x W] + [\frac{R_h - R_z}{R_z} \cdot \frac{1}{R_h}] \cdot \frac{d^3 W}{dz^3}\}$$

This completes the set of governing equations in the linear model.

c. (2) Computation of Terms for the Energy Equation of the Secondary Flow

After Brown (1970) and Asai (1970), an expression for the kinetic energy of the secondary flow E_2 integrated over the fluid depth can be written (in dimensional form):

$$\frac{\partial E'_2}{\partial t} = \int_0^H \{ \overbrace{-(\overline{\rho_o' \overline{u'w'}} \frac{d\bar{U}'}{dz'} + \overline{\rho_o' \overline{v'w'}} \frac{d\bar{V}'}{dz'})}^{A} + \overbrace{g\alpha \overline{\rho_o' \overline{w'\theta'}}}^{B} + \tag{26}$$

$$\overbrace{(-\overline{\rho_o' \overline{u'\frac{\partial p'}{\partial x'}}} - \overline{\rho_o' \overline{v'\frac{\partial p'}{\partial y'}}} - \overline{\rho_o' \overline{w'\frac{\partial p'}{\partial z'}}})\frac{1}{\rho}}^{C} + \overbrace{\varepsilon_v}^{D}\} dz$$

where $\overline{\quad}$ represents Reynolds averaging in the dimensional

equations (26) and (27) of the designated variables over the horizontal domain and $\bar{\rho}$ is a mean density value over the integrated depth. In (26), term (A) represents the conversion between kinetic energy of the mean flow and that of the perturbation, term (B) is the conversion between potential and kinetic energy of the perturbation due to buoyancy, term (C) is the work done on the system by the perturbation pressure, and term D is the dissipation of perturbation kinetic energy due to viscosity. Term D was neglected by Brown for dry shallow convection in the PBL. However, this term should be computed for moist, deeper convection. After Chandrasekhar (1961), term D can be defined:

$$\varepsilon_v = \overline{\rho_o'w'(\nu_h\nabla_h'^2 w' + \nu_z\frac{\partial^2 w'}{\partial z'^2})} + \overline{\rho_o'u'(\nu_h\nabla_h'^2 u' + \nu_z\frac{\partial^2 u'}{\partial z'^2})} + \quad (27)$$

$$\overline{\rho_o'v'(\nu_h\nabla_h'^2 v' + \nu_z\frac{\partial^2 v'}{\partial z'^2})}$$

Substituting (27) into (26) and non-dimensionalizing where ___ denotes a Reynolds average yields:

$$\frac{\partial E_2^*}{\partial t} = \int_0^H \{ (-\rho_{oo}\overline{u^* w^*}\frac{d\bar{U}}{dz} - \rho_{oo}\overline{v^* w^*}\frac{d\bar{V}}{dz}) + \quad (28)$$

$$R_i\rho_{oo}\overline{w^* \theta^*} + \frac{\rho_{oo}^2}{\bar{\rho}} (-\overline{u^*\frac{\partial p^*}{\partial x}} - \overline{v^*\frac{\partial p^*}{\partial y}} - \overline{w^*\frac{\partial p^*}{\partial z}})$$

$$+ \rho_{oo}[\overline{w^*(\nabla_h^2 \frac{w^*}{R_h} + \frac{1}{R_z}\frac{\partial^2 w^*}{\partial z^2})}$$

$$+ \overline{u^*(\frac{\nabla_h^2 u^*}{R_h} + \frac{1}{R_z}\frac{\partial^2 u^*}{\partial z^2})} + \overline{v^*(\frac{\nabla_h^2 v^*}{R_h} + \frac{1}{R_z}\frac{\partial^2 v^*}{\partial z^2})}]\} \ dz$$

Here, cross-correlation quantities such as

$$\overline{u'w'} = \int_{-\infty}^{+\infty} u(r)^. w(1 + r)dr = \tag{29}$$

$$\int_{-\infty}^{+\infty} U^*(k)^. W(k)\exp(j2\pi kr)dk$$

Hence $\overline{u'w'} \longleftrightarrow U^*W$ where * signifies the complex conjugate.

Evaluating U^*W about its central ordinate in the wavenumber domain and assuming $\overline{u'w'}$ is a real function, then $U^*W = (U_r W_r + U_i W_i)$ where the imaginary, odd portion is dropped due to symmetry arguments.

Completing the transformation, terms A-D of (26) become:

$$-(U_r W_r + U_i W_i)\frac{d\overline{U}}{dz} - (V_r W_r + V_i W_i)\frac{d\overline{V}}{dz} \tag{A}$$

$$Ri[W_r \Theta_r + W_i \Theta_i] \ ; \ Ri = \frac{g\alpha\Delta TH}{U_T^2} \tag{B}$$

$$\frac{-\rho_{oo}}{\rho}[U_r(ik_x P)_r + U_i(ik_x P)_i + V_r(ik_y P)_r \tag{C}$$

$$+ \ V_i(ik_yP)_i \ + \ W_r(\frac{dP}{dz})_r \ + \ W_i(\frac{dP}{dz})_i \ ]$$

$$W_r(\frac{1}{R_z}\frac{d^2W}{dz^2} - k^2\frac{W}{R_h})_r \ + \ W_i(\frac{1}{R_z}\frac{d^2W}{dz^2} - k^2\frac{W}{R_h})_i \qquad (D)$$

$$+ \ U_r(\frac{1}{R_z}\frac{d^2U}{dz^2} - k^2\frac{U}{R_h})_r \ + \ U_i(\frac{1}{R_z}\frac{d^2U}{dz^2} - k^2\frac{U}{R_h})_i$$

$$+ \ V_r(\frac{1}{R_z}\frac{d^2V}{dz^2} - k^2\frac{V}{R_h})_r \ + \ V_i(\frac{1}{R_z}\frac{d^2V}{dz^2} - k^2\frac{V}{R_h})_i$$

where the subscripts "r" and "i" represent the real and imaginary parts of the complex function, respectively. Vertical derivatives and appropriate boundary conditions are evaluated in the standard manner to be discussed in Chapter V.

Using the above derivations, a flux Richardson number R_f integrated over the entire depth of the fluid is defined as:

$$R_f \ = \ \frac{|\int_0^H B \ dz|}{|\int_0^H A \ dz|} \ = \qquad (30)$$

$$\frac{|\int_0^H R_i[W_r\theta_r \ + \ W_i\theta_i]dz|}{|\int_0^H \{(U_rW_r \ + \ U_iW_i)\frac{d\bar{U}}{dz} \ + \ (V_rW_r \ + \ V_iW_i)\frac{d\bar{V}}{dz}\}dz|}$$

This is equivalent to the expressions derived by Asai (1970) and Sun (1978). The flux Richardson number is essentially a ratio of the production of perturbation kinetic energy due to buoyancy to the production of perturbation kinetic energy due

to shear interaction with the secondary circulations. Hence, small flux Richardson numbers signify the production of eddy kinetic energy is dominated by shear production while large values imply the shear production terms are negligible relative to the heat flux.

d. Closure Problems

In order to solve the linear system and then compute the diagnostic terms requires defining the base state input, diabatic heating term, and eddy diffusion coefficients in a physically reasonable manner. Once this is accomplished, we may consider all independent variables appropriately defined such that the system is closed and legitimate solutions can be obtained. However, determining a "physically reasonable" closure is difficult especially when parameterization of poorly-understood small scale processes is required. Furthermore, the parameterization must be obtainable without excessive computational expense --otherwise, no solution is possible!

In the following five sections, an approach to the closure problem is discussed along with its method of implementation in the model. Their selection was based on my review of the literature and relative ease of computation.

(1) Moisture Accession into the Model

As noted in the discussion on CISK, the appropriate closure for feeding moisture into the linear model is still open

to debate. Thus, the two principle approaches --cloud depth (CD) moisture accession and boundary layer (BL) moisture accession -- have been both used in this study. A derivation for the expression for the first approach follows:

For a given level in the atmosphere using the linearized anelastic perturbation equations, the large scale moisture convergence I is:

$$I = \nabla \cdot \overline{q}'(\overline{\rho_o}'\overline{v}') = \overline{q}'(\frac{\partial \overline{\rho_o}'u'}{\partial x'} + \frac{\partial \overline{\rho_o}'v'}{\partial y'} + \frac{\partial \overline{\rho_o}'w'}{\partial z'}) + \tag{31}$$

$$(\overline{\rho_o}'u'\frac{\partial \overline{q}'}{\partial x'} + \overline{\rho_o}'v'\frac{\partial \overline{q}'}{\partial y'} + \overline{\rho_o}'w'\frac{\partial \overline{q}'}{\partial z'})$$

letting $\overline{q}'$ = uniform large-scale moisture supply over the horizontal domain

$$\frac{\partial \overline{q}'}{\partial x'} = \frac{\partial \overline{q}'}{\partial y'} = 0$$

Also

$$(\frac{\partial \overline{\rho_o}'u'}{\partial x'} + \frac{\partial \overline{\rho_o}'v'}{\partial y'} + \frac{\partial \overline{\rho_o}'w'}{\partial z'}) = 0$$

from the anelastic continuity equation. Then

$$\nabla \cdot \overline{q}'\overline{\rho_o}'\overline{v}' = \overline{\rho_o}'w'\frac{\partial \overline{q}'}{\partial z'} \tag{32}$$

Now, the vertically-integrated moisture convergence through a column of unit horizontal area in the atmosphere is (keeping w' = 0 at the lower boundary):

$$M_t = \int_0^{\infty} \overline{\rho_o' w'} \frac{\partial \overline{q}'}{\partial z'} \, dz' = \int_0^{z_t} \overline{\rho_o' w'} \frac{\partial \overline{q}'}{\partial z'} \, dz' \tag{33}$$

assuming the moisture gradient drops sharply above cloud top. Here, z_t is the cloud top with the integral contribution above that level assumed as negligible.

Breaking (33) into parts:

$$M_t = \int_0^{z_b} \overline{\rho_o' w'} \frac{\partial \overline{q}'}{\partial z'} dz' + \int_{z_b}^{z_t} \overline{\rho_o' w'} \frac{\partial \overline{q}'}{\partial z'} dz'$$

$$= \overset{A}{\overline{\rho_o' w_b'} \cdot (\overline{q}'_{bl} - \overline{q}'_o)} + \int_{z_b}^{z_t} \overset{B}{\overline{\rho_o' w'}} \frac{\partial \overline{q}'}{\partial z} dz' \tag{34}$$

In term A, w_b' is defined as the perturbation vertical velocity at the cloud base or characteristic of the mean in the boundary layer. z_b is the height of the cloud base. $\overline{q}'_{bl}$ and $\overline{q}'_o$ represent simply the base state moisture at the top and bottom of the boundary layer. This term, although included in the model formulation, appears to have little effect on the results.

Term B is by far the dominant term. It is integrated numerically in the matrix using a trapezoidal scheme. The exact numerical formulation is shown later. When L multiplies B, convective warming results (Rao and Hassebrock, 1972; Mathur, 1975).

The expression for the second approach of boundary layer

moisture accession is more intuitive. Syono in 1944 and 1950 proposed that the rate of precipitation in a typhoon r, be expressed as a product of the mixing ratio q^* and the vertical velocity at the top of the friction layer ω^* (Syono and Yamasaki, 1966). Specifically,

$$r \doteq \int_0^{P_s} (\nabla \cdot Vq)dp = \omega^* q^* \qquad (35)$$

where the integration was performed with respect to pressure. Ooyama (1964, 1969) supported this closure where heating is proportional to the horizontal convergence of moisture in the boundary layer. Others such as Koss (1976), Stevens and Lindzen (1977), Sun (1984, 1987), and Wang (1987) have used this closure. However, Mak (1981) stated that both (34) and (35) would give essentially the same result. Results from both approaches will be compared later in this study.

An implicit assumption in (34) and (35) is that the moistening parameter "b" is zero -- that is, all of the moisture convergence in the cloud or heating layer is converted to precipitation. Kuo (1974) stated that it is safe to assume b to be smaller than 1 (e.g., 0.05) over most of the tropics. In addition, Krishnamurti, Low-Nam, and Pasch (1983), using GATE data sets, showed that it was necessary during periods of active easterly waves to augment the large-scale moisture supply using a mesoscale convergence parameter η. From their study, when both the time-averaged η and b were computed for a

19 day interval in GATE, the precipitation efficiency P ,
defined as:

P = (1-b)   after Kuo (1974)

P = (1-b)*(1+η)   after Krishnamurti et al.
(1983)

is ~ 1.0 in both equations. Dudhia and Moncrieff (1987) found
that b ~ 0 during their 3 hour simulation of a tropical convec-
tive band. McBride (1988) found the weighted moisture tendency
term (I * b) was also very small, equivalent to setting b=0 for
a "free ride". However, during periods of widespread mesoscale
convergence P may well exceed 1.0.

Theoretically, b cannot be less than zero. As b --> 0,
the large scale lapse rate approaches that of the moist adia-
bat. Krishnamurti et al. have allowed P, the precipitation
efficiency, to exceed one by introducing the mesoscale non-
measurable convergence parameter η. η can vary from 0 to 1.0
during highly disturbed periods and allows for moistening (b >
0.0) during such periods where strong moisture diffusion may
still exist.

"b" may be computed using the large scale relative humi-
dity (Anthes, 1977). The hypothesis is, that if the large-
scale environment is sufficiently humid, most of the moisture
convergence will be converted to rain while if it is dry a
greater fraction will be used to moisten the environment. The
suggested relationship is:

$$b = [\frac{(1 - \langle RH \rangle)}{(1-RH_c)}]^n \ , \ \langle RH \rangle \geq RH_c \tag{37}$$

$$b = 1 \ , \ \langle RH \rangle < RH_c$$

Here, $\langle RH \rangle$ is the column mean relative humidity integrated over the cloud depth and RH_c is a critical value. A limitation of this approach is that the rainfall rate can never exceed the large-scale moisture convergence. Anthes (1977) suggested values of 1 and 0.5 for n and RH_c respectively which may be empirically adjusted. Kuo and Anthes (1984) adjusted these values in semi-prognostic tests to match observed rainfall rates associated with a convective episode during the SESAME 1979 program. The best fit adjusted values were n ~ 2.5 and RH_c ~ .35. "b" was computed for both sets of constants for varying core radii (cloud heights) for each deep convective base state. These results are displayed in Table 6.2. Evidently, the fitted constants closely match Kuo's (1974) assumption. For future numerical modeling, one might set b < .10 in the eastern Arabian Sea but > .10 in the central Arabian Sea during monsoon.

(2) Vertical Distribution of Heating and Cloud Models

It is well known that cumulus convection distributes amounts of latent and sensible heat in the vertical. In turn, the release and re-distribution of energy by small-scale convective cells can significantly affect the evolution of mesoscale circulations. With respect to the linear model, the prob-

lem is to incorporate the convective transports of heat, moisture, and momentum which cannot be explicitly resolved by the model into the diabatic heating term in the thermodynamic energy equation.

Cumulus parameterization schemes have been traditionally divided into two classes: (a) convective adjustment and (b) cloud model schemes. In the convective adjustment method, the effect of cumulus convection on the environment is considered by adjusting the model's moisture and thermodynamic fields toward a moist neutral state. However, such simple schemes cannot adequately describe the interaction of cumulus convection with the large-scale environment and the subsequent response of the linear system.

The second scheme, the cloud model scheme, considers the effect of subgrid-scale penetrative convection on the large scale equations by a model of the cloud themselves. The primary goal with this scheme is to determine the vertical extent or distribution of convective heating caused by the clouds. Schemes of this type used in modern numerical weather prediction are called Kuo-type schemes (1965, 1974) which couple cloud columnar moisture accession with a temperature differential (or other parameter) describing the vertical distribution of convective heating. Since the linear model and its base state already provide the parameters necessary for the moisture accession, the role of the parameterization scheme becomes (1) to provide the vertical extent of the cloud and (2) the

vertical distribution of heating associated with the convection.

One variant of the Kuo-type scheme which has been used in hurricane models is the Anthes (1977) scheme. In this scheme, a one-dimensional steady state (1DSS) cloud model is used to provide the necessary parameters for convective heating determination. The basis for the Anthes approach is that the vertical distribution of heating is a function of the area-averaged condensation rate. The area-averaged rate (after normalization) in turn requires a knowledge of the in-cloud humidity, the cloud environment humidity, the entrainment rate of mass into the updraft, the cloud top height, the cloud base vertical velocity, and the percent area covered by the clouds at cloud base. (The last two parameters drop out when this term is normalized). This term is then normalized by its vertical average whose result is the vertical distribution function which is then entered in the diabatic heating term of the linearized thermodynamic energy equation.

Specifically, $\bar{C}^*$, the area-averaged condensation rate is defined as:

$$\bar{C}^* = -w_b a_b \frac{M}{M_b} \cdot [\frac{\partial q_c}{\partial z} + (q_c - q_e) \cdot \frac{1}{M} \frac{dM}{dz}] \tag{38}$$

where a is the percent area covered by cumulus clouds at cloud base, w_b is the vertical velocity at cloud base, q_c is the cloud specific humidity, q_e is the environmental specific

humidity, M is the total mass flux across a particular level, and M_b is the mass flux at cloud base. The mass at any pressure level going up (according to Anthes, 1977 under a hydrostatic approximation) is:

$$M(p) = M_b \left(\frac{p}{p_b} \right)^{\frac{-R_d \bar{T} \mu}{g}} \tag{39}$$

where p is pressure, μ is an entrainment factor ($= 1/M$ dM/dz) inversely proportional to cloud radius, R_d is the dry adiabatic gas constant, and $\bar{T}$ is the mean temperature of the cloud. In order to "top" the vertical profile, in the upper 10% of the cloud's pressure depth:

$$M(p) = ((p-p_u)/(p_d-p_u)) * M(p_d) \ ; \ p_u < p < p_d \tag{40}$$

where p_d is the pressure level where detrainment begins (p_d = cloud top pressure plus 10 percent of the cloud pressure depth differential) and p_u is the upper pressure level (cloud top). Then N(z), the normalized vertical distribution of condensational heating is:

$$N(z) = \bar{C}^*(z)/\langle \bar{C}^* \rangle = \tag{41}$$

$$\frac{- M(z) \cdot [\frac{\partial q_c}{\partial z} + (q_c - q_e)\mu]}{-(z_t-z_b)^{-1} \int_{z_b}^{z_t} M(z)[\frac{\partial q_c}{\partial z} + \mu(q_c - q_e)] \ dz}$$

where z and p are the corresponding height and pressure levels

in the 21 level model. M(p) and M(z) are related hydrostatically. The cloud model provides the necessary variables for computation of this quantity including cloud top. However, the cloud model itself must be provided a core radius. The entrainment factor will be discussed in detail later in the cloud model discussion. The vertical integration is performed using the trapezoidal rule.

In (41), the term $\frac{\partial q_c}{\partial z}$ may be viewed as the core or updraft scale vertical advection of cloud moisture. The second term is a dilution term due to entrainment and acts to oppose the first term. Hence, the smaller the core radius of the cloud, the greater the dilution for a given environment.

Although, the final partitioning of convective heating depends on vertical eddy fluxes as well as $\bar{C}^*$, the major component of convective heating is $\bar{C}^*$. Some profiles of $\bar{C}^*$ / $\langle\bar{C}^*\rangle$ are presented in Chapter VII. In the condensation heating profile, the effects of ice are included in the cloud model. The role of frozen precipitation here is to shift slightly higher the heating distributions within the cloud boundaries.

2(a). The inclusion of the effects of sensible heating on the environment.

It is possible using the cloud model data to include the sensible heat transports in the vertical heating profile following Kuo and Raymond (1980).

The overall effect of cumulus convection is to warm its surroundings. Sensible warming occurs as a result of the following processes:

(i) T_{11} , the net upward transport of sensible heat into a layer Δz inside the cloud and the downward transport of cooling through convective moist downdrafts in the immediate environment and

(ii) T_{12}, the compressional heating created by the slow descending motions in the distant environment.

The mean heating due to (i) is defined as:

$$\frac{\partial T_{11}}{\partial t} = \frac{-1}{\pi_o \rho} \frac{\partial}{\partial z}(\rho T^*_\theta) \tag{42}$$

where $T^*_\theta = (1-\alpha_2 \, a \, k)a_o w_c \theta'_c$, $\theta'_c = \theta_c - \theta_o$

The mean heating due to (ii) is defined as:

$$\frac{\partial T_{12}}{\partial t} = (1-\alpha_2 k) \cdot \frac{a_o w_c}{\pi_o} \cdot \frac{\Delta \hat{t}}{\hat{t}} \frac{\partial \theta_o}{\partial z} \tag{43}$$

In the above, the empirical constants are $\alpha_2 = 0.4$, $a = -0.1$, k (area of moist downdraft/area of updraft) $= 1$ and $a_o = (A_c/A) = 0.1$. Also,

$$\Delta \hat{t}_i = \sum_{i=1}^{i} \Delta t \;;\; \hat{t} = \sum_{i=1}^{N} \Delta t \tag{44}$$

and π_o is the Exner function.

The dominant effect of cumulus convection is to warm the atmosphere through latent heat release. This means heating due to this process is defined as:

$$\frac{\partial T_2}{\partial t} = -a_o \frac{L}{c_p} w_c \left[\frac{\partial q_c}{\partial z} - \mu(q_e - q_c)\right]$$

Then, the total heating is simply:

$$\frac{\partial T}{\partial t} = \frac{\partial T_{11}}{\partial t} + \frac{\partial T_{12}}{\partial t} + \frac{\partial T_2}{\partial t} = \frac{\partial T_1}{\partial t} + \frac{\partial T_2}{\partial t} \tag{45}$$

Dividing through all terms by

$$\frac{a_o w_c L}{c_p}$$

and incorporating the above $(\frac{\partial T}{\partial t})$ into the Anthes (1977) scheme

$$N(z) = \frac{(z_t - z_b) * M * (\frac{\partial T}{\partial t})}{\int_{z_b}^{z_t} M * (\frac{\partial T}{\partial t}) dz} \tag{46}$$

The variables Δt, θ_c, w_c, $\hat{t}$, and q_c are provided by the cloud model. In 1DSS models, development time $\hat{t}$ is often equated with cloud life span. Chapter VII includes profiles of the normalized total and sensible heating rate as well as the normalized condensation rates for selected base states. These indicate that with respect to sensible heat transport, deep convection tends to warm the upper part and cool the lower part of the convective layer. However, most of the convective heating rate is contributed by the area-averaged condensation rate

$\overline{C}^*$.

It should be noted that (45) represents only the influence of convection on the surrounding environment and does not include the mutual interaction of updrafts and downdrafts. For example, while cool moist downdrafts increase the mean sensible heat transport upwards (42), they may also reduce the cloud vertical velocity thus somewhat minimizing its role in transporting heat upwards. Similarly, the contribution of compressional heating (43) to the sensible heat transport would be offset by the reduction in latent heat release.

(2) b. The Cloud Model

A one-dimensional steady-state cloud model similar to that developed by Simpson and Wiggert (1969) is used to close the convective heating scheme. This simple model avoids the more costly and sometimes unstable aspects of time integration but provides robust results incorporating the major aspects of cumulus cloud development including entrainment and simple microphysics.

The model may be viewed as an entraining jet within a quasi-Lagrangian framework which traces the rise of a parcel through a particular level. The model assumes that e rainment through the cloud sides is inversely proportional t oud or tower radius. With this model, plots of w and other variables as functions of height represent mean properties of the active

tower as it rises through a level. An exact definition of the tower or core radius does not exist. For this model, the core radius may be determined either photogrammetrically or by specifying a vertical velocity threshold.

The primary equation of the model is the vertical velocity equation

$$\frac{d(\frac{w^2}{2})}{dz} = \frac{g*B}{1 + \alpha} - gQ_{lw} - \mu w^2 \qquad (47)$$

where w is the vertical velocity, g is gravity, μ is the entrainment rate, α is the virtual mass coefficient which compensates for the neglect of pressure perturbations and Q_{lw} is the total liquid water content. The buoyancy is defined as:

$$B = \frac{(T_v - T_{ve})}{T_{ve}} \qquad (48)$$

where T_v and T_{ve} are the virtual temperature of the updraft and environment, respectively. The mass entrainment rate ($\frac{1}{M}\frac{dM}{dz}$) is:

$$\mu = \frac{.183}{R} \qquad (49)$$

where R is the updraft or core radius. This expression is derived from the theoretical work of Levine (1959). The procedure is to first compute the updraft sounding independently of (47) and to determine the buoyancy and liquid water content. Then (47) is integrated upward from cloud base. The

precipitation formation and fallout is calculated simultane-
ously during the march upward.

The 1DSS model consists of 321 levels through a 16 km
depth with 50 m spacing between levels. The cloud base is
equated to the lifting condensation level which itself is
determined from surface values of temperature and moisture.
The updraft sounding is calculated beginning at this point
using the equation

$$dT = \frac{-Ldq_s}{(1 + 1.9*q_s) \cdot c_{pm}} \qquad (50)$$

where q_s is the saturation mixing ratio, c_{pm} the specific heat
at constant pressure for moist air, and L is the latent heat of
phase change.

To compute T and q, the parcel is first lifted from z to z
+ Δz conserving potential temperature and mixing ratio. Then,
the temperature and mixing ratio are modified by entrainment
according to the formula:

$$X_c = \frac{X_c + [\exp(\mu\Delta z) - 1]X_e}{\exp(\mu\Delta z)} \qquad (51)$$

where X_c is the cloud property before mixing, X'_e is the
environmental property, and X'_c is the cloud property after
mixing. Following this mixing step, if the parcel is supersa-
turated, q_s is reduced and T is increased iteratively by (50)
until saturation is reached. The condensate from each step is

saved for use in the later calculation of liquid water. The process is repeated until the parcel is no longer supersaturated or reaches 50 mb.

For convectively unstable soundings and larger core radii (reduced entrainment), the cloud towers will extend well above the freezing level. To account for this in the manner of Simpson and Wiggert (1971) and Kuo and Raymond (1980), freezing of the supercooled water is linearly interpolated through a transition or "slush" zone. To maintain rough fidelity with heterogeneous nucleation curves (Cotton, 1972 fig.1) and avoid model distortion, the model slush zone is defined from -10C to -40C with complete freezing occurring at and below the lower temperatures. Additional heat release will come from two factors --the latent heat of fusion and the saturation vapor differential between ice and water. A reliable equation for saturation mixing ratio over ice (between 0C and -50C) is:

$$Q_{ci} = (\frac{3.8}{p}) \cdot 10^{**}(\frac{9.5(T-273)}{T-8}) \tag{52}$$

from Ogura and Takahashi (1971). Ice crystal microphysics is beyond the scope of this study.

The equations for the change of Q_{cw} and Q_{rw} over a height interval Δz are written as:

$$\Delta Q_{cw} = (\Delta Q_{cw})_{cond} - (\Delta Q_{cw})_{auto} - (\Delta Q_{cw})_{collect} \tag{53}$$

$$\Delta Q_{rw} = (\Delta Q_{lw})_{auto} + (\Delta Q_{cw})_{collect} - (\Delta Q_{rw})_{fallout} \qquad (54)$$

$$(\Delta Q_{cw})_{auto} = k_1 \Delta t (Q_{cw} - a) \; ; \; Q_{cw} \geq a \qquad \qquad (55)$$

Here, a is the threshold cloud water (.5 g/m**3) at which conversion is assumed to begin. The subscripts "cw", "rw", and "lw" denote respectively, cloud water, rain water, and total liquid water. The terms "cond", "auto", "collect", and "fallout" refer to the conversion processes of condensation, autoconversion, collection, and fallout respectively, for the water budget terms. The time step Δt is $\Delta z/w$ where w is restricted to be greater than .01 m/s. Using the computed time step,

$$(\Delta Q_{cw})_{coll} = (5.26 \times 10^{-3}) Q_{cw} (Q_{rw}^{.875}) \Delta t \qquad (56)$$

$$(\Delta Q_{rw})_{fall} = \frac{Q_{rw} V_t \Delta t}{R} \qquad (57)$$

where Q_{cw} and Q_{rw} are expressed in g/m**3, V_t is the terminal velocity of the median cloud drop and R is the updraft core radius. Here

$$V_t = 5.1 (Q_{rw}^{0.125}) \quad (ms^{-1}) \qquad (58)$$

Following Simpson and Wiggert (1971), the terminal velocity of ice particles is reduced to 70% of the water droplets'. The effect is to reduce the fallout rate , thus increasing the drag and reducing slightly the cloud top height for very deep con-

vection.

Computing changes in cloud and rain water over each interval Δz, Q_{1w} is known and (47) is integrated upward. For Δt, the previously calculated vertical velocity is utilized. Cloud top is defined as the level at which w decreases below .01 m/s. The updraft is initialized by assuming w = 1 m/s at cloud base.

Results of some 1DSS model runs are displayed in Table 6.1, Chapter VI. Time here is simply the summation of time steps during the vertical integration over the cloud depth:

$$\hat{t} = \sum_{i=1}^{N} \Delt \qquad \text{(development time)} \qquad (59)$$

One may equate the total cloud life time and development time.

The precipitation rate (Kuo and Raymond, 1980) is defined as:

$$P_r = \sum_{i=1}^{N} \Delta\hat{t}_i V_t (\Delta Q_{rw})_{fall} / \hat{t} \qquad (60)$$

where $\Delta\hat{t}_i$ is the time for development of the cloud through the ith layer as previously defined.

While the 1DSS model enjoyed cloud height observational successes during its Florida cumulus seeding tests, limitations exist:

(1) The model only represents the actively growing phase of a cloud; in the tropics its rainfall cannot necessarily be

equated to that reaching cloud base or the ground.

(2) Cloud dimension or radius must be specified; It cannot predict cumulus structure and development ahead of time.

(3) It does not incorporate the effects of vertical shear which may suppress cloud tower development.

(4) Cloud radius is invariant with height in the formulation used in the linear model. This violates the requirement for mass continuity.

The microphysical and thermodynamic terms were evaluated in a non-linear one dimensional time dependent cloud model (1DTD) patterned after Weinstein (1970) designed to accentuate the potential for growth through dynamic seeding (introduction of ice nuclei above the freezing level to assist growth through latent heat release). Like Simpson and Wiggert, the Weinstein 1DTD model had been used with operational success and was a modification of the Weinstein-Davis (1968) 1DSS model. Integrations were accomplished using the Upstream N method of Molenkamp (1968) for the advection terms and Srivastava (1967) boundary conditions. Besides confirming the stability of the 1DSS thermodynamic terms, it verified the tendency for growth or non-growth above the freezing level in four of the five base states. Integrations were terminated after two hours of model time (1440 5 sec time steps). Contour plots of vertical velocity versus time and height are shown in Fig. 6.5 (Chapter VI) for the different base states.

Also, runs were made using a variable core radius in the 1DSS cloud model based on a formulation suggested by Cotton (1972). This procedure was not tested extensively. However, results suggest that in the Lagrangian formulation, the introduction of a variable radius reduces the cloud height somewhat for larger cores (> 1000 m). In addition, a different procedure for computing the mass flux in the condensational heating profile involving summation rather than a deep layer mean value is being tested. The net effect on the condensational heating profile of the variable radius and summed mass flux schemes is still under investigation. However, these formulations appear to lower the height level of maximum heating slightly.

c. The Estimation of Eddy Viscosity

A major closure problem exists in the determination of subgrid-scale eddy diffusion. Following Sun (1978), first order, constant but anisotropic assumptions are utilized. The ratio of horizontal to vertical diffusion is set at 100. This anisotropic ratio is supported by the discussions of Priestley (1962), Ray (1965), and Agee (1975) under conditions of stable stratification ($\frac{d\theta_e}{dz} > 0$) and the anisotropic eddies associated with large convection cells. The effect of this ratio is to enhance the so-called "short-wave cut-off" --that is, have the maximum of growth rate lie within the wavenumber domain under consideration.

The Prandtl number, defined as $\frac{v}{\kappa}$ or the ratio of the eddy to thermal diffusion coefficients, is usually set at about 0.7 to 1.0 for air. Lipps (1971) in a numerical study of longitudinal secondary circulations in an unstable stratification showed that increasing the Prandtl number significantly (from 0.7 to 9.25 while holding the Rayleigh number constant) reduced the momentum flux while having little effect on the eddy transfer of heat. Limited tests with the linear model holding v fixed but increasing the Prandtl number to 9 indicated the primary result was to eliminate the short wave cut-off and slightly increase the flux Richardson number. For convenience, the Prandtl number was defined as 1.0 throughout this study (Chandrasekhar, 1961).

Having made the above assumptions, the relevant problem becomes one of determining values for the eddy diffusion coefficients. Previous linear studies have used a wide range of diffusion coefficients. For example, Sun (1978) and Asai (1970, 1972) used fixed values of 250 and 100 m**2/s. Based on this linear system's response, both values seem somewhat high for bands with smaller convective cores (R=1000m or less). Furthermore, since a variable cloud size and depth is allowed for, it would seem logical to tie the eddy diffusion magnitude to the size and intensity of the convection.

One method used in convection studies is to use forms of the Smagorinsky-Lilly method which is essentially a product of the grid- scale velocity and eddy scale separation (Lilly,

1962). Asai and Kasahara (1967), in their study of compensating motion associated with clouds, defined a lateral mixing coefficient ν that is proportional to the velocity variation across the boundary of the cloud times the radius squared of the cloud updraft region:

$$\nu = 1^2 \left|\frac{\partial w}{\partial r}\right| \; ; \; 1 = \alpha a \tag{61}$$

where a is the radius of the updraft region and α is a constant which may vary from .1 to 1. Summarizing the Lilly-Smagorinsky two-dimensional approach, Xu (1988) defined the Smagorinsky eddy viscosity coefficient for the 1963 2D general circulation model as:

$$\nu_e = (k\Delta)^2 D \tag{62}$$

and the Lilly (1962) form including a convective stability parameter:

$$\nu_e = (k\Delta)^2 [D^2 + \max(-N_w^2 P_r^{-1}, 0)]^{0.5} \tag{63}$$

where

$$N_w^2 = \frac{g}{\theta_o} \frac{\partial \theta_e}{\partial z}$$

In (62) and (63) $k \sim .4$, Δ is the mesh separation distance, and D is the deformation tensor. In (63), only convective instability makes a contribution to the turbulent energy generation.

Cotton (1975) used a Smagorinsky formulation to compute the eddy viscosity at the center of the convective core:

$$K_{m(r=0)} = \frac{(k_1 \Delta z)^2}{\sqrt{2}} \left| 2\left(\frac{\partial \overline{w}}{\partial z}\right)^2 \right|^{0.5} \tag{64}$$

where

$$\Delta z = [\pi R^2 (\delta z)]^{1/3}$$

and $k^{\sim} = 0.21$

Here, $\overline{w}$ is the vertical velocity averaged over the scale length Δz where δz is the vertical grid spacing and R is the cloud tower radius. k is set at 0.21. Centered differences are used to approximate $\frac{\partial \overline{w}}{\partial z}$.

Equation (64) was used to provide estimates for the vertical diffusion coefficient in the linear model. The cloud model vertical velocity is equated to $\overline{w}$ based on Simpson and Wiggert's (1969) definition of w as a mean tower rise rate in a quasi-Lagrangian reference frame.

The eddy viscosity coefficient is then computed at each level in the model cloud, summed over all levels and divided by the total number of levels in the cloud. This mean cloud layer isotropic diffusion coefficient is then provided to the linear model as an estimate of the vertical eddy diffusion coefficient to complete the closure.

The linear model K_z is thus a function of cloud size and vertical velocity. The cloud model results of Chapter VI show values computed for individual base states as a function of core radii. Highest estimates are found for the most convectively unstable base states and largest cloud cores while lowest viscosity coefficients are computed for the more stable base states and smallest core radii. Agee (1975) estimated vertical coefficients of ~ 10 m**2/s near banded cirrus and ~100 m**2/s for Cb anvils. Krishnamurti (1975) used isotropic values of 30 m**2/s for unstable open cell oceanic convection. Lin et al. (1988) computed coefficient values of about 20 m**2/s for the lower levels of a Colorado microburst. In spite of the uncertainty surrounding these numbers, the greatest influence on the results is probably due to the anisotropic ratio. This will be discussed briefly in Chapter IX.

(4)   Insertion of the Base State Wind Profile

A third area of concern in closing the linear system is determining the appropriate base state U and V components and their first and second vertical derivatives. Many previous linear studies have used smooth analytic profiles (such as Asai (1970), Sun (1978), Mak (1983), and Kuo and Seitter (1985). While this is undoubtedly beneficial when testing general profiles and the system's response, it is doubtful that analytical functions can represent the full character of the observed wind in most instances, especially the more subtle maxima/minima.

A first try at solving this problem might be to put the actual wind in the model and determine the first and second derivatives at each level using a higher order finite difference scheme. However, such an approach leaves no freedom to determine to what extent detail is desired in the vertical profile. Furthermore, this method implies no error exists in the wind observation itself. All "noise" or small features are thus assumed relevant to the problem. Experience also shows, at least with respect to the eigenfunctions, that considerable noise is introduced into the solution which might partially mask the significant patterns.

A second approach is to smooth the data either by "hand" or using some simple numerical technique such as a 3 channel smoother. While the former procedure may be suitable if the individual is familiar with the data and working with a limited amount so that proper care can be taken, this may produce an unintended bias in the results. The concept of numerical smoothing has utility when the least squares procedure is not rigorously valid and may provide a better fit to the data by decreasing X^2. For the monsoon profiles, both a 3 point running average smoother and a 3 channel weighted smoother were tested. In both cases, the wind amplitudes were considerably reduced. These weaker speeds were not representative of those observed and the smoothing approach was discarded.

A third approach --one employed in this study, is to fit the observed wind with a least-squares polynomial whose order

may be varied. When applied rigorously, the least-squares method provides the most unbiased estimate with errors which approximate the uncertainties of the parent distribution. This method thus accounts for error in the observation and allows for variable "detail" through changing the order of the polynomial. To compute the first and second derivatives, the fitted wind data is then approximated by a low order interpolating polynomial whose derivatives give smaller truncation error than using a standard finite difference scheme at each level.

For the model, a Legendre polynomial subroutine (Bevington,1969) was used to fit the wind data. It allows for an order variation from 1 to 9 and uses a matrix inversion method to compute the higher order coefficients. A general form for the orthogonal Legendre polynomial is:

$$y = a_o P_o(x) + a_1 P_1(x) + \ldots = \sum_{L=0}^{N} [a_L P_L(x)] \tag{65}$$

where x, y are the data pairs to be fitted and

$$P_L(x) = \frac{1}{L}[(2L - 1)x P_{L-1}(x) - (L - 1)P_{L-2}(x)]$$

A popular cubic spline routine (Gerald and Wheatley, 1985) was used for interpolation of the fitted data and subsequent computation of the first and second derivatives. The cubic spline procedure retains smoothness where the function is smooth and avoids violent behavior near local irregularities which could

affect derivatives computed using a finite difference technique applied to the fitted data.

Thus, the base state wind can be handled numerically within the model code and the only requirement is specification of the desired polynomial order. Based on visual inspection of the fits, a 3rd order and 9th order fit were chosen in most instances to represent "smooth" and "detailed" profiles for comparison of the linear system response.

(5) Non-Precipitating Moist Convection and Surface Fluxes

It is generally recognized that shallow, non-precipitating convection should be treated in a manner fundamentally different from deep precipitating convection (Kuo, 1974, Frank, 1983). The shallow clouds generally have tops less than 3 km above the surface and do not involve a net release of latent heat when averaged over their lifetimes. The western Arabian Sea is characterized by shallow non-precipitating convection as revealed by aircraft film and satellite imagery (see Chapter VIII). Because this shallow convection interacts with the subsidence inversion and serves as an extended eddy to transport heat, moisture, and momentum between the subcloud layer below and subsiding layer above, it seems necessary that an attempt be made to include shallow clouds in the linear analysis.

Betts (1973) proposed a two layer lapse rate model to

parameterize the diabatic heating produced by the cloud. Betts notes that the mean atmosphere was modified even by non-precipitating convection because water condensed at one level is advected to another before evaporation. Convection warms the lower part of the cloud layer through condensation, transports liquid water upward and cools the upper part through evaporation. This heat transfer is a destabilizing process which, in the absence of large scale subsidence, will cause the cumulus layer to deepen until precipitation occurs. The evaporative cooling occurring in the sub-inversion layer will accentuate the temperature change across the inversion. The Betts two layer lapse rate scheme seems especially suited for the linear model since it can be included in terms of the eigenfunctions necessary for system closure and does not require specification of liquid water content.

The governing equation for the shallow cloud layer diabatic heating is:

$$\frac{\partial \tilde{\theta}}{\partial t} = -w\frac{\partial \tilde{\theta}}{\partial z} - \frac{\partial(\overline{\rho c_p \overline{w'\theta'}}_1)}{\partial z} \tag{66}$$

where $\tilde{\ }$ denotes an areal average, w is the convective scale vertical velocity and $'$ denotes deviations from the areal mean. A schematic (Fig. 4.1) may help explain the model. In Figure 4.1, Term A: $- w \frac{\partial \tilde{\theta}}{\partial z}$ is effectively already in the thermodynamic energy equation.
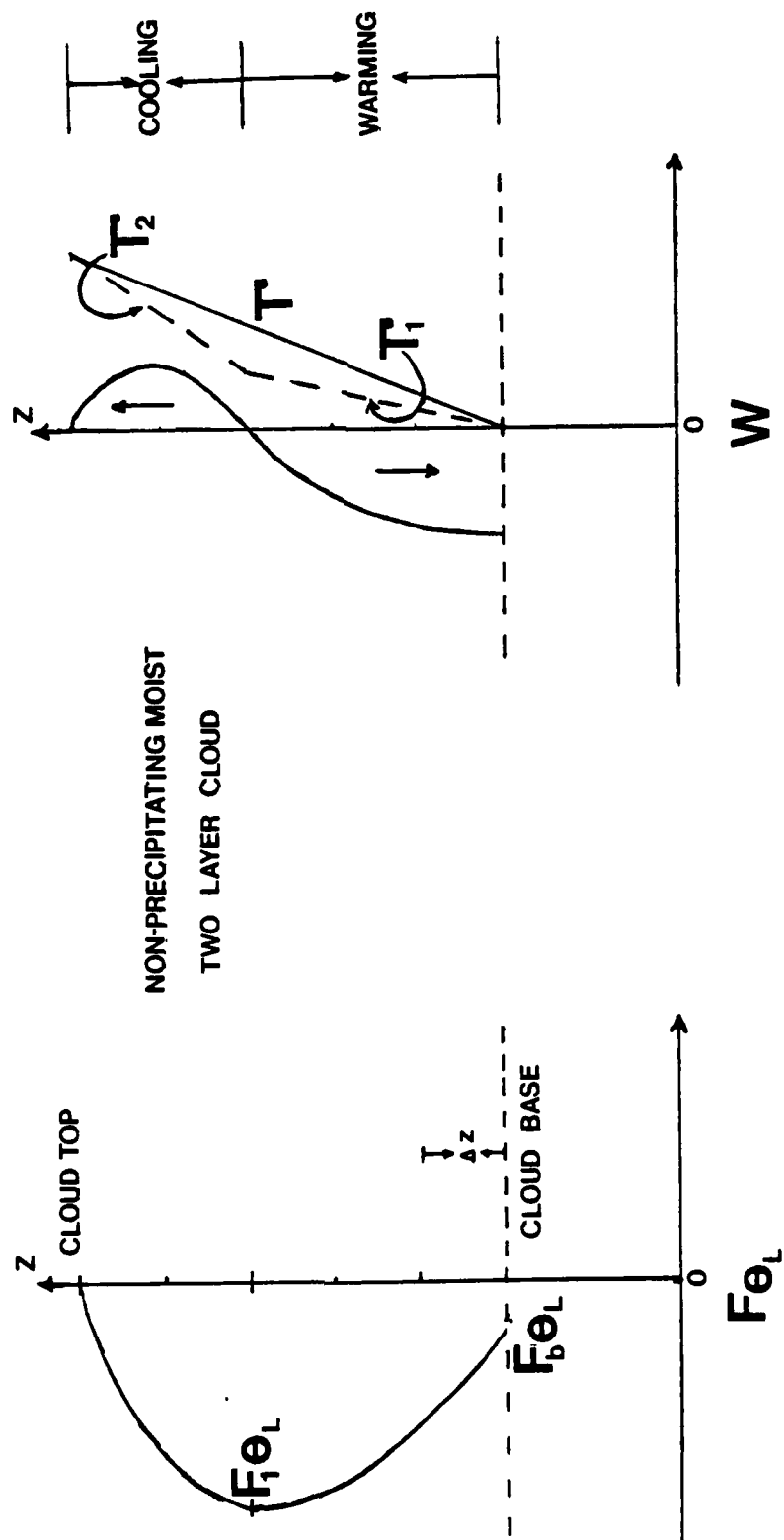
Fig. 4.1. Betts Two-Layer Cloud Model for Shallow, Non-Precipitating Convection (Betts, 1973)

Evaluating term B:

$$-\frac{\partial[\bar{\rho}c_p\overline{w'\theta'_1}]}{\partial z} = \frac{F_{b\theta_1} - F_{1\theta_1}}{3\Delta z} - \frac{F_{1\theta_1} - F_{2\theta_1}}{2\,\Delta z} \tag{67}$$

$$= -\frac{1}{\Delta z}[\int_{z_b}^{z_1}\frac{W}{3}\frac{\partial\tilde{\theta}_1}{\partial z}dz + \int_{z_1}^{z_t}\frac{W}{2}\frac{\partial\tilde{\theta}_2}{\partial z}]dz \tag{68}$$

where $F_{\theta 1}$ represents the fluxes of liquid water potential temperature (Betts, 1973).

Thus, the diabatic heating for a cloud layer can be represented linearly in terms of the W eigenvector and a modified base-state lapse rate in the cloud layer. In the example above:

$$\frac{\partial\tilde{\theta}_1}{\partial z} = \frac{\bar{\Gamma}}{1.5}\; ;\; \frac{\partial\tilde{\theta}_2}{\partial z} = 1.5\bar{\Gamma}\quad\text{where }\bar{\Gamma}$$

is the base state lapse rate. The lower layer lapse rate is generally less stable than the upper lapse rate.

It is well known that surface latent and sensible heat fluxes are an important source of moist static energy for the tropical atmosphere (Ooyama, 1969, Koss, 1976 ; Emmanuel, 1988). Normally their inclusion in numerical models is in the form of a bulk parameterization scheme which relates the moisture or heat flux to magnitudes of a surface or near -surface wind speed through a transfer coefficient. Because the eigenvalue problem requires that the equations remain homogeneous

with respect to the eigenvectors in the complex matrices, the surface fluxes can only be closed in terms of W, Θ, or Z. A method suggested by Haltiner (1967) and adopted here is to relate the surface perturbation flux to the temperature perturbation at a higher level in the model.

Following Haltiner's approach, the following procedure was used. (Actually, Haltiner, having only five layers in his model, extrapolated the temperature perturbation from the 750 mb level to the surface). First, the surface temperature perturbation was assumed to be equivalent to the temperature perturbation in the lower layers of the cloud:

$$\theta_o = \frac{\theta_1 + \theta_3}{2} = \theta_s - \theta_a \tag{69}$$

where θ_1 and θ_3 are the temperature perturbation at the first and third model levels in the cloud. The form of the surface heat flux using the bulk aerodynamic formula is:

$$Q_o = - \rho_o C_d c_p |V_s| [\frac{\theta_1 + \theta_3}{2}] \tag{70}$$

where C_d is the transfer coefficient and V_s is the surface base state wind speed.

Next, following Haltiner (1967) and Doos (1962), the surface heat flux is distributed vertically through the model using a pressure- weighted distribution of the form:

$$Q_n = \rho_o C_d c_p |V_s| \left[\frac{\theta_1 + \theta_3}{2} \right] \left(\frac{p_n}{p_s} \right)^r \qquad (71)$$

where n represents the linear model level, r is some integer, and p_s is the base state surface pressure. For the cases studied, r=2 and $C_d = 2.6e-03$ were used. (Haltiner, 1971). Initial tests of this scheme showed little influence for deep convection but not insignificant results for the shallow, non-precipitating convection. Therefore, the inclusion of surface fluxes was only placed in the shallow convection model.

Ooyama (1969) combines the processes of latent and sensible heat air-sea exchange into a single expression:

$$C_e V_s (\theta_e - \theta_{eo})$$

which is essentially a measure of the moist static energy differential between the sea surface and the overlying boundary layer. By expanding Ooyama's expression into mean and perturbed components and retaining only the perturbed contribution, the moist static energy flux then can be computed by multiplying (71) by

$$\exp \left[\frac{L(q_s)}{c_p T_s} \right]$$

where q_s is the saturation specific humidity of the sea surface temperature. Normally this factor is about 1.2.

V. Numerical Procedures

Having derived the necessary analytic forms to determine the linear system, a solution must be obtained. Previous research has shown that since the solutions are somewhat sensitive to the vertical resolution or number of levels in the model, the most robust solutions are obtained by using continuous functions in the vertical (Wang, 1987). While this approach may be suitable for purely theoretical studies, it is more difficult to adopt the continuous vertical functions where base states using observed data and more realistic closure schemes are required. A common approach is to discretize the vertical, i.e. divide it into numerous levels, write equations for each level and use finite difference forms for vertical derivatives. The system is then solved using an iterative numerical scheme. Asai (1970) found that at least 16 layers were required to produce a convergent solution using an iterative technique. Other total divisions used by researchers include 7 (Koss, 1976), 20 (Sun, 1978), 10 (Stark, 1976), and 20 (Eymard, 1985). In this study, a 21 level scheme for the vertical has been chosen. Second order centered finite differences for the vertical differences are used. For example:

$$\frac{dW}{dz} = \frac{W_{j+1} - W_{j-1}}{2h}$$

$$\frac{d^2W}{dz^2} = \frac{W_{j+1} - 2W_j + W_{j-1}}{h^2}$$

$$\frac{d^4W}{dz^4} = \frac{W_{j+2} - 4W_{j+1} + 6W_j - 4W_{j-1} + W_{j-2}}{h^4}$$

where W_j represents the non-dimensional vertical velocity defined at some level j and h is the non-dimensional spacing between levels:

h = Δ z/H = 1/N; N= number of layers in the vertical.

Substituting the above approximations into (11)-(15) of Chapter IV and grouping terms yields the following expressions:

$$W_{j-2}N^4 + W_{j-1}\{-4N^4 - k^2N^2 - K^2N^2\frac{R_z}{R_h} - N^2R_z \cdot \tag{1}$$

$$[\sigma + i(k_x\bar{U}_j + k_y\bar{V}_j)]\} - \frac{N}{2R_o}Z_{j-1} +$$

$$W_j\{6N^4 + 2N^2k^2 + \frac{R_z}{R_h}k^2(2N^2 + k^2) +$$

$$R_z(2N^2 + k^2)(\sigma + i(k_x\bar{U}_j + k_y\bar{V}_j)) +$$

$$iR_z(k_x\frac{d^2\bar{U}_j}{dz^2} + k_y\frac{d^2\bar{V}_j}{dz^2})\} + \frac{ik_yZ_j}{R_o^*}$$

$$+ W_{j+1}\{-4N^4 - k^2N^2 - k^2N^2\frac{R_z}{R_h} - N^2R_z[\sigma + i(k_x\bar{U}_j + k_y\bar{V}_j)]\}$$

$$+ \frac{N}{2R_o}Z_{j+1} + W_{j+2}N^4 - R_z R_i k^2 \Theta_j = 0$$

$$\Theta_{j+1}^{\cdot}(-\frac{N^2}{R_z P_z}) + \Theta_j\{\sigma + i(k_x \bar{U}_j + k_y \bar{V}_j) + \frac{2N^2}{R_z P_z} + \frac{k^2}{R_h P_h}\} \qquad (2)$$

$$- \Theta_{j-1}(\frac{N^2}{R_z P_z}) + W_j\frac{d\bar{\Theta}_j}{dz} = f^*_j(z)f(\Sigma a_i W)$$

where $f^*_j = f_j(z)\bar{\Theta}/\bar{T}$ is the vertical distribution function and $f(\Sigma a_i W)$ represents some form of moisture accession which is closed by the transform variable W.

$$Z_{j-1}(-\frac{\nu_z}{\nu_h})N^2 + Z_j\{R_h(\sigma + i(k_x \bar{U}_j + k_y \bar{V}_j)) + k^2 + 2\frac{\nu_z}{\nu_h}N^2\} + \qquad (3)$$

$$i R_h[k_x\frac{d\bar{V}_j}{dz} - k_y(\frac{d\bar{U}_j}{dz} + \frac{1}{R_o^*})]W_j$$

$$- N\frac{R_h}{2R_o}(W_{j+1} - W_{j-1}) - \frac{\nu_z}{\nu_h}N^2 Z_{j+1} = 0$$

The diagnostic equations can be written in similar form. For example,

$$U_j = i(k_y Z_j + k_x[\frac{W_{j+1} - W_{j-1}}{2h}])/k^2 \qquad (4)$$

$$V_j = -i(k_x Z_j - k_y[\frac{W_{j+1} - W_{j-1}}{2h}])/k^2 \qquad (5)$$

$$\nabla \cdot \bar{V}_j = ik_x U_j + ik_y V_j \qquad (6)$$

$$X_j = [ik_y W_j - (V_{j+1} - V_{j-1})\frac{N}{2}] \tag{7}$$

$$[P_{j+1} - 2P_j + P_{j-1}]N^2 - k^2 P_j = \tag{8}$$

$$[\rho_{oo}\frac{U_T^2}{P_{oo}}]\{-2i[k_x W_j \frac{d\bar{U}_j}{dz} + k_y W_j \frac{d\bar{V}_j}{dz}] +$$

$$R_i[\frac{\theta_{j+1} - \theta_{j-1}}{2}]N + \frac{Z_j}{R_o} + \frac{1}{R_o^*}[\frac{d\bar{U}_j}{dz} + \frac{(U_{j+1} - U_{j-1})}{2}N - ik_x W_j] +$$

$$[\frac{R_h - R_z}{R_z R_h}][\frac{W_{j+2} - 2W_{j+1} + 2W_{j-1} - W_{j-2}}{2}]N^3\}$$

The eddy correlation terms are written in a similar manner.

Equations (1) - (8) represent the basic numerical forms required for obtaining a solution.

a. Forming the Eigenvalue Problem

Fig. 5.1 displays the 21 level model. The three equations for W, θ, and Z are used in the model where free boundary conditions are applied:

$$\frac{d^2 W}{dz^2} , \quad W = 0 \text{ at top } \partial \quad \text{ bottom}$$

$$\theta = 0 \quad \text{ at top and bottom}$$

$$\frac{dZ}{dz} = 0 \text{ at top and bottom}$$

or in numerical form

$$\frac{d^2W}{dz^2} = \frac{dZ}{dz} = 0$$

Z   z=16 km

W,Θ,Z

h=Δz/H=0.05

Δz=0.8 km

W, Θ, Z   BASE

Z   z=0 km

$$\frac{d^2W}{dz^2} = \frac{dZ}{dz} = 0$$
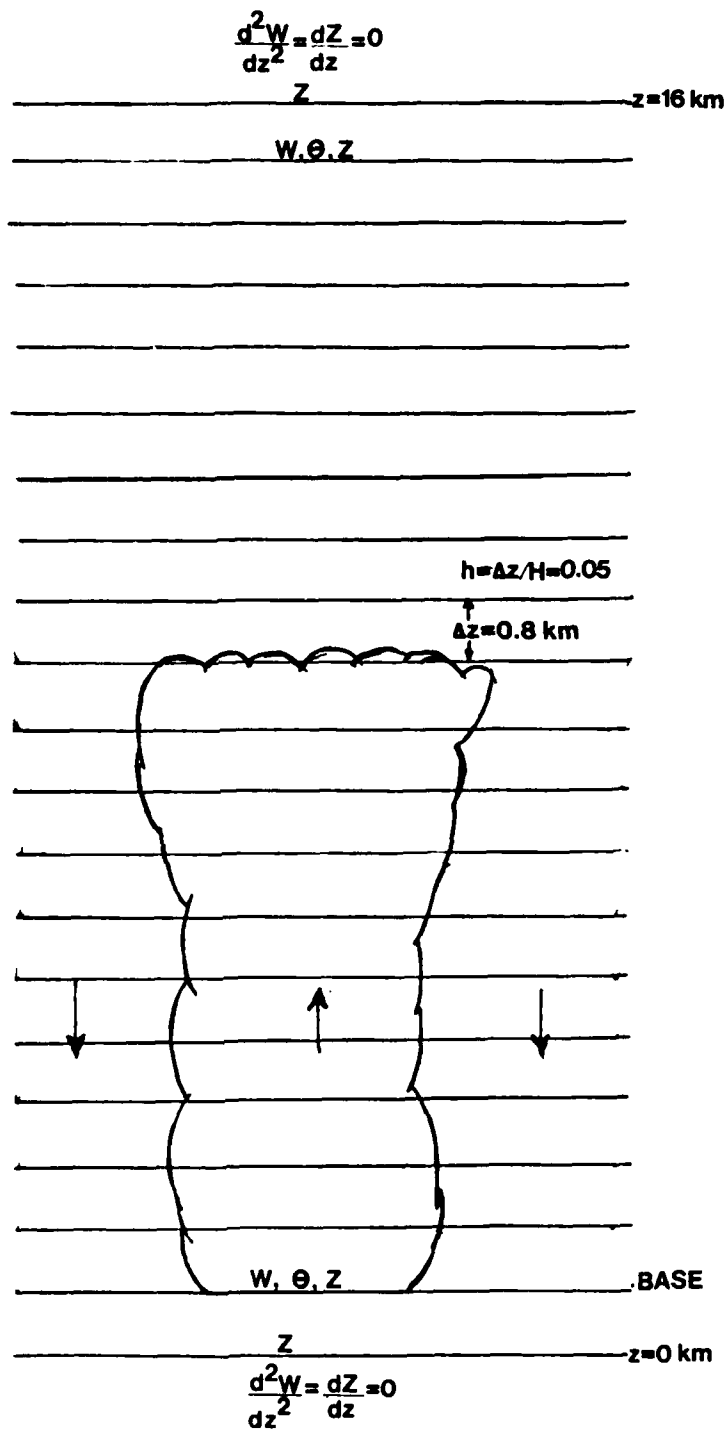
21 LEVEL MODEL

Fig. 5.1. 21 Level Convection Model

$$W_0 = W_{20} = 0$$

$$W_1 = -W_{-1}$$

$$W_{N+1} = -W_{N-1} \qquad (N=20)$$

$$\Theta_0 = \Theta_n = 0$$

$$Z_1 = Z_{-1}$$

$$Z_{N+1} = Z_{N-1}$$

Rigid boundary conditions were also tested for the lower boundary (Chandrasekhar, 1961):

$$\Theta = W = U = V = Z = 0 \qquad\qquad (9)$$

$$\frac{dW}{dz} = 0$$

Little difference was noted in the results when compared with the free boundary conditions. Thus, free boundary conditions were used for convenience throughout this study.

Using free boundary conditions, the numerical equations for W, Θ, and Z are written for levels 1 - 19 and the equation for Z is also written for levels 0 and 20. This procedure yields 59 algebraic equations for 59 unknown perturbation or transform variables and 59 eigenvalues represented by the complex frequency σ.

The algebraic equations are written in the form:

$$A\bar{x} - \sigma B\bar{x} = 0 \qquad (10)$$

where σ is the eigenvalue which is complex, x is the eigenvector containing the complex perturbation transforms, and A and B are the sparse complex "operator" matrices containing the constant coefficients in equations (1) - (3). 0 is the null columnar matrix. Besides revealing a sparsity (~90% zeroes) which is consistent with a matrix associated with a grid, both the A and B matrices are in banded form and quasi-symmetric with the exception of the latent heat square sub-matrix and surface flux columns (Fig. 5.2).

The solution method for the perturbation pressure whose governing equation (Poisson's equation) was derived in the previous chapter is also a boundary value problem. The form is $A\bar{x}=b$ where A is a tridiagonal 21 x 21 matrix formed as a result of the Laplace operator, $\bar{x}$ is the perturbation pressure eigenvector and b represents the right-hand side. The algorithm for solution is a simple but robust Gaussian elimination technique which requires relatively few lines of code and is documented in standard numerical texts.

All vertical derivatives, unless otherwise noted, are approximated by second order centered finite differences. Numerical integrations are accomplished using the trapezoidal scheme which is also of second order accuracy.

b. The LZ/QZ Algorithms
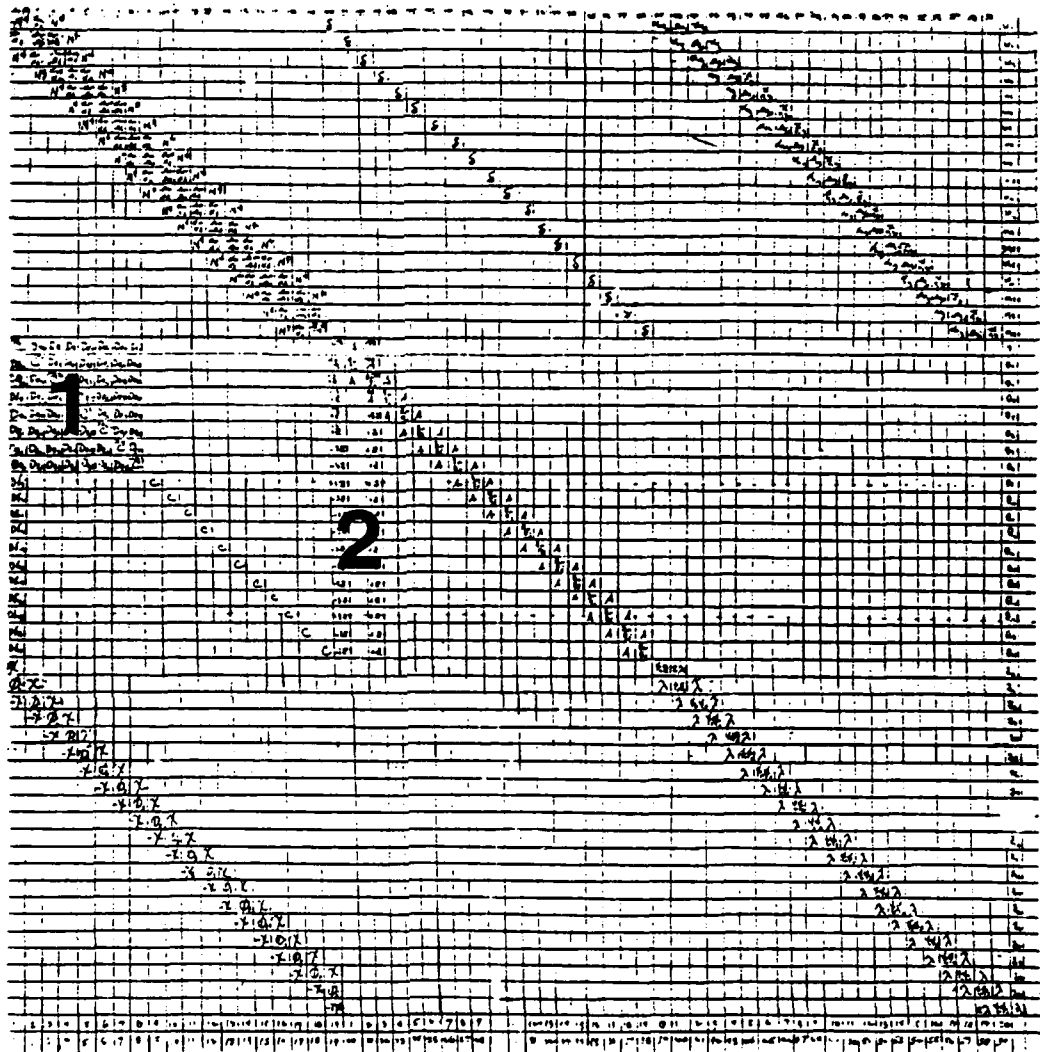
COMPLEX MATRIX 'A'

1: LATENT HEATING (CLOUD)

2: SENSIBLE HEATING

Fig. 5.2 Linear Operator Matrix "A"

81

In large systems of simultaneous equations, especially in ill- conditioned systems, round-off error can destroy the accuracy of the solution since it is propagated all along the solution. Thus, routines which involve a matrix inversion, an often unstable process, should be avoided. Instead, an iterative method should be sought provided it converges (Stark, 1970).

The set of equations of the form $A\bar{x}-\sigma B\bar{x}=0$ represents the complex generalized eigenvalue problem. Two algorithms exist which solve the problem using the iterative technique. One is the LZ algorithm (Kaufman, 1975) which uses elementary transformations and complex operands. The other is the QZ algorithm (Garbow, 1978) which employs unitary transformations using programmed complex arithmetic on real operands. The practical difference in using the two algorithms is the LZ algorithm requires specification of two input N x N complex matrices respectively for A and B and one N x N complex matrix for the computed eigenvector output while the QZ algorithm requires specification of four input real N x N matrices and two output N x N matrices for the eigenvectors. In practice, on the SLUATMOS Masscomp, the QZ algorithm requires about twice as much computing time as does the LZ algorithm. Because of the increased core and computing time requirements of the QZ algorithm, the LZ algorithm was used throughout the study for solutions to the linear system.

The LZ algorithm reduces the complex matrix A to upper

Hessenberg form (one diagonal filled below the center diagonal) and the complex matrix B to upper triangular form. Then the A matrix is iteratively reduced to upper triangular form while preserving the triangularity of B using stabilized elementary transformations. These transformations are designed to minimize the loss of accuracy in numerical operations.

Next, using the two upper triangular matrices A and B formed above, the ith eigenvalue will be found on their diagonals , i.e. $a_{ii}(k)/b_{ii}(k)$ if $b_{ii}(k)$ is non-zero. The corresponding eigenvector x_i is found by solving:

$$(b_{ii}(k)A_k - a_{ii}(k)B_k)^*y_i = 0 \tag{11}$$

and setting $x_i = M^*y$ where M is a matrix computed during the iterative procedure. The eigenvectors are normalized so that the modulus of their largest component is 1.

Assuming no singularities in the input matrices, the LZ algorithm will converge to a solution in about 3n iterations where n is the order of the matrix. For a single eigenvalue/eigenvector pair, the number of iterations for convergence ranges from 0 to 8 for a 59 x 59 operational pair of matrices.

The numerical accuracy of the results is a matter of concern when solving large complex matrices. To determine an estimate of the error, a relative residual estimation has been used. Besides evaluating the results for appropriate physical

behavior, a measure of numerical performance for the generalized complex eigenvalue problem as defined by EISPACK (Garbow, et al.,1977) is:

$$\tau = \frac{||b_i Ax_i - a_i Bx_i||}{10 \cdot N \cdot eps(|b_i| \cdot ||A|| + |a_i| \cdot ||B||) \cdot || x_i ||} \qquad (12)$$

where N is the matrices' order

A and B are the input complex matrices

a ,b are the eigenvalue terms

x is the eigenvector

eps is the machine precision

Also, $|$ represents magnitude and $||$ is the symbol for a matrix norm. 1-norms (the largest matrix columnar magnitude) are used for the SLUATMOS performance estimates. The term eps may also be treated as a desired precision or tolerance; i.e. how many digits of accuracy are desired for the performance estimate? In the matrix computations here, eps has been set to $10^{**}-5$.

The performance index is essentially a measure of the size of the relative residual --i.e., the matrix residual divided by the matrix norm. These residuals are sensitive to small perturbations in the eigenvalues. For all matrix computations, performance indices are computed and evaluated for each eigenvalue/eigenvector pair for the LZ algorithm. According to EISPACK thresholds (Garbow, 1977), if $\tau < 1$, the numerical results are considered excellent. If $1 < \tau < 100$, the results

are considered good. If $\tau > 100$, the results are considered poor numerically. Using 64 bit machine precision, the results are excellent or good for all grid points during the linear model production runs at NCAR on Cray C1/CX. $\tau < 1$ for about half of all computations.

A brief comparison of LZ and QZ algorithm output reveals almost identical results. Treating the QZ algorithm computations as the "true" result and varying the diabatic heating (precipitation efficiency) over a range of P=0.8 to P=1.8 ,the LZ algorithm possessed a relative error of about $1 \times 10^{**-8}$ % for the eigenvalue computations (both real and imaginary part) and about $1 \times 10^{**-10}$ % for the integrated eigenfunction moduli. For the real part of the eigenfunction correlation terms (integrated over the entire depth), a relative error of 1.45% was computed. In addition, a visual comparison was performed of the plotted eigenfunction vertical cross-sectional results between the two algorithms. Identical moduli (amplitudes) and phase differences between eigenfunctions existed for both algorithms. Correlation plots matched exactly. The diagnostic pressure perturbation computations were identical below 10 km but showed differences in amplitude and phase above that level. The trend was however the same. The perturbation pressure eigenfunction was the only output to show noticeable differences between the two methods. This suggests there may be some ill-conditioning associated with the tridiagonal matrix technique.

c. Machine Precision and Compatibility

To reduce the propagation of round-off error, all computa-
tions were performed using 64 bit word-lengths including the
linear model, its attendant subroutines, and all cloud model
computations. This is equivalent to double precision on the
Masscomp and single precision on the Cray computers (Cray dou-
ble precision is 96 bit but does not allow for complex
numbers). Early in this research, it was found that single
precision computations led to program aborts during the matrix
calculation. Also, the matrix performance index occasionally
exceeded tolerance limits. The use of 64-bit length words
solved both of these problems. However, it added ~20% more
time to the matrix calculations.

To compute the dominant modes for one wavenumber grid
point in double precision requires ~8-10 minutes of CPU time
for SLUATMOS. To fully define a wavenumber domain requires
about 100 grid points. The tremendous computing time require-
ments of SLUATMOS can be circumvented by running these jobs on
the fast (but expensive) Cray C1/CX of NCAR. Computing times
are reduced by a factor of 500.

The primary code modifications necessary for Cray comput-
ing are (1) the change of all double precision complex vari-
ables to single precision complex and (2) development of the
appropriate Job Control Language to handle data and file
transfer between the Cray, the IBM 4381 "front- end", the Mass

Storage System, and the different output devices. 10 GAU were allocated for the project (1 GAU is approximately equal to one hour of CPU time). For a 160 point k wavenumber domain run, about 80 sec of Cray C1 CPU time and 57 sec of Cray CX CPU time are required. All the GAU were used. Results were compared with Masscomp calculations for each Cray implementation. The only discrepancy noted was a slight difference in the vertically-integrated higher order Legendre polynomial fits. The subroutine used to compute the polynomial employs a matrix inversion technique which is sensitive to round-off error for higher order polynomials. Even though both machine computations used 64 bit words, it is possible the different methods of computing intrinsic functions on the Cray and Masscomp resulted in the discrepancy which was magnified by the ill-conditioning. The net result was changes occurred in the third decimal place of the computed growth rate. However, no significant changes were noted in the pattern of the wavenumber domain. It was decided that the discrepancy posed no obstacle to obtaining compatible results between the two machines.

d. Selecting the Eigenvalue-Eigenvector Pairs and Displaying the Results

The procedures adopted for selecting the eigenvalue-eigenvector pair are straightforward. The eigenvalue with the largest real part (and its corresponding eigenvector 59 x 1 columnar matrix) are plucked from the 59 candidates for a given wavenumber and orientation angle and checked for numerical

performance. Any other necessary diagnostic computations are made for this point using the selected eigenvalue- eigenvector pair.

For production runs at NCAR, the model was run for a 160 point rectangular grid in the wavenumber domain. With a 1 wavenumber grid interval, the grid limits for the 16 km scale height ranged from -7.5 to 7.5 in the k_x direction and 0.25 to 9.25 in the k_y direction. For the 3 km scale height, the ranges were 0.25 to 4.75 and -3.75 to +3.75 in the k_y and k_x directions, respectively. The wavenumber k and angular locations are, respectively:

$$k = (k_x^2 + k_y^2)^{**0.5} \tag{13}$$

$$\varepsilon = atan2(k_y, k_x) \tag{14}$$

The orientation angle of the base state shear vector in the k domain is:

$$shreps = atan2(vshr, ushsr)*180/\pi \tag{15}$$

The shear magnitude is simply:

$$shrmag = \{[ushr^{**2} + vshr^{**2}]^{**0.5}\}U_T \tag{16}$$

where vshr, ushr are the non-dimensional $\overline{U}, \overline{V}$ least squares fitted shear components for the cloud depth. Three "if" statements are used to determine the appropriate orientation angle quadrant.

.

For each eigenvalue, there will be an eigenvector containing 59 complex transform coefficients --19 coefficients each for W and θ (19 levels) and 21 coefficients for Z (21 levels including surface and top). The transform's magnitude or modulus is, for example:

$$|W| = [(W_r)^{**2} + (W_i)^{**2}]^{**0.5} \tag{17}$$

where W_r and W_i represent the real and imaginary coefficients respectively, of the complex transform.

Its phase angle in the complex domain is:

$$\phi = atan2(W_r, W_i) \tag{18}$$

Thus:

$$W = |W| exp(i\phi) \tag{19}$$

Using (14), (17), the horizontal wavenumber and normal mode assumptions from Chapter 4, and dropping the imaginary term yields:

$$w^* = |W| \cdot [cos\phi + \frac{2\pi}{1_x} Lcos\epsilon + \frac{2\pi}{1_y} Lsin\epsilon] \tag{20}$$

where 1_x and 1_y are the dominant mode horizontal wavelengths in the k_x and k_y directions, respectively, and L is the horizontal distance in the k direction whose unit length is the wavelength of the dominant mode or 2π radians in the phase

angle domain.

For plotting purposes, one wavelength is divided into 16 intervals or 25 grid points per 3π radians (1.5 wavelengths). Including all 21 vertical levels, this results in a 21 x 25 rectangular mesh for which the vertical cross-section is plotted. Horizontal periodicity appears in the solutions due to the integral transformation.

e. Bugs

With any programming job, a major concern is undetected coding errors. Normally major errors affect the results enough to be detected readily. However, minor errors may slip through.

During the runs at NCAR, the growth rates and eigenfunction results were carefully checked against standard runs performed on the Masscomp. No discrepancies were noted except for the aforementioned least squares matrix ill-conditioning and the upper part of the perturbation pressure pattern for the western Arabian Sea. The latter discrepancy was mistakenly attributed to the least-squares problem. However, the source of the discrepancy was the bulk Richardson number formula, which is used explicitly by the perturbation pressure subroutine, was deleted during code splicing at NCAR. This deletion did not affect the eigenvalues or other eigenfunctions since the Richardson number is not used explicitly in other terms. Affected plots were re-run.

A second bug was found in the lDSS cloud model freezing subroutine. The saturation vapor pressure over ice formulation used in Ogura and Takahashi (Chapter IV, eqn. 52) was miscoded. The net effect of the miscoding was the upper heating distribution was reduced somewhat compared to the correct formulation although the upper level heating was still increased over its non-freezing value. However, this error was not significant enough to alter the cloud model height in any of the examined cases and did not significantly affect the growth rate magnitudes or patterns in the wavenumber domain. This coding error was caught due to the extraordinary sensitivity of the time dependent model to the ice saturation specification. In the lDTD model, the Pruppacher-Klett (1978) numerical formulation is used. Even though their formulation is more lengthy, it gives essentially the same results as the Ogura and Takahashi formula. Neither formula is usable below -50C.

A third bug was found in the eddy viscosity estimation where the total number of levels used to determine the mean cloud depth viscosity was not enclosed in parentheses. This error resulted in a slight reduction in viscosity --about 1-3 m**2/s for small cores and about 3-10 m**2/sec for 1500m cores or greater. This error in the estimate should have no effect on the character of the results.

f. The Computer Model Flow Chart

Having laid the physical, mathematical, and numerical

premises for the model, it is now coded and divided into func-
tional modules which are linked in a flexible manner. Fig. 5.3
represents the flow chart of the basic linear model. The indi-
vidual modules are described briefly below:

Linear Transform Driver (LTD): This is the heart of the model.
It receives the base state initialization from both the HEAT
and WIND modules.   It computes the transform coefficients,
places them in the derived matrix forms, sends and receives
data from the LZ algorithm and computes the diagnostic
transform quantities as required. Different versions compute
these quantities for an entire k grid or for an individual mode
including eigenfunction cross-sections and eddy flux profiles.
The LTD is distinguished by how moisture or heat is accessed
into the linear model --cloud depth, BL, or shallow non-
precipitating. Also, certain scaling parameters such as scale
height and latitude are set in the LTD itself.

LZ Algorithm (LZ): The essential numerical aspects of the LZ
algorithm have been described previously in this chapter. The
algorithm is divided into three subroutines:

  --LZHES: Reduces the complex matrix A to upper Hessenberg
form and reduces the complex matrix B to upper triangular form.

  --LZIT: Solves the generalized eigenvalue problem using the
reduced matrices from LZHES.

  --LZPI: Computes the performance index for each eigenvector-
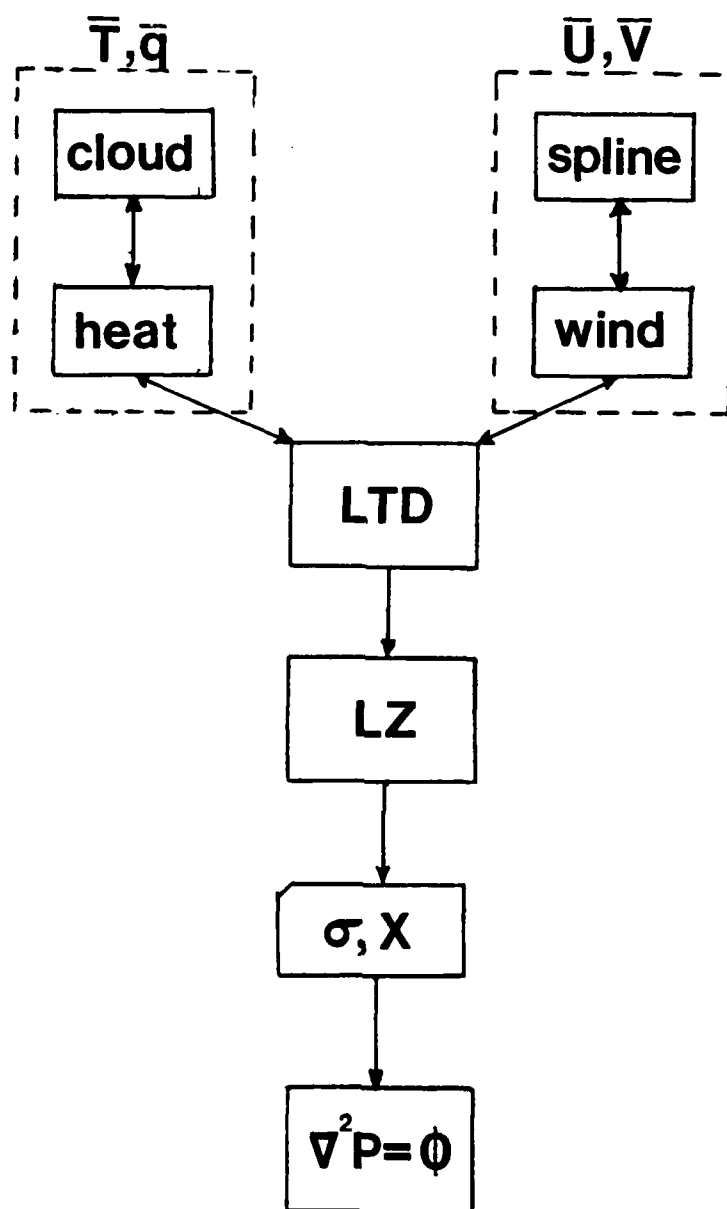
A LINEAR CONVECTION MODEL

Fig. 5.3 Computer Flow Chart for the Linear Model

eigenvalue pair produced by LZIT.

All three subroutines are called from LTD.

HEAT Algorithm: HEAT contains the thermodynamic base state from which it computes the convective heating and/or sensible heating vertical profile using the Anthes cumulus parameterization scheme and the 1DSS cloud model or Betts parameterization. Modified versions also incorporate the Kuo-Raymond sensible heat transport equations. In addition, HEAT provides estimates of eddy diffusion coefficients averaged over the cloud depth. HEAT requires specification of a cloud core radius.

WIND Algorithm: WIND contains the base state wind from which it computes the first and second vertical derivatives of the u and v components after fitting the data with a least-squares Legendre polynomial. WIND requires specification of the polynomial order which may range from 1 - 9.

Perturbation Pressure Algorithm (PP): The perturbation pressure eigenfunction is computed as a separate boundary value problem using previously computed base states and transform quantities. Its derivation is found in Chapter IV.

VI. Determination of the Base States

a. Description

In the linear model discussed in the previous chapters,
the temperature, wind, and moisture profiles of the base state
are assumed to have no horizontal variation over the domain
under consideration.   This is implicit in the open lateral
boundary conditions. Thus, it becomes necessary to determine a
sounding representative of the convective conditions under
investigation.

The base states used here are taken from data gathered
during June 1979 over the Arabian Sea during the Summer Monsoon
Experiment. Data sources available during this period have
been discussed previously in studies by Grossman and Durran
(1984), Meyer and Rao (1985), Roadcap and Rao (1986), Benson
and Rao (1987), and others. Sounding data includes a mix of
observation platforms such as the NCAR Electra, NOAA P-3,
island and ship-based rawinsonde, and dropwindsondes. Probably
the most thorough composite of dropwindsonde data over the
eastern Arabian Sea has been accomplished by Grossman and Dur-
ran (1984). Using the extensive coverage by U.S. aircraft dur-
ing SMONEX, they determined average thermodynamic profiles for
days with and without convection from the surface to 300 mb.
In order to best simulate conditions uncontaminated by upstream
convection, they confined their analysis to locations between

95

67E and 71E and north of 15N. The stratified data were inter-
polated to 50 mb intervals and each class was averaged to give
a "convective" sounding and a "non-convective" sounding. An
E-W basic state flow (no v component) with a low-level maximum
(after Ogura and Yoshizaki, 1988) was used as the standard wind
distribution associated with these two base states for the
linear model runs.

Ideally, composite soundings stratified according to con-
vective activity represent the best approach for studying the
linear model response. By averaging many soundings, "noise"
due to instrumental error and transient convection is filtered
and a more representative signal emerges. However, the lack of
sounding data over tropical oceans often makes it necessary to
rely on individual soundings in order to investigate a particu-
lar convective episode (e.g., Dudhia and Moncrieff, 1987).
Thus, I have used four more base states based on either a sin-
gle sounding or aircraft run or on a sounding and a nearby
coincident dropsonde profile.

A third base state is formed from sounding data taken near
the convective bands studied by Benson and Rao (1987). The
thermodynamic and wind profiles below 550 mb are taken from the
20 June 0542 CUT dropwindsonde (12.3N 71.3E) launched from the
NCAR Electra. Above 550 mb, the closest in space and time
available sounding (Amini, 10.5N 73E, 19 June 18 UTC) was used.
This base state was assumed to be representative of the
environment of the deep moist Eastern Arabian Sea convection on

that day. A fourth base state representing conditions for deep convection associated with the Monsoon Onset was derived from the USSR ship Volna sounding (9.2N 66.7E) on 12 June 1200 UTC.

As noted earlier, the central and western Arabian Sea environment is more stable, dry, and less disturbed than the eastern Arabian Sea. The sounding used as representative of the central Arabian Sea base state is ship Deepak (15N 65E) on 24 June 0608 UTC. For the western Arabian Sea, no ground- or ship-based rawinsonde are available from the immediate vicinity. However, the NOAA P-3 performed "saw-tooth" patterns in the cloud- and sub-cloud layer on 24 June east of Socotra Island from 0730 to 1000 UTC. The purpose of these maneuvers was to investigate the Somali Jet structure. From the aircraft soundings, LaSeur (1981) prepared a cross-section of wind, temperature, and humidity from the surface to about 3 km. Estimates of cloud base and cloud height were determined from on-board movie camera film during descent and ascent. These were used to prepare a base state representative of the W. Arabian Sea at 13N 57E.

b. Data Preparation

The six base states were prepared for model use in the following manner. The observed temperature, humidity (dewpoint), and pressure data were used to compute the corresponding height levels using the hypsometric formula. Next, the height, temperature, and moisture values were inter-

polated to the linear model height surfaces using a quadratic interpolating polynomial and then the corresponding pressure values were computed. The interpolated results were plotted on a Skew-T and examined visually. The temperature curve is adjusted by hand, if necessary, to eliminate adiabatic or superadiabatic lapse rates. The wind data is handled in a similar manner except that it is first broken into U and V components. The least-squares fitting procedure of the winds before their usage by the model is discussed in Chapter IV. For levels above the available data (if any) in the upper troposphere, temperature and dewpoint curves are inserted by hand. Normally, missing winds were replaced by those consistent with an easterly jet. For the western Arabian Sea, where the data were cut-off at 3000 m, the model scale height was reduced to 3 km with 150 m between levels. For the 1DSS cloud model, temperature and moisture profiles were linearly interpolated to the cloud model surfaces using the linear model profiles. For the cloud model only, the surface temperature was adjusted if necessary to produce a more neutral lapse rate in the subcloud layer to assist cloud initiation. This procedure had little effect on the final cloud depth or strength.

In addition to the sounding data, the 1DSS cloud model and condensational heating algorithm requires specification of an updraft or cloud tower radius for the lateral entrainment approximation. Normally these radii are determined photogrammetrically or through visual aircraft penetration. However,

these methods are often impractical and a measured vertical velocity threshold exceeded over a given distance has been used to define core size (e.g. LeMone and Zipser, 1980; Benson and Rao, 1987). Cotton (1986) notes that rarely is it possible to obtain representative sampling of a cloud system in a given case study. He suggests that the rms vertical velocity averaged over the width of a cloud is more useful for comparison with model results than is the mean vertical velocity.

Core measurements using NCAR Electra 1 second vertical velocity measurements (1 m/s threshold over 500 m or longer distance) and analyzed by Tamin (1988) show mean updraft radii of 475 m for the 20th of June over the Eastern Arabian Sea and 1650 m for the Central Arabian Sea (24 June 1979). However, the core measurements for the eastern Arabian Sea were made at or below 540m which is normally at or below cloud base. Simpson and Wiggert (1971) noted that even in the strongest hurricanes, core radii rarely exceeded 2000 m. Because of the uncertainty in determining representative core radii, the core radius was varied during the model runs for each base state. The specified radii were 500 m, 1000 m, and 1500 m for deep convection and 500 and 1000 m for less deep convection.

c. θ, θ_e and u,v Diagrams for the Base States

The following four diagrams (Figs. 6.1-4) show θ, θ_e, u, and v vertical distributions for the five deep convective base states. These are the profiles that were inserted into the

linear model code. Base state plots for the western Arabian Sea as well as convective heating profiles and discussion for the deep convective base states are included in Chapter VII.

d. Cloud Model Results

A data table for 1DSS cloud model runs (Table 6.1) for each base state follows. Table 6.2 displays computed values of the Kuo moistening parameter "b" for different cloud heights using the Anthes formula discussed in Chapter IV. Also, contour plots for the 1DTD vertical velocity computations plotted as a function of time and height are shown in figure 6.5. For the 1DTD model, total integration time is 2 hours and model depth is 15.8 km.
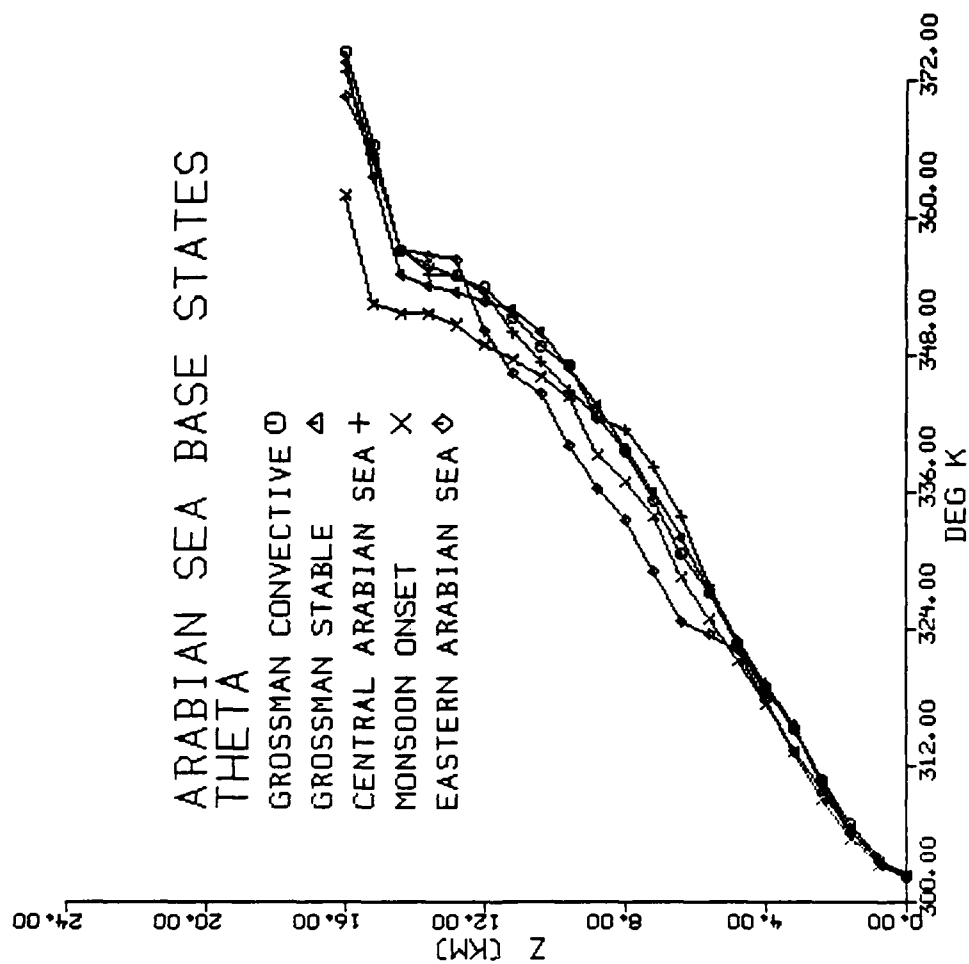
Fig. 6.1 θ Profiles for the Base States
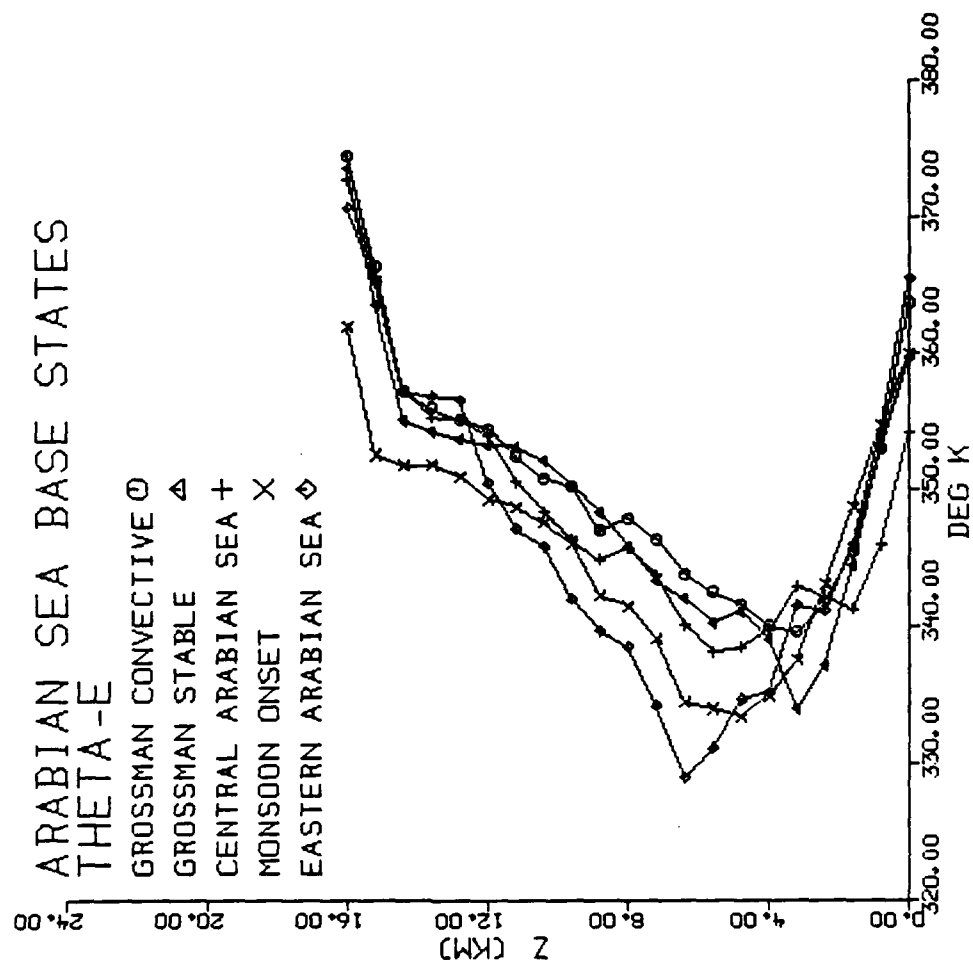
Fig. 6.2 θ_e Profiles for the Base States
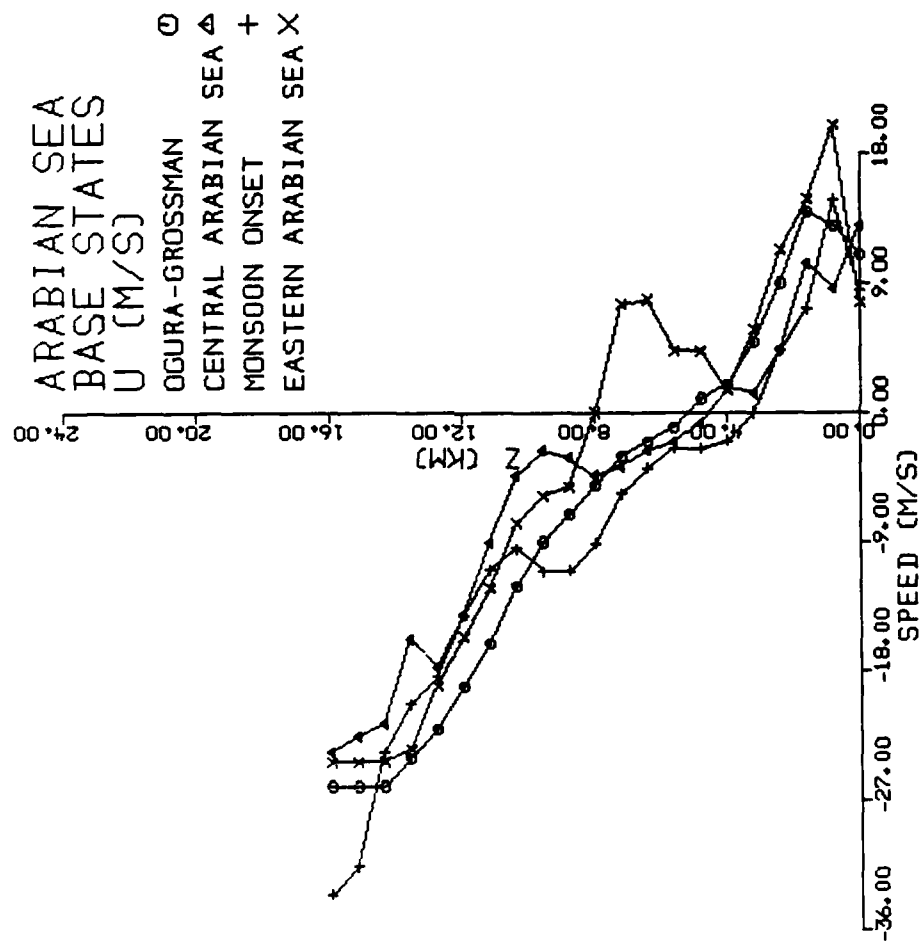
Fig. 6.3 U Profiles for the Base States
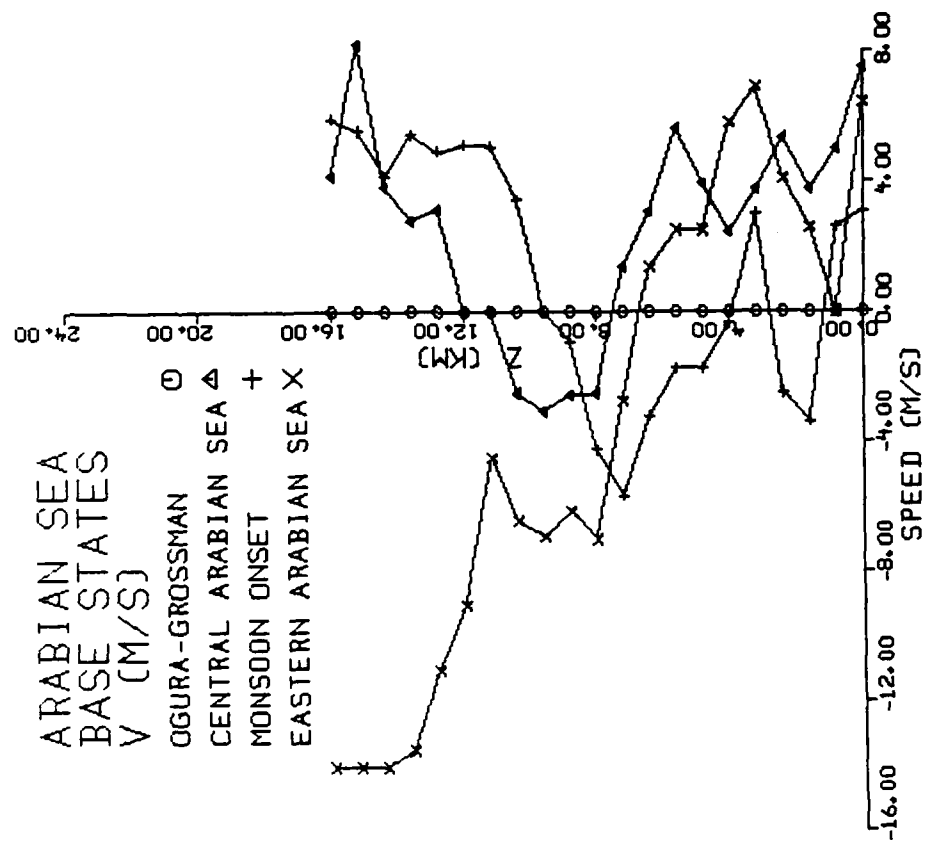
Fig. 6.4 V Profiles for the Base States

104

TABLE 6.1   1DSS CLOUD MODEL OUTPUT   (CONSTANT RADIUS)

20 June 1979 06UTC EASTERN ARABIAN SEA (Amini/Electra Dropsonde)

core	top	ptop	wmax	nuz	rate	time	z(wmax)
500	7850	386	8.7	14.6	10.0	24.0	2750
1000	10450	270	17.0	40.9	15.1	20.3	7100
1500	11550	230	21.4	78.3	15.3	19.3	7500
2000	12100	212	24.2	123.5	14.2	18.3	7750

24 June 1979 06UTC CENTRAL ARABIAN SEA (Deepak 15N 65E)

core	top	ptop	wmax	nuz	rate	time	z(wmax)
500	2800	727	3.8	17.1	3.4	19.0	1950
1000	5950	494	5.6	41.6	8.5	28.0	2400
1500	6350	470	6.5	66.8	10.4	24.7	2500
2000	6400	467	7.0	91.4	10.4	23.1	2600

12 June 1979 12UTC MONSOON ONSET (Ship Volna 9N 67E)

core	top	ptop	wmax	nuz	rate	time	z(wmax)
500	6250	474	9.0	14.9	9.3	22.4	2900
1000	9200	321	12.9	37.3	11.8	26.6	3950
1500	9800	296	15.6	70.3	14.7	19.5	5500
2000	10300	276	17.6	112.6	14.4	20.3	6200

June 1979 GROSSMAN CONVECTIVE COMPOSITE

core	top	ptop	wmax	nuz	rate	time	z(wmax)
500	5400	530	6.7	12.2	7.7	23.6	2200
1000	9200	324	9.8	26.7	12.5	27.6	3000
1500	11800	225	12.4	55.1	11.6	34.8	5050
2000	12250	210	14.0	79.4	12.9	32.0	5200

June 1979 GROSSMAN STABLE COMPOSITE

core	top	ptop	wmax	nuz	rate	time	z(wmax)
500	4300	607	6.1	18.1	4.3	33.3	2100
1000	6750	447	8.6	33.2	11.8	23.8	2700
1500	9300	319	10.0	50.5	10.0	40.9	4400

```
2000    10600    267       11.5      80.2      11.6      38.9      4650
```

core= radius (meters)

top= height (meters)

ptop= pressure cloud top (mb.)

wmax= max vertical velocity (m/s)

rate=rain rate (cm/hr)

time=development time (minutes) --time for parcel to traverse
cloud depth

z(wmax) = height of vertical velocity maximum (meters)

nuz=vertical eddy diffusion coefficient (m**2/s)

TABLE 6.2   KUO MOISTENING PARAMETER "b"

20 June 1979 06UTC EASTERN ARABIAN SEA   (Amini/Electra Dropsonde)

core	top	"b"	"b*"
500	7850	.10	.52
1000	10450	.09	.49
1500	11550	.09	.49

24 June 1979 06UTC CENTRAL ARABIAN SEA (Deepak 15N 65E)

core	top	"b"	"b*"
500	2800	.05	.39
1000	5950	.10	.52
1500	6350	.15	.61

12 June 1979 12UTC MONSOON ONSET (Ship VOLNA 9N 67E)

core	top	"b"	"b*"
500	6250	.09	.49
1000	9200	.14	.59
1500	9800	.14	.59

June 1979 GROSSMAN CONVECTIVE COMPOSITE

core	top	"b"	"b*"
500	5400	.06	.43
1000	9200	.04	.35
1500	11800	.04	.37

June 1979 GROSSMAN STABLE COMPOSITE

core	top	"b"	"b*"
500	4300	.12	.56
1000	6750	.13	.58
1500	9300	.13	.58

core = radius (meters)

top = height (meters)

"b" = moistening parameter (n=2.5, RHC=.35)

"b*" = moistening parameter (n=1.0, RHC=.50)

note: saturation mixing ratio computed with respect to ice
    for levels above 263K.
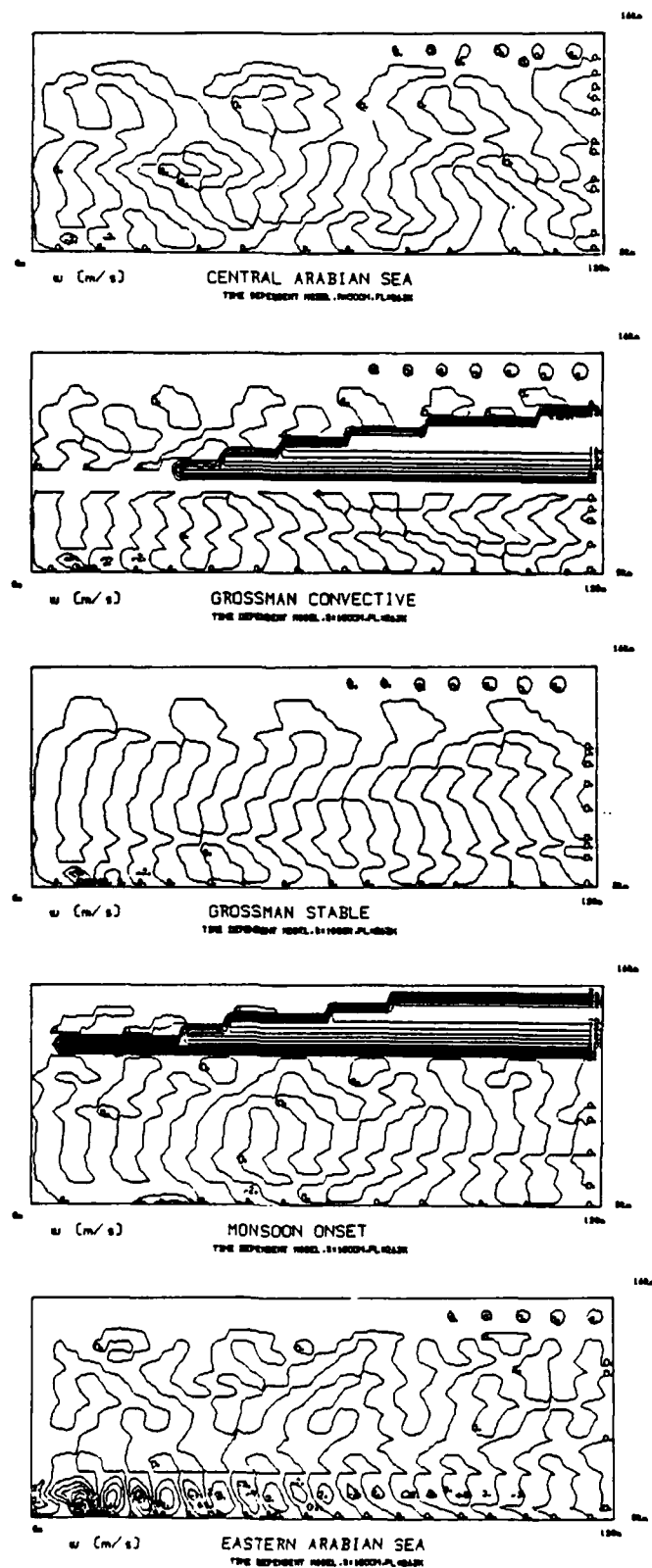
1-D TIME INTEGRATIONS

Fig. 6.5 1DTD Cloud Model Integrations for the Base States (2 hours)

VII. Results

a. Introduction

The linear model was run extensively for the six base states (w. Arabian Sea, c. Arabian Sea, e. Arabian Sea, monsoon onset, Grossman convective composite, and Grossman stable composite.) Scale height was 16 km for all base states except the W. Arabian Sea where the scale height was set to 3 km due to the lack of data above that level. Parameters that could be varied during the runs included the following:

(1) Vertical eddy diffusion

(2) order of wind polynomial fit

(3) cloud core radius (cloud height and lateral entrainment

(4) method of moisture accession into the model

(5) precipitation efficiency

(6) inclusion or non-inclusion of sensible heat transport in vertical heating profile

(7) inclusion or non-inclusion of surface fluxes (non-precipitating convection only)

For the analyzed base states, wavenumber (k) domain contour plots of growth rate, B, phase speed, and flux Richardson number are produced. Also a few contour analyses of vertically-integrated eigenfunctions were performed for

selected base states. All of these contour plots are produced using a 16 x 10 point grid and the NCAR plotting package (CON-RECSMTH). Eigenfunction contour plots for an individual base state use a 21 x 25 grid (z-L plane) where L is the horizontal wavelength in the k direction with 16 grid spaces per wavelength (2π radians).

Here, the term B is defined:

$$B = \left| \frac{\sigma_r}{\sigma_i + k_x U_m + k_y V_m} \right| \tag{1}$$

where σ_r (growth rate) and σ_i represent the real and imaginary parts of the eigenvalue, respectively, and U_m and V_m are the mean u and v non-dimensional wind components computed over the cloud depth using the Mean Value Theorem. Larger values of B, say greater than 5, may be considered to be associated with stationary modes relative to the mean wind.

The band phase speed relative to the fixed cartesian coordinate system is:

$$c = -\sigma_i/k \quad \text{(Asai, 1970)} \tag{2}$$

where σ_i is the complex portion of the eigenvalue. It may also be viewed as the oscillatory part of the frequency. Accounting for the component of the wind perpendicular to the band, the band phase speed relative to the cloud layer mean wind is:

$$c = \frac{-(\sigma_i + k_x U_m + k_y V_m)}{k} \tag{3}$$

(3) is plotted in the phase speed diagrams. Knowing σ_i at every grid point in the wavenumber domain, the group velocity may then be computed numerically for each point to measure the dispersion of the wave field.

The flux Richardson number was defined in a previous chapter. The mean value theorem was used to compute the mean eigenfunction quantities for the depth which were then plotted and contoured. For example,

$$\bar{X} = \int_a^b X \, dz/(b - a) \tag{4}$$

where X is the complex eigenvector.

Throughout the remainder of this study, the terms "longitudinal" and "transverse" will be used frequently. A "longitudinal" mode implies that a dominant mode (wavenumber associated with the largest growth rate) is parallel (within +/- 30 degrees) to the base state shear vector in the cloud in the k plane. Conversely, a "transverse" mode will be perpendicular (within +/-30 degrees) to the shear vector. The shear vector as described previously uses the prescribed least-squares fit.

b.   Western Arabian Sea (24 June 08UTC, 13N 57E)

The western Arabian Sea base state is characterized by a well- mixed subcloud layer below 1000 m and a convectively

unstable but statically stable layer above the cloud layer
(Fig. 7.1). Based on aircraft film, the cloud depth is ~ 200m
in the base state area (900 - 1100 m AGL). For the linear
model, clouds are introduced in the layer from 900-1200 m using
the Betts (1973) non-precipitating parameterization scheme.
The observed wind distribution shows a SW jet maximum at about
1 km decreasing and veering slowly with height to become
northwesterly near the domain top (Fig. 7.1). For the W. Ara-
bian Sea, the model scale height is set to 3 km. The vertical
eddy diffusion is set to 5 m**2/s. This value was about the
maximum that would allow growth under the parameterization
scheme.

The linear model was first run using a 300 m deep cloud for
all polynomial fits. In all cases except for the 3rd and 4th
order fits, the dominant mode was transverse (Fig. 7.2). In
the 3rd and 4th order cases, bimodal growth appeared with a
tendency for the more longitudinal modes to dominate in the 3rd
order case. Also, as the polynomial order is increased past 4,
the transverse mode increases in relative dominance. Table 7.1
shows the (shear - band) orientation differences for each of
the fits.

When the cloud depth is increased to 5 levels (600 m
thick), a more longitudinal mode becomes evident in the lower
order fits (3 and 5). Also, when surface fluxes are included
with the 3 level cloud, the dominant mode does not change but
the longitudinal mode becomes stronger relative to the

transverse mode. However, even with the 5 level cloud and stationary mode, the "longitudinal mode" never approaches within 20 degrees either of the model depth or cloud layer shear. This is in contrast to the observed cloud rows which were parallel to the cloud layer' shear. Thus, given the observed base state, the model did not duplicate well the observed shallow banding orientation in the w. Arabian Sea. However, a stronger heat flux or deeper cloud produces results more similar to those observed.

Examining the eigenfunctions for some dominant modes, the 5th order fit for the 3 level cloud with surface flux shows plume-like structures for the longitudinal mode throughout the depth with the strongest divergence confined to the subcloud and cloud layer. Because of the cloud parameterization scheme, the strongest thermal perturbations will lie within and near the cloud layer. Across the cloud base, there is a change in sign of relative vorticity with the maximum amplitude located in the subcloud layer and at the cloud top. (Fig. 7.3)

We contrast these results with those from a 5th order transverse mode. Although the plume-like structure exists, a secondary maximum is located above the cloud top in the W and θ fields. A significant difference between the longitudinal mode and the transverse mode exists in the kinematic fields. Strong vorticity exists only above cloud top. Somewhat similar patterns are also noted in the U and $\nabla \cdot \bar{V}$ fields. These comparisons imply that for the more longitudinal mode the cloud band

roots are strongest in the subcloud layer while the transverse mode roots are relatively weak there. (Fig. 7.4)

For the high detail wind profile (9th order), a transverse mode dominates with and without a surface heat flux although stationarity begins to appear in the longitudinal mode when surface heat flux is introduced. When the cloud depth is increased to 5 levels, the short wave cutoff disappears while a stationary mode remains within the analyzed k domain. The higher order eigenfunctions exhibit considerable noise in the vertical.

An examination of the non-dimensional energy budget terms finds $\langle P,K'\rangle$ greatest for the cloud layer while the transverse mode contribution is negative at all levels above the cloud. Similarly, $\langle \overline{K},K'\rangle$ is greatest at and above the cloud layer for the longitudinal mode while the transverse $\langle \overline{K},K'\rangle$ is greatest well above cloud top. The corresponding viscous dissipation diagrams reflect a similar vertical distribution. This suggests for the shallow convective longitudinal modes that the base state and its potential energy are feeding the secondary circulation below and within the cloud layer while the transverse mode circulation is being fed energy in the stable layer by the mean flow but is also having energy extracted by the negative buoyancy term.

TABLE 7.1 WESTERN ARABIAN SEA

LSQRS	NLVL	SHREPS	DESCR	MODE	DIFF	LMAX	EFTIME
1	3LVL	145.2	Transv	65.6	79.6	6.2	14.7
2	3LVL	163.7	Transv	74.7	89.0	6.6	16.7
3	3LVL	160.0	Long	114.4	45.6	6.2	15.5
4	3LVL	164.9	Transv	71.6	93.3	7.9	13.8
5	3LVL	165.1	Transv	60.9	104.2	7.3	8.8
6	3LVL	145.1	Transv	71.6	73.5	7.9	15.7
7	3LVL	154.3	Transv	60.9	93.4	7.3	8.7
8	3LVL	136.9	Transv	84.6	52.1	6.8	12.8
9	3LVL	170.0	Transv	50.7	119.3	5.3	9.5
3	5LVL	155.0	Long.	122.5	32.5	5.8	4.6
5	5LVL	156.2	Long.	111.0	45.2	5.4	4.7
9	5LVL	137.6	Transv	31.0	106.6	4.3	3.5
5	3LVL*	165.1	Transv	60.9	104.2	7.3	8.7
9	3LVL*	170.0	Transv	50.7	119.3	5.3	9.4

* Denotes inclusion of surface heat flux

SHREPS=Cloud layer shear orientation in k domain

DIFF=angle magnitude between MODE and SHREPS

LMAX=band spacing in km.

EFTIME=reciprocal of mode growth rate in minutes

LSQRS=order of fitted wind polynomial
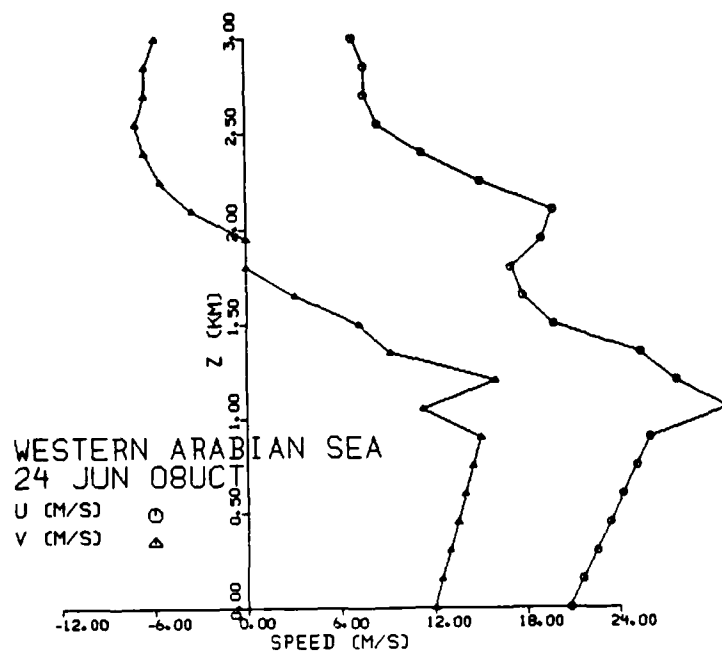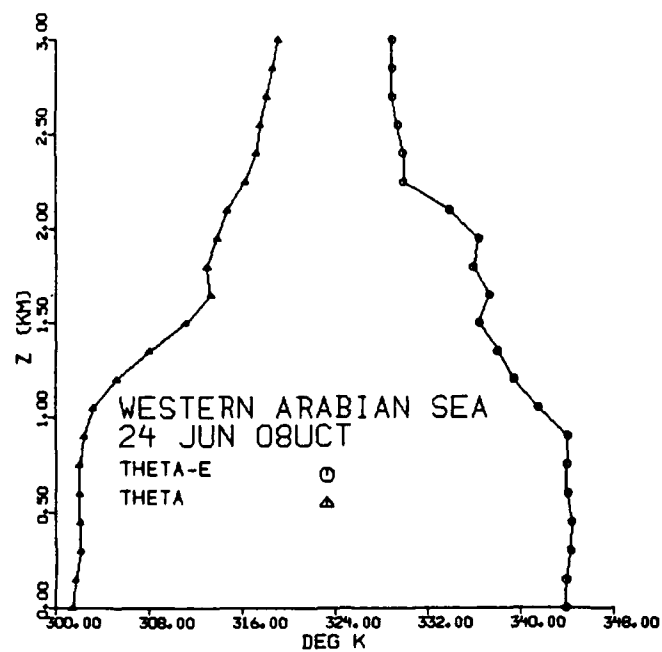
Fig. 7.1 Base State Diagrams for the Western Arabian Sea

116
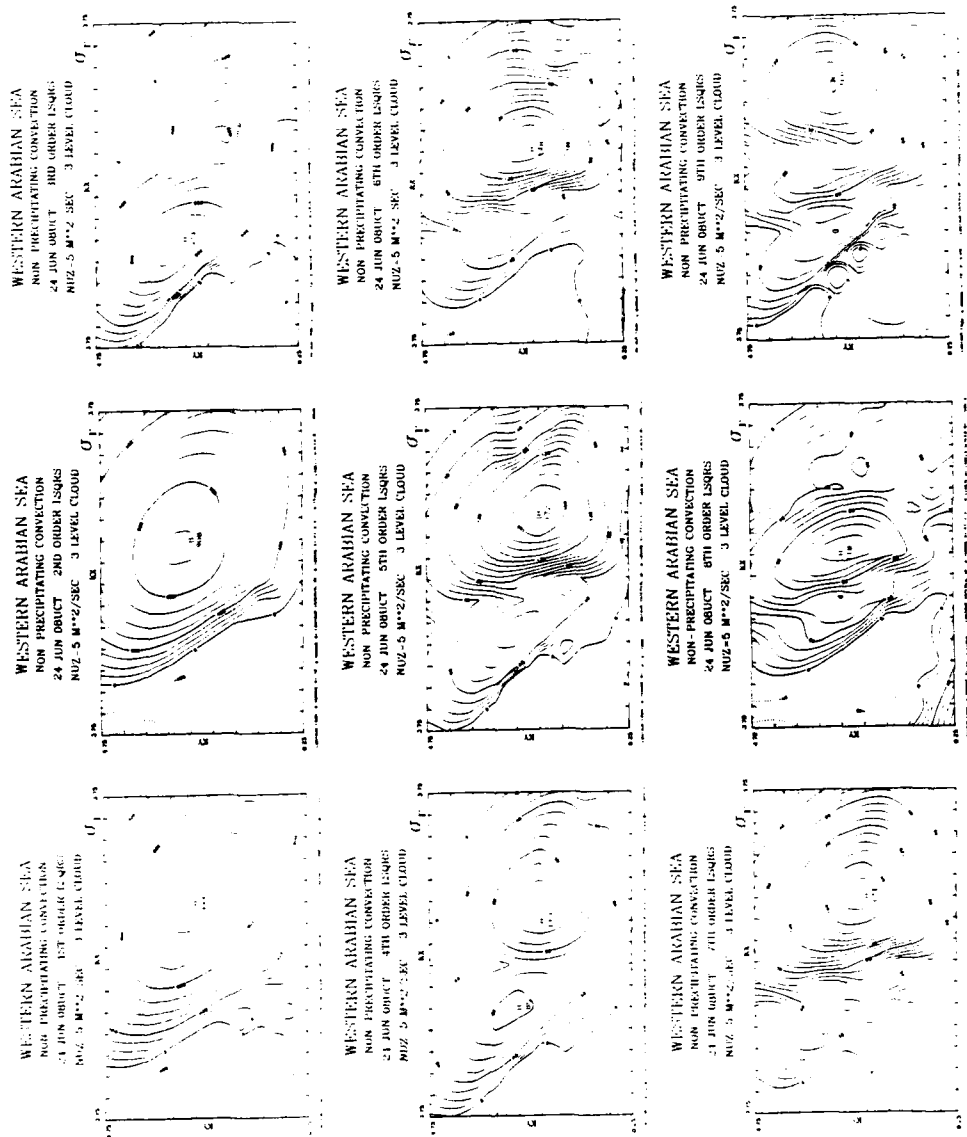
Fig. 7.2 Growth Rates for Varying Polynomial Order (1-9)

117

W EIGENFUNCTION
L=6.2 KM -- NNW

T EIGENFUNCTION
L=6.2 KM -- NNW

Z EIGENFUNCTION
L=6.2 KM -- NNW

U EIGENFUNCTION
L=6.2 KM -- NNW

Fig. 7.3 Longitudinal/5th Order/Sfc. Flux Eigenfunctions

113

Fig.   7.4   Transverse/5th Order/Sfc. Flux Eigenfunctions

119
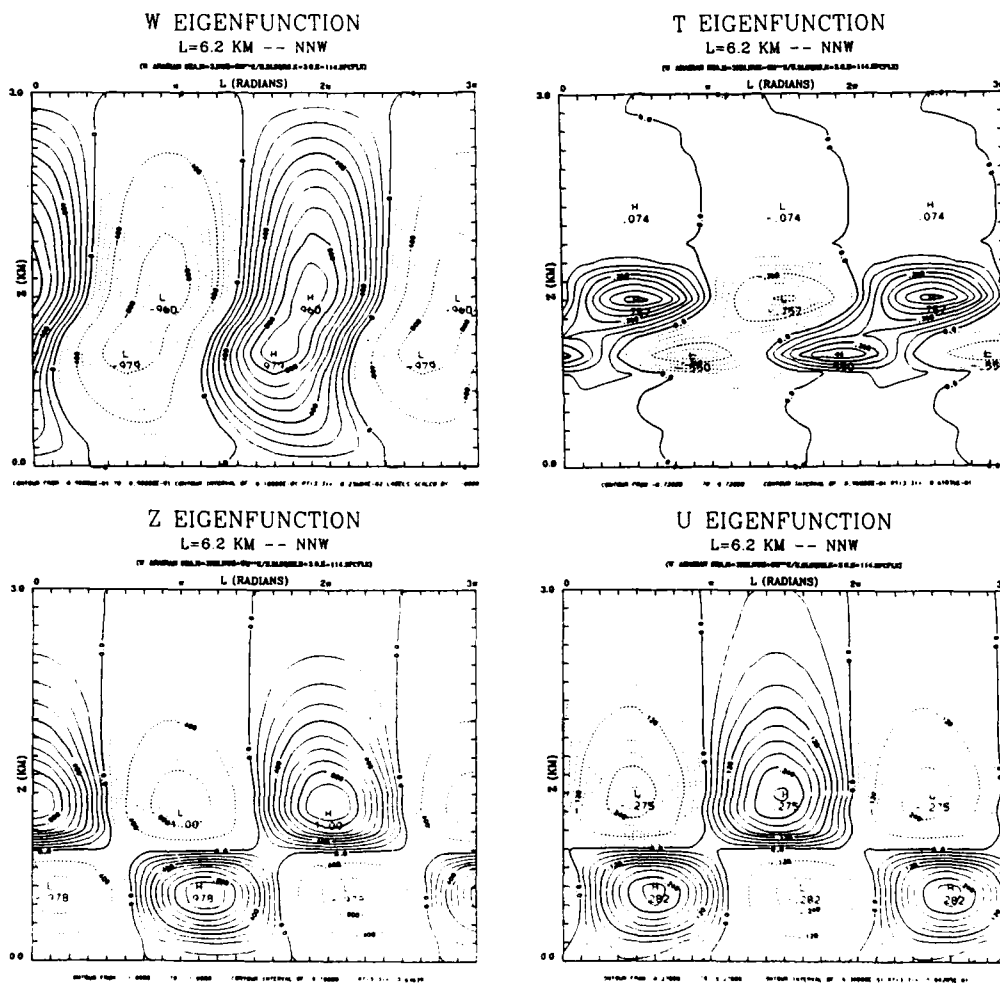
Model Results for Deeper Convection

As a preface to the following discussion, all results presented hereafter incorporate the cumulus parameterization scheme discussed in Chapter IV. This scheme allows for varying the cloud size (and thus the cloud height and lateral entrainment). In addition, the vertical diffusivity is varied including both results from the cloud model as well as "arbitrary" values. A further distinction will be allowed through variation of the moisture accession method in the linear model since precipitation is allowed in the deep convection case. Both methods discussed previously in Chapter IV will be used. Finally, the wind polynomial fit will be allowed to vary as was the case in the W. Arabian Sea.

All of these options allow for many degrees of freedom -- perhaps too many. However, the options do exist to select different combinations if so desired.

c. Central Arabian Sea Results

The central Arabian Sea is characterized by a thermodynamic base state which is less convectively unstable in the lower 4 km and convectively stable above (See Chapter VI). For the horizontal wind, southwesterly flow dominates through the first 4 km, while a northerly component is present between 8 and 11 km. The dominant feature is strong easterly shear throughout the troposphere, especially above 10 km.

The convective heating profiles (Fig. 7.5) are somewhat suppressed with clouds failing to reach the freezing level (for supercooled water) even for a 1500 m radius cloud. This stunting of growth in the cloud model apparently is a result of the weak convective instability in the lower levels (lower specific humidity values in the first 250 hPa) and a more stable layer around 600 hPa. DMSP IR satellite imagery (24 June 0608 UTC) indicates stunted convection near the sounding location (15N 65E) and relatively shallow convection located about 2 ° of ship Deepak. The time dependent cloud model results (Chapter VI) also indicate no propensity for deep cloud growth above the freezing level.

One feature noted during the runs of the linear model was that boundary layer (BL) moisture accession favored shallow convection growth. This is quite evident in Table 7.2. Suppression of growth was observed for cloud depth (CD) moisture accession for all core radii and wind fits. Also, larger core radii, given the same moisture accession and polynomial fit, produced smaller growth rates for the dominant mode.

Given a precipitation efficiency of 1.0, increasing the order of the wind fit produced a stronger longitudinal mode. This is very evident in the k diagrams for 3rd, 6th, and 9th order fits (Fig. 7.6). Also, a minimum in the flux Richardson number domain is associated with the longitudinal mode. This is a recurring feature as will be shown in subsequent sections. While a B maximum (stationarity index) becomes evident, it is

less than 1.0 in magnitude and thus these longitudinal modes are transitive, propagating structures.

Increasing the precipitation efficiency slightly past 1 produces drastic changes in the wavenumber domain. For an increase to P=1.25, the growth rate dominance shifts to a more transverse mode for both 3rd and 9th order fits. The third order fit change is especially dramatic where a relative minimum is established along the longitudinal mode while a strong flux Richardson number decrease is noted in the same region (Fig. 7.7). As the precipitation efficiency is increased to 1.50, the short-wave cutoff disappears and the growth rate becomes strictly a function of wavenumber.

The W eigenfunction for the longitudinal mode exhibits a tilt to the south during the first 2.4 km and a strong tilt to the north above (Fig. 7.8). This same tilt is repeated in the Z and U fields. In the longitudinal case, the Z field is coincident in phase with the W field. The divergence fields indicate the strongest maximum is at the surface with a corresponding maximum at cloud top of the opposite sign. For the transverse mode, the W structures tilt initially towards the west above 1.6 km (perhaps due to the easterly shear) but then show a distinct maximum of opposite sign to the southwest of the low level maximum around 7 km (Fig. 7.9). For the transverse mode, the vorticity field is out-of-phase with the W field and does not extend through the entire cloud depth as does the Z field in the longitudinal case. Also, the U field

123

maximum is located at the surface instead of being situated at 1.6 km as was the longitudinal mode. In addition, there is only a weak secondary divergence maximum located in the cloud layer for the transverse mode.

It is interesting to examine the vertical distribution of secondary flow energy budget terms, especially the real terms for the conversion of mean to perturbation kinetic energy $\langle \overline{K}, K' \rangle$ and potential to perturbation kinetic energy $\langle P, K' \rangle$. Figure 7.10 compares the longitudinal and transverse modes for these two terms. For the longitudinal mode it is obvious that the conversion of mean to perturbation kinetic energy dominates the system. Here, the conversion of perturbation potential energy to kinetic energy plays only a secondary role. For the more dominant transverse mode, however, the roles of the two terms are reversed. Here, the $\langle P, K' \rangle$ term is clearly dominant especially in the cloud depth. Furthermore, through the first 2 km, $\langle \overline{K}, K' \rangle$ is negative suggesting that the secondary flow is feeding kinetic energy to the mean flow in this layer. Thus, these figures seem to explain the observed flux Richardson number distribution for the particular base state.

Another area of interest is the behavior of the longitudinal and transverse mode as the precipitation efficiency is increased. For this, we examine the functions plotted in the k plane --i.e., growth rate, propagation factor B, flux Richardson number, and phase speed (Fig. 7.11). From these diagrams, for the specified method, it is evident that there is

discontinuous behavior at the point P=1.0 for the longitudinal mode. These jump conditions are especially noticeable in the flux Richardson number and phase speed quantities. It is obvious that with a dramatic reduction in phase speed there is also a significant increase of the shear energy conversion term relative to the buoyancy conversion term at the critical point. The discontinuity is also reflected to a lesser extent in the growth rate and stationarity factor B. The transverse mode also exhibits jump conditions but to a lesser extent and at a different precipitation efficiency. Thus, it would appear that for this particular base state, the onset of the stationary mode does not occur in a continuous manner. The applicability of this discontinuity to other base states will be tested in subsequent discussions.

TABLE 7.2 CENTRAL ARABIAN SEA

NUZ	MA	R	LSQ	SHREPS	DESCR	MODE	DIFF	LMAX	EFTIME
10	CD	500	9	98.5	Supp.	--	--	--	
33.7	CD	1000	9	91.3	Supp.	--	--	--	
10	CD	500	3	105.6	Supp.	--	--	--	
33.7	CD	1000	3	111.2	Supp.	--	--	--	
10	BL	500	9	98.5	Long.	93.9	4.6	13.8	58.0
33.7	BL	1000	9	91.3	Supp.	--	--	--	
10	BL	500	3	105.6	Transv.	19.1	86.5	14.6	166.9
33.7	BL	1000	3	111.2	Supp.	--	--	--	
20	BL	500	9	98.5	Long.	96.7	1.8	23.5	122.2
30	BL	500	9	98.5	Long.	98.7	0.2	30.6	274.7
20	BL	1000	9	91.3	Supp.	--	--	--	
10	BL	500	6	91.7	Transv.	30.6	61.1	15.7	161.1
10	BL*	500	3	105.6	Transv.	51.8	53.8	9.6	23.7
20	BL*	500	3	105.6	Transv.	37.7	67.9	14.5	42.5
20	BL*	500	9	98.5	Transv.	30.6	67.9	15.7	43.1
10	BL**	500	3	105.6	Long.	129.1	23.5	8.4	13.8
10	BL	500	1	94.2	Transv.	167.2	72.9	17.8	180.9

* P=1.25   **P=1.50

CD=Cloud depth moisture accession

BL=Boundary layer moisture accession

NUZ=vertical eddy diffusion coefficient (m**2/s)

SHREPS=cloud layer shear orientation in k domain

DIFF=angle magnitude between MODE and SHREPS

LMAX=band spacing in km

EFTIME=reciprocal of mode growth rate in minutes

R=cloud radius in meters

LSQ=order of fitted wind polynomial
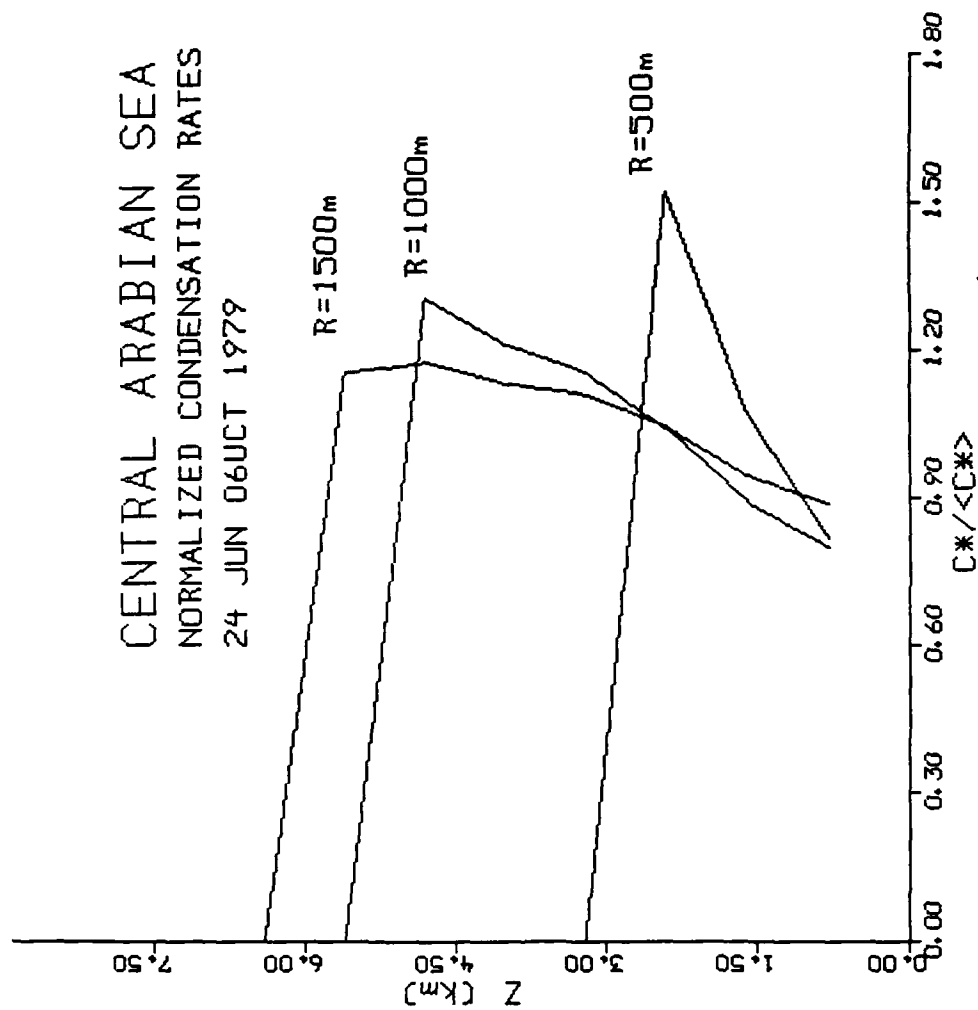
Fig. 7.5 Central Arabian Sea Convective Heating Profiles

CENTRAL ARABIAN SEA
BL MOISTURE ACCESSION
24 JUN 06UCT - 3RD ORDER LSQRS
NUZ=10 M**2/SEC - CORE=500 M

CENTRAL ARABIAN SEA
BL MOISTURE ACCESSION
24 JUN 06UCT - 6TH ORDER LSQRS
NUZ=10 M**2/SEC - CORE=500 M

CENTRAL ARABIAN SEA
BL MOISTURE ACCESSION
24 JUN 06UCT - 9TH ORDER LSQRS
NUZ=10 M**2/SEC - CORE=500 M
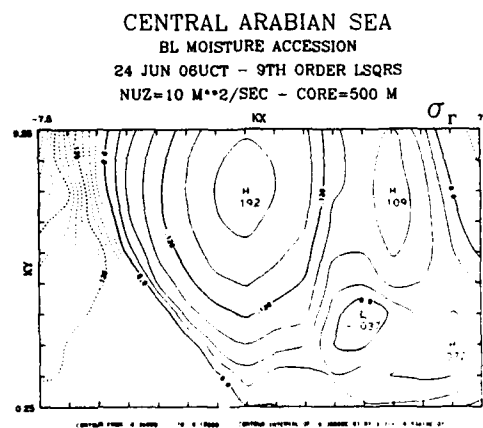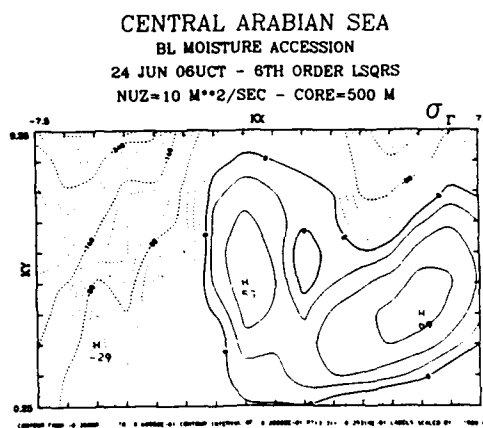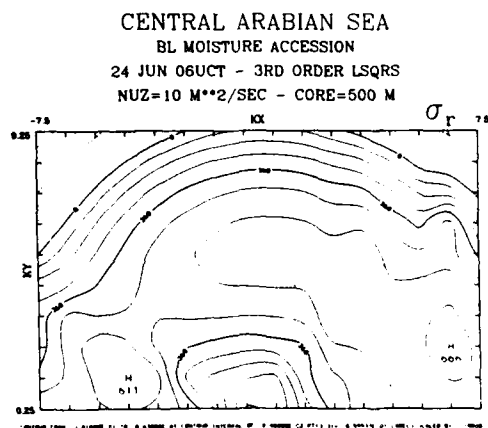
Fig. 7.6 Growth Rate (3rd, 6th, 9th Order)
P=1.0/BL/R=500

CENTRAL ARABIAN SEA
BL MOISTURE ACCESSION (X 1.25)
24 JUN 06UCT – 3RD ORDER LSQRS
NUZ=20 M**2/SEC – CORE=500 M

CENTRAL ARABIAN SEA
BL MOISTURE ACCESSION (X 1.25)
24 JUN 06UCT – 3RD ORDER LSQRS
NUZ=20 M**2/SEC – CORE=500 M

CENTRAL ARABIAN SEA
BL MOISTURE ACCESSION (X 1.25)
24 JUN 06UCT – 9TH ORDER LSQRS
NUZ=20 M**2/SEC – CORE=500 M

CENTRAL ARABIAN SEA
BL MOISTURE ACCESSION (X 1.25)
24 JUN 06UCT – 9TH ORDER LSQRS
NUZ=20 M**2/SEC – CORE=500 M

Fig. 7.7 Growth Rate and Rflux (3rd and 9th Order)
P=1.25/BL/R=500

128

W EIGENFUNCTION

L=13.8 KM -- N

Z EIGENFUNCTION

L=13.8 KM -- N

D EIGENFUNCTION

L=13.8 KM -- N

Fig. 7.8 Longitudinal/9th Order/P=1.0/BL/
R=500 Eigenfunctions

W EIGENFUNCTION
L=14.6 KM -- ENE

Z EIGENFUNCTION
L=14.6 KM -- ENE

U EIGENFUNCTION
L=14.6 KM -- ENE

Fig. 7.9 Transverse/3rdOrder/P=1.0/BL/R=500
Eigenfunctions

130

Fig. 7.10 Longitudinal and Transverse Mode Energy Transfers

131
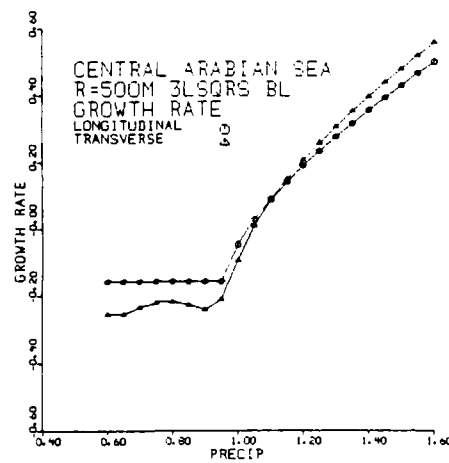
Fig. 7.11 Longitudinal and Transverse Mode Behavior as f(P)

d. Grossman Stable Composite

Another base state which favors shallow convection is the Grossman stable composite sounding (Grossman and Durran, 1984). θ_e base state properties suggest moderate convective instability from the surface to about 3 km. Above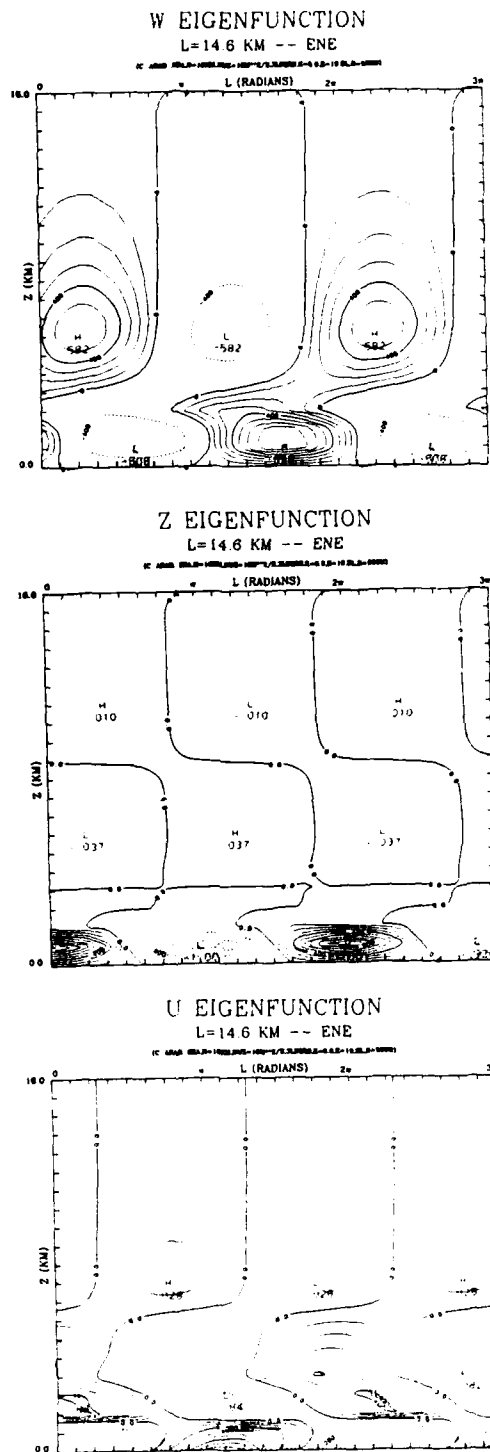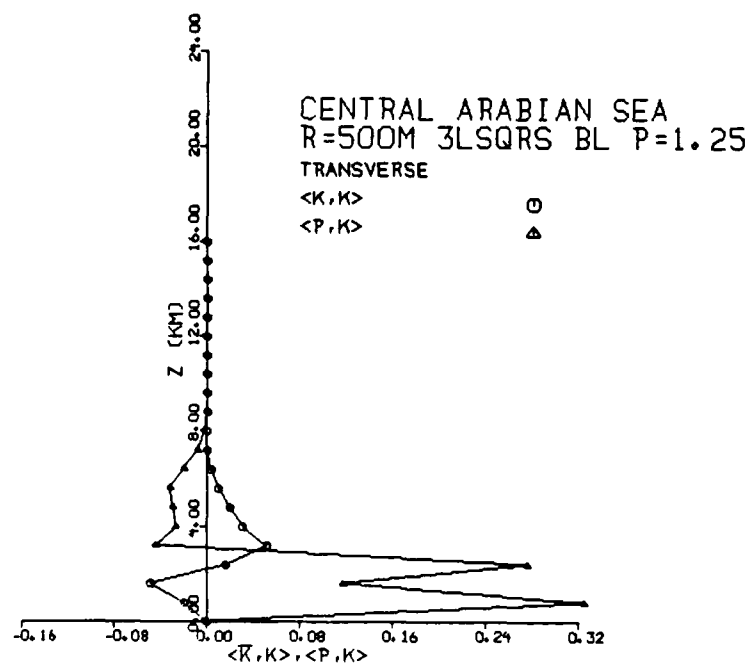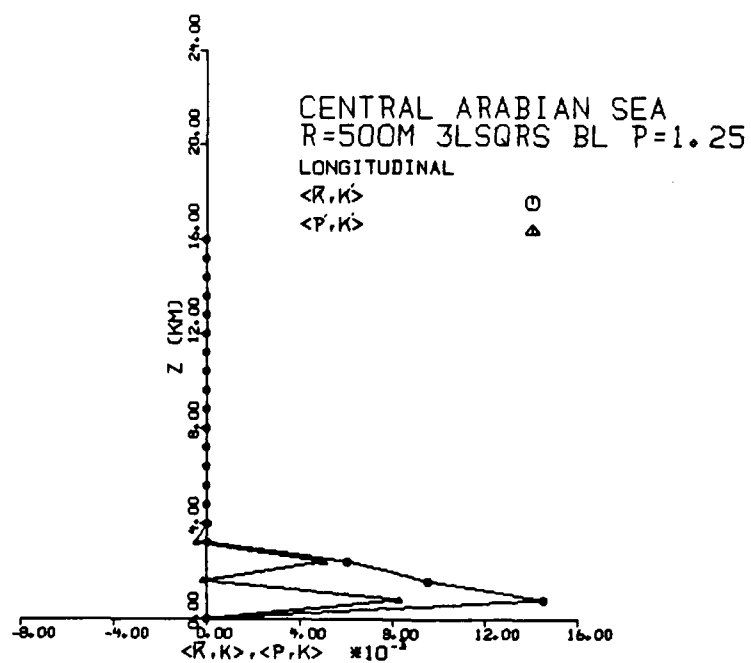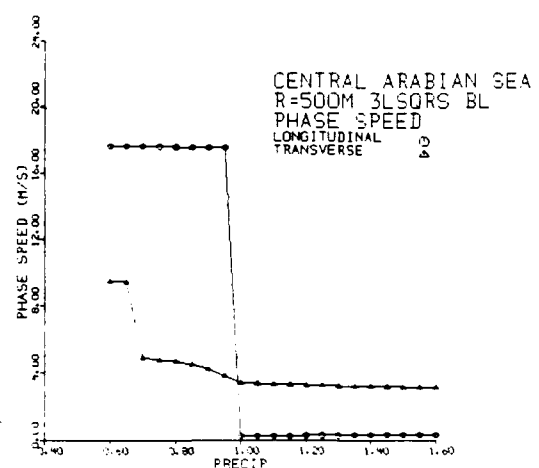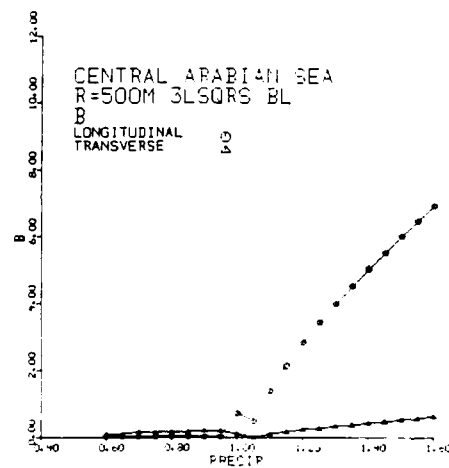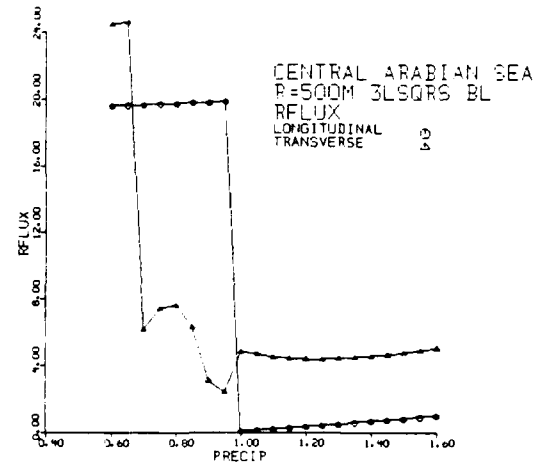 that level convective stability dominates. The 1DTD cloud model shows no propensity for upper level development. The 1DSS model shows cloud tops varying markedly with core radius (Fig. 7.12). For cloud core radii greater than 1 km, the cloud tops extend above the freezing level.

Since no wind base state was provided by Grossman and Durran, an E-W zonal profile was used with the sounding (see chapter VI) characteristic of the E. Arabian Sea. This profile was developed by Ogura and Yoshizaki (1988) for a numerical study of orographic-convective precipitation over the E. Arabian Sea. The u profile possesses characteristic features of the region --a strong low level SW jet just above cloud base and strong easterly shear through most of the troposphere. The inclusion of a base state wind with no turning produces symmetric patterns in the wavenumber domain.

Table 7.3 presents a summary of results. One immediate conclusion from the table is that modes associated with large core radii and smoother profiles or BL moisture accession are suppressed. Also, the longitudinal mode is associated with the high order (detailed 9th order) polynomial fit. A comparison

of the 3rd and 9th order fits (Fig. 7.13) shows the cubic poly-
nomial cannot represent the low-level jet while the 9th order
polynomial can. It appears the low level maximum here is the
critical factor in determining the existence of a longitudinal
mode provided the moisture accession and cloud size are also
conducive to its formation.

Examining the k diagrams with no enhanced moisture, it is
obvious a special set of circumstances is required for the for-
mation of the dominant longitudinal mode. These are achieved
at least with a 9th order fit, BL moisture accession, and 500 m
core radius. A 3rd order fit produces a less well defined but
dominant transverse mode.   The wavelength for both dominant
modes is about 12 km. What is remarkable is the dramatic
change in growth rate pattern associated with a rather subtle
change in the base state wind. Also, both fits result in a
stationary mode being developed. Furthermore, the 3rd order
wave fields tend to be non-dispersive (Fig. 7.14).   Increasing
the cloud radius to 1000 m (top = 6.4 km) rapidly destroys
growth and weakens the stationary mode.

Tests were also run for values of b (moistening parameter)
other than 0.   The principle effects of "negative" b were to
enhance the growth rate, decrease the wavelength of the dom-
inant modes, enhance the stationarity of the longitudinal
modes, and for BL accession, increase the non-dispersive char-
acter of the wave field. However, even with enhanced moisture,
only a 9th order fit would support a longitudinal mode.

Next, examining the behavior of the vertically-integrated mean eigenfunctions over the wave number domain, the maximum eigenfunctions tend to favor modes associated with N-S bands (Fig. 7.15). In the case of W, the short wavelength N-S modes are favored. For θ , and especially Z, the entire spectrum of N-S modes is preferred. However, the maximum U values are associated with the larger wavelength E-W or longitudinal modes. The 3rd order fit shows a somewhat similar pattern except these eigenfunctions favor a longer E-W component.

The vertical distribution of energy transfer terms is shown in Fig. 7.16. The $\langle\bar{K},K'\rangle$ term dominates the $\langle P,K'\rangle$ term. Frictional dissipation of perturbation kinetic energy $\langle DK'\rangle$ to some extent offsets the other two terms in the cloud layer. For the transverse mode, the situation is reversed. The $\langle P,K'\rangle$ term dominates in the cloud layer with $\langle\bar{K},K'\rangle$ reaching its maximum amplitude just below cloud top. $\langle DK'\rangle$ is largest at the surface decreasing sharply up to 1.6 km and slowly decreasing thereafter. At 3.2 km, a maximum in negative buoyancy flux is associated with a maximum in conversion from the mean flow to perturbation kinetic energy.

A cross-section for the dominant longitudinal mode for BL moisture accession shows vertical velocity to be in-phase with perturbation potential temperature and 180° out-of-phase with the divergence (Fig. 7.17). The Z fields are 90° out-of-phase with the vertical velocity fields. The WU cross-sections imply convergence-divergence of U in the cloud layer. For a

transverse mode, the W and Θ fields are 90° out-of -phase and only one maximum of each field is observed in the cloud layer zone (Fig. 7.18). Also, the relative vorticity field is weaker and detached from the lower two levels.

As was the case in the central Arabian Sea, the individual mode behavior exhibits discontinuities as b is decreased (Fig. 7.19). For the longitudinal mode, the "jump" occurs at P=0.8 (b=0.2) and for the transverse mode the critical b is 0. Again, there is the jump behavior of opposite sign associated with the flux Richardson number --a drastic decrease at P=0.8 for the longitudinal mode and a drastic increase for the transverse mode at P=1.0. In addition, there is a Δ P lag of 0.2 between the jump condition in the longitudinal mode and transverse mode. All four analyzed variables exhibit the same critical point of discontinuity.

TABLE 7.3   GROSSMAN STABLE COMPOSITE

NUZ	MA	R	LSQ	SHREPS	DESCR	MODE	DIFF	LMAX	EFTIME
14	BL	500	9	90	Long	93.4	3.4	12.2	36.8
10	CD	1000	9	90	NW	52.4	38.6	24.5	135.7
14	BL	500	3	90	Transv	150.5	60.5	11.7	36.2
10	CD	500	9	90	Transv	5.7	84.3	40.0	340.0
28.3	BL	1000	9	90	Supp	--	--	--	
28.3	BL	1000	3	90	Supp	--	--	--	
45.0	CD	1500	9	90	Supp	--	--	--	
28.3	CD	1000	9	90	Supp	--	--	--	
45.0	CD	1500	3	90	Supp	56.3	--	--	
28.3	CD	1000	3	90	Supp	--	--	--	
13.6	CD	500	3	90	Supp.	--	--	--	
13.6	CD	500*	3	90	Supp.	--	--	--	
13.6	CD	500*	9	90	Supp.	--	--	--	
14.	BL	500**	3	90	NE	136.0	46.	9.7	17.6
14.	BL	500*	3	90	Supp.	--	--	--	
14.	CD	500*	9	90	Supp.	--	--	--	
14.	CD	500**	9	90	Transv	4.1	85.9	28.7	146.1
14.	CD	500**	3	90	Transv	5.7	84.3	40.0	10119.
14.	BL	500**	9	90	Long	93.1	3.1	10.9	18.1

* P=0.8   **P=1.2

CD=cloud depth moisture accession

BL=boundary layer moisture accession

NUZ=eddy diffusion coefficient $(m^{**}2/s)$

SHREPS=cloud layer shear orientation in k domain

DIFF=angle magnitude between MODE and SHREPS

LMAX=band spacing in km.

EFTIME=reciprocal of mode growth rate in minutes

R=cloud radius in meters

LSQ=order of fitted wind polynomial
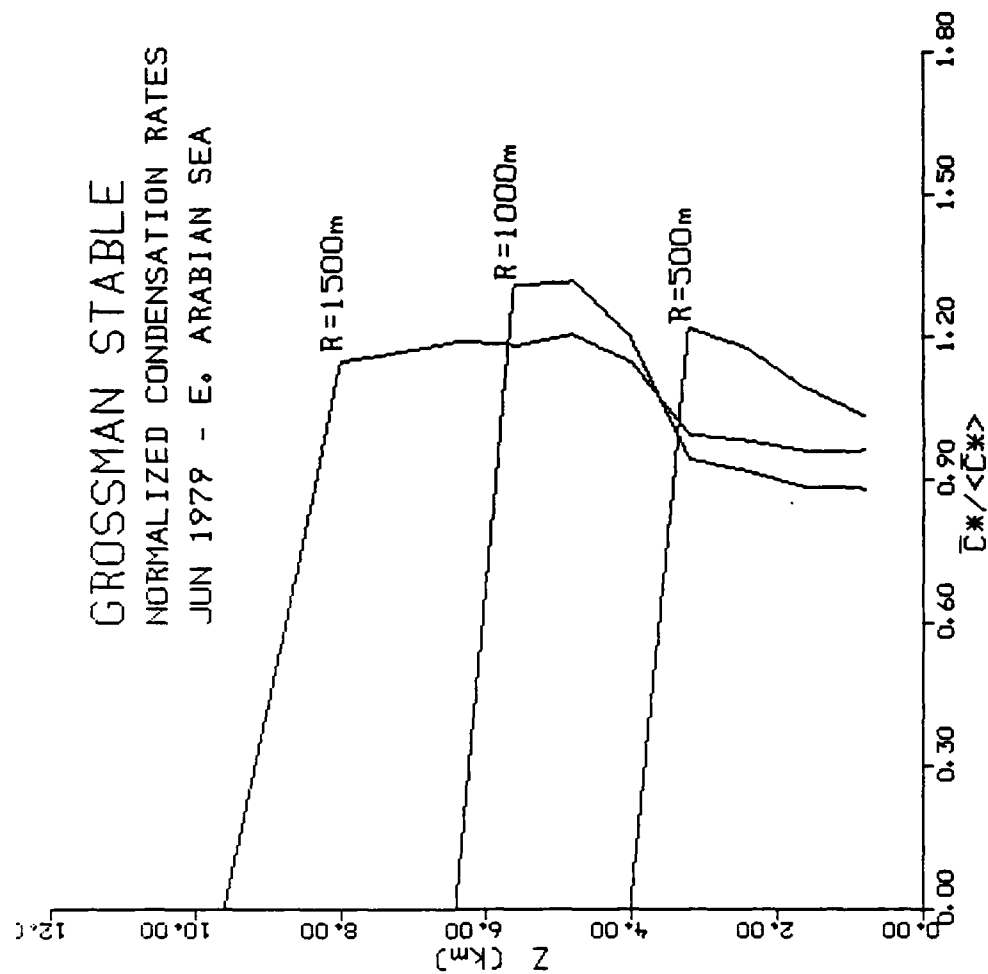
Fig. 7.12 Grossman Stable Convective Heating Profiles
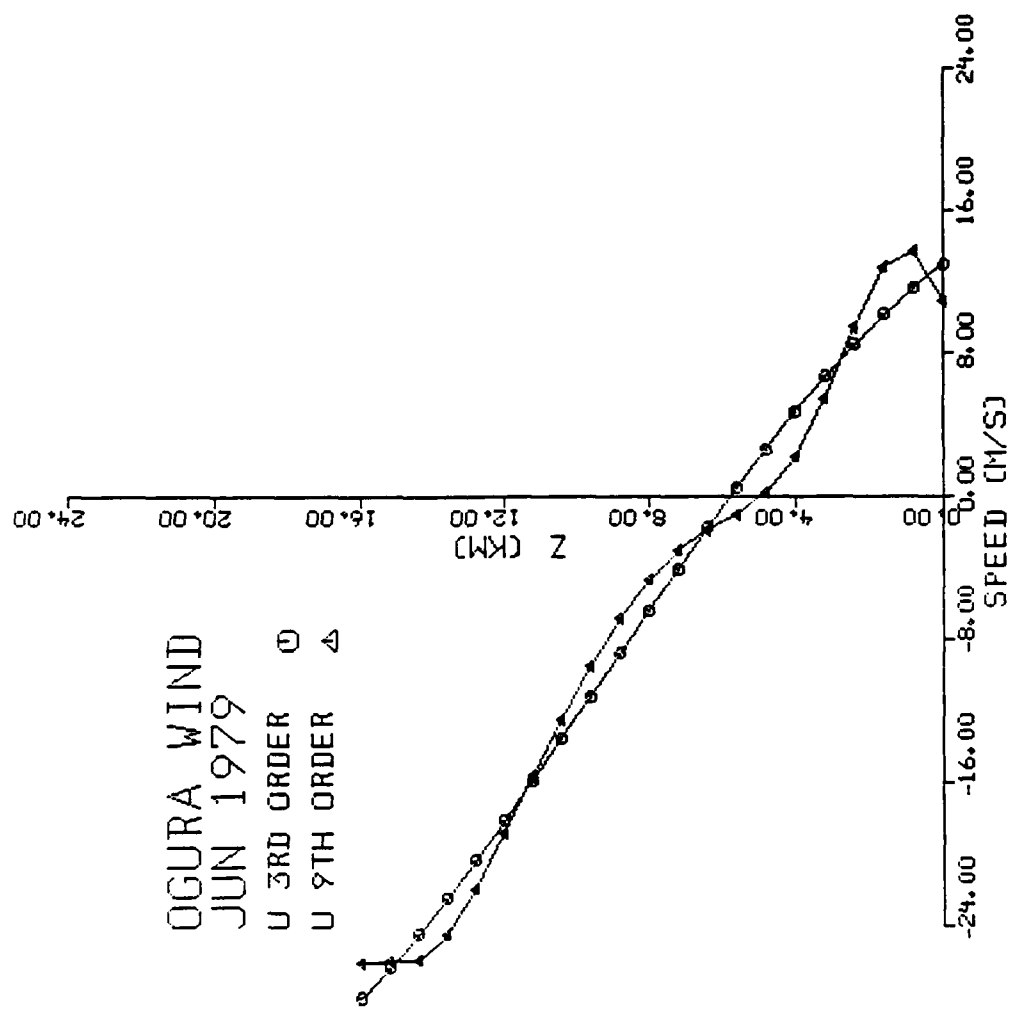
Fig. 7.13 3rd and 9th Order Wind Fits

GROSSMAN COMPOSITE (STABLE)
BL MOISTURE ACCESSION
JUN 1979 – 3RD ORDER LSQRS
NUZ=14 M**2/SEC – CORE=500 M

GROSSMAN COMPOSITE (STABLE)
BL MOISTURE ACCESSION
JUN 1979 – 3RD ORDER LSQRS
NUZ=14 M**2/SEC – CORE=500 M

GROSSMAN COMPOSITE (STABLE)
BL MOISTURE ACCESSION
JUN 1979 – 9TH ORDER LSQRS
NUZ=14 M**2/SEC – CORE=500 M

GROSSMAN COMPOSITE (STABLE)
BL MOISTURE ACCESSION
JUN 1979 – 9TH ORDER LSQRS
NUZ=14 M**2/SEC – CORE=500 M

Fig. 7.14 Growth Rate and Phase Speed (3rd and 9th Order) P=1.0/BL/ R=500

GROSSMAN COMPOSITE (STABLE)
BL MOISTURE ACCESSION
JUN 1979 - 9TH ORDER LSQRS - P=1.2
NUZ=14 M**2/SEC - CORE=500 M

GROSSMAN COMPOSITE (STABLE)
BL MOISTURE ACCESSION
JUN 1979 - 9TH ORDER LSQRS - P=1.2
NUZ=14 M**2/SEC - CORE=500 M

GROSSMAN COMPOSITE (STABLE)
BL MOISTURE ACCESSION
JUN 1979 - 9TH ORDER LSQRS - P=1.2
NUZ=14 M**2/SEC - CORE=500 M

GROSSMAN COMPOSITE (STABLE)
BL MOISTURE ACCESSION
JUN 1979 - 9TH ORDER LSQRS - P=1.2
NUZ=14 M**2/SEC - CORE=500 M

Fig. 7.15   Dominant Modes' Mean Eigenfunction Amplitudes

141

W EIGENFUNCTION
L=12 1 KM -- N

T EIGENFUNCTION
L=12 1 KM -- N

D EIGENFUNCTION
L=12 1 KM -- N

WU EIGENFUNCTION
L=12 1 KM -- N

**Fig. 7.17 Longitudinal/9th Order/P=1.0/BL/R=500
Eigenfunctions**

143

Fig. 7.16 Longitudinal and Transverse Mode Energy Transfers

W EIGENFUNCTION

L=40.0 KM -- E

T EIGENFUNCTION

L=40.0 KM -- E

Z EIGENFUNCTION

L=40.0 KM -- E
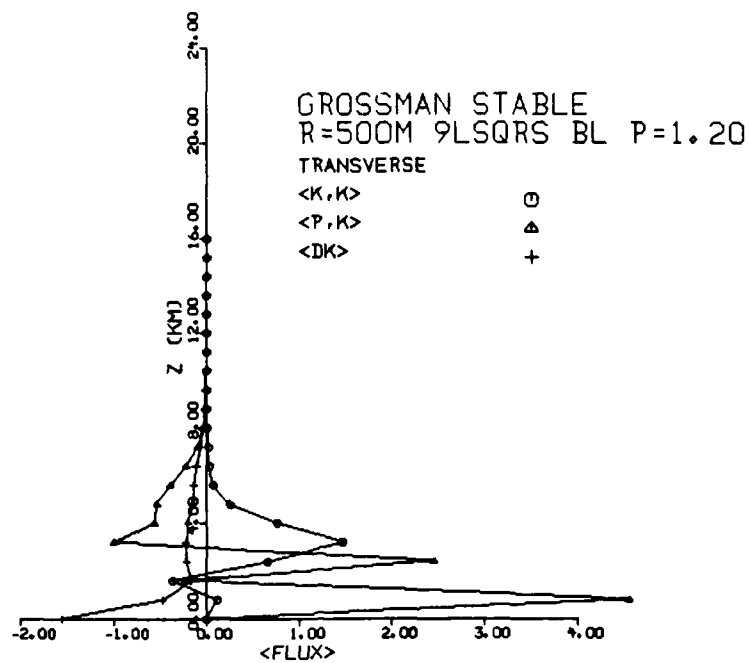
Fig. 7.18 Transverse/9th Order/P=1.0/CD/R=500
Eigenfunctions
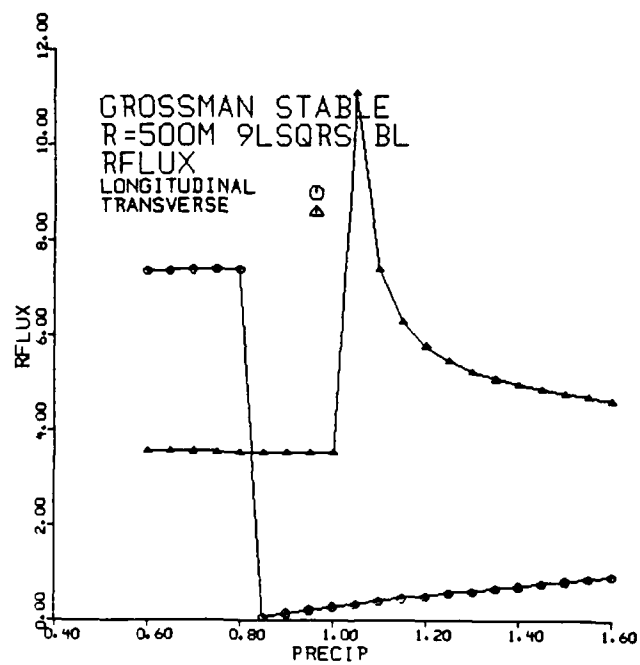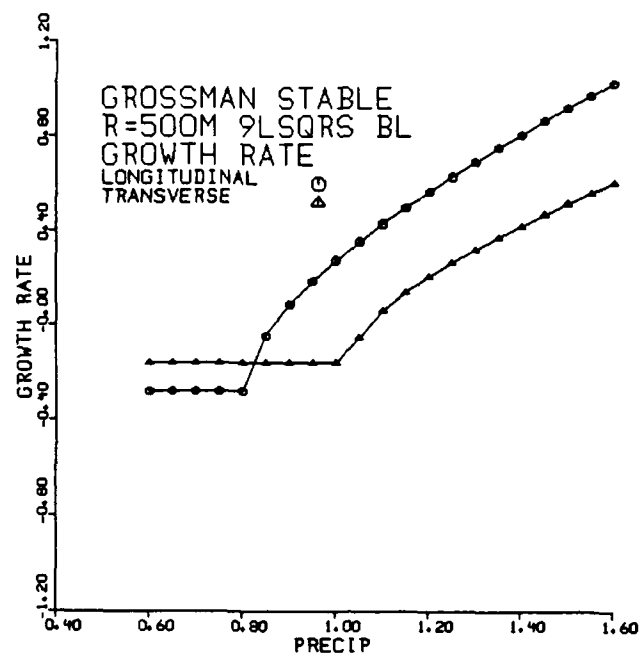
Fig. 7.19 Longitudinal and Transverse Mode Behavior as f(P)

145

e. Monsoon Onset Base State

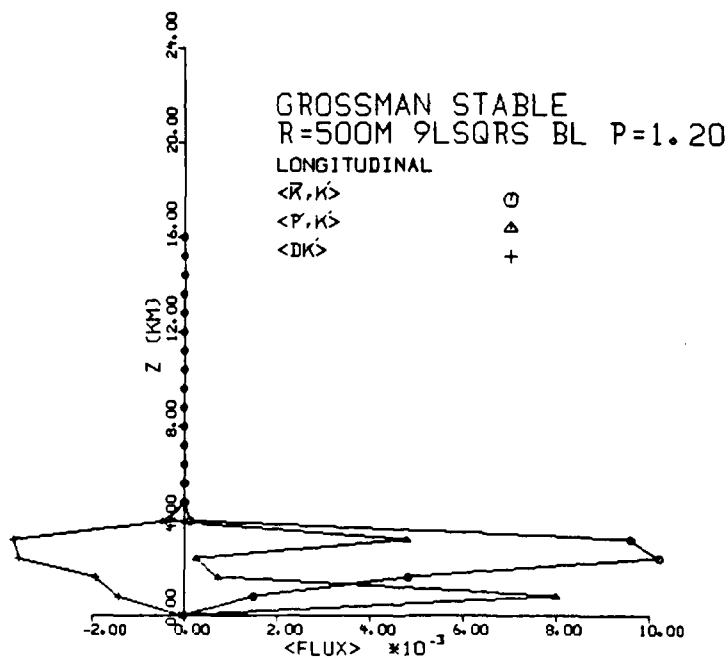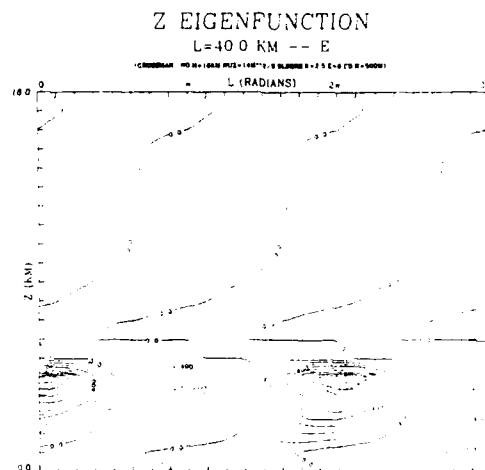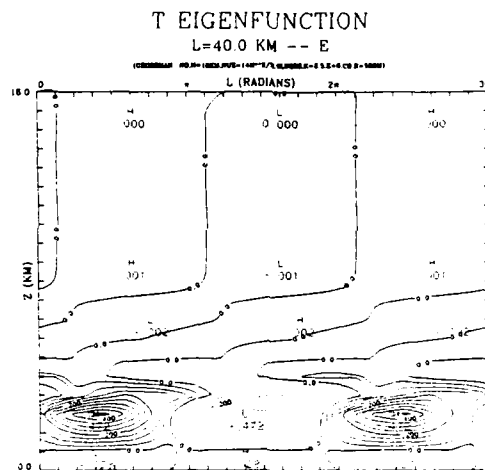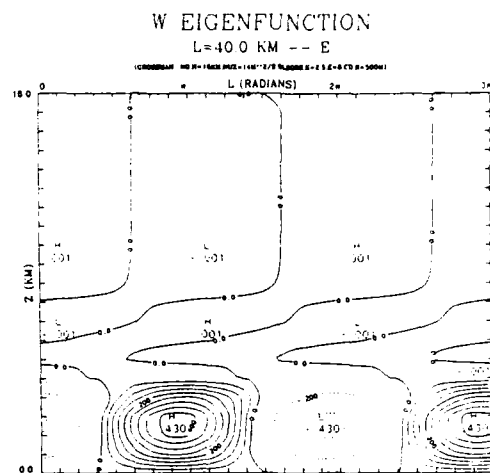The monsoon onset base state is characterized by low level convective instability below 4 km and is convectively unstable above. In this respect, it is little different from the other deep convection profiles. However, through most of the depth above 4 km, it is less convectively unstable than the other soundings. For the time dependent model, growth is almost immediately initiated above the freezing level (see chapter VI). The 1DSS model shows a propensity for deep convection above the freezing level for cloud radii greater than 500 m. (Fig. 7.20)

The vertical distribution of the horizontal wind exhibits a low level westerly jet and strong upper level easterly shear. Weaker northerly flow is present from about 3.2 km to 9.6 km. For this base state study, the 3rd and 9th order polynomials are used predominantly for wind fitting. The 3rd order fit retains the easterly and northerly shear profiles of the base state but removes the low level jet. The 9th order fit dampens the peaks but appears to retain the essential character of the flow. (See Fig. 7.21)

Table 7.4 displays a summary of the model runs. In general, the longitudinal mode dominance occurs only in cloud depth moisture accession. The one exception which includes a 3rd order fit has a rather large e-folding time (216 min.). Another noticeable feature is the predominance of NW-SE dom-

inant modes for values of precipitation efficiency =1.0 except for three cases. However, all of these modes are essentially propagating modes. Stationarity does not begin to set in until P exceeds 1.0. In some instances, however, the Richardson flux number shows signs of characteristic stationary organization in the wavenumber domain before the critical point is reached.

Some k diagrams for P=1.0 and varied moisture accession method and polynomial order are compared (Fig. 7.22 and 7.23). Growth rate distributions tend to be bi-modal with the higher order polynomials for BL accession producing a more transverse mode. The behavior of the CD accession is not as dramatic with the dominant modes shifting to a slightly more longitudinal orientation. The Richardson flux field for BL accession displays a minimum surrounding the longitudinal mode. The flux Richardson number (Rflux) field for the CD accession is more chaotic. In both cases, B is much less than 1.0 and the bands may be considered as transitive or propagating relative to the surface.

Next, examining the effect of increasing P, drastic change occurs in the wave number domain. NW-SE short wavelength modes begin to assume a non-dispersive character for the 3rd order polynomial. The dominant modes split for the third order fit into two transverse modes. For the 9th order fit, the dominant modes congeal to produce a stronger E-W alignment. However, no characteristic longitudinal signal in the flux Richardson number domain develops. As P --> 1.5, a longitudinal mode

dominates both for the 3rd and 9th order fits for cloud depth moisture accession. The growth rate fields tend to be smoother with the 3rd order fit and there is no bimodal tendency as exists with the 9th order fit. However, the more transverse modes still dominate the BL accession k fields. It is interesting to note that linear shear will produce a weakly bi-modal longitudinal mode.

Examining the 9th order CD eigenfunctions for P=1.5, W fields show the greatest magnitude in the upper half of the cloud layer (Fig. 7.24). The eigenfunctions, while displaying considerable noise, show a maximum near cloud base and cloud top, thus roughly corresponding in phase to the W patterns. However, the Z fields, while showing both lower and upper level maxima, are about 45° out- of-phase with W. A strong U maximum is observed at 1.6 km while a secondary U maximum is observed at 7.2 km. No such corresponding jet develops in the V field. Likewise, maximum vertical transports of U are observed at 1.6 km and 6.4 km.

What effect does the different order polynomial have on the energy conversion terms? For this, we examine both longitudinal and transverse dominant modes (Fig. 7.25). Examining first the longitudinal mode, for both the 9th and 3rd order fits, we see generally positive values for $\langle \bar{K},K' \rangle$ and $\langle P,K' \rangle$ terms. However, for the 9th order fits, the $\langle \bar{K},K' \rangle$ term is relatively higher in the upper layer and the $\langle P,K' \rangle$ term is relatively higher in the lower layer than is the case with the

3rd order fit. Also, the dissipation of kinetic energy due to friction is relatively smaller in the 3rd order case compared to the 9th order. For the transverse mode, a greater predominance of $\langle P,K'\rangle$ is noted for both fits while $\langle \overline{K},K'\rangle$ tends to be more negative especially for the 3rd order fit. To offset the stronger $\langle P,K'\rangle$ in the transverse mode, the $\langle D,K'\rangle$ term shows larger values in the upper levels especially for the 9th order fits.

Finally, examining the mode behavior, the discontinuities or jump points still appear as P increases but to a lesser degree in the transverse mode (Fig. 7.26). For the 3rd order longitudinal mode, the jump point is 1.05. For the transverse mode, the critical point is 1.25. These values are considerably higher than those observed for shallow convection. Hence, from this we may suggest that deeper convection delays the onset of the stationary mode relative to less deep convection. Again, spectacular drops are evident in both phase speed and Richardson flux as the stationary mode is fully established.

TABLE 7.4   MONSOON ONSET

NUZ	MA	R	LSQ	SHREPS	DESCR	MODE	DIFF	LMAX	EFTIME
60	CD	1000	9	91.1	NW	56.3	34.8	37.2	85.4
31.7	BL	1000	3	92.4	NW	127.6	35.2	24.5	184
31.7	BL	1000	9	91.1	NW	50.5	40.6	18.3	51
60	CD	500	3	105.0	Long.	111.8	6.8	74.7	216.0
60	CD	1500	9	91.1	NW	56.3	34.8	37.2	130.2
12	BL	500	3	105.0	NW	48.7	56.3	12.1	195.6
12	BL	500	9	107.0	Transv.	39.8	67.2	10.3	26.3
62.8	BL	1500	9	91.1	NW	42.0	49.1	29.9	144.7
62.8	BL	1500	3	92.4	NE	123.7	31.3	37.2	774.9
11.5	CD	500	3	105.0	NE	153.4	48.4	20.0	61.9
62.8	CD	1500.	3	92.4	NW	42.0	50.4	29.9	111.1
31.7	CD	1000	9	91.1	Long.	65.2	25.9	28.1	55.8
62.8	CD	1500	9	91.1	NW	56.3	34.8	37.2	140.9
11.5	CD	500	9	107.0	Long.	105.9	1.1	18.4	47.0
31.7	CD	1000	3	92.4	NW	52.4	40	24.5	54.1
31.7	CD	1000*	1	80.0	Long.	103.5	23.4	15.6	12.1
31.7	BL	1000*	3	92.4	Transv.	26.6	65.9	13.8	19.0
31.7	CD	1000*	9	91.1	Long	94.6	3.5	16.0	16.8
31.7	CD	1000**	3	42.9	Transv.	92.4	49.6	21.0	32.1
31.7	CD	1000**	9	91.1	Long.	65.2	25.9	28.1	41.8
31.7	CD	1000*	3	92.4	NE	123.7	31.3	15.9	11.8
31.7	CD	1000	1	80.0	NE	123.7	43.6	37.2	106.6

* P=1.5   **P=1.2

CD=cloud depth moisture accession

BL=boundary layer moisture accession

NUZ=eddy diffusion coefficient (m**2/s)

SHREPS=cloud layer shear orientation in k domain

DIFF=angle magnitude between MODE and SHREPS

LMAX=band spacing in km.

EFTIME=reciprocal of mode growth rate in minutes

R=cloud radius in meters
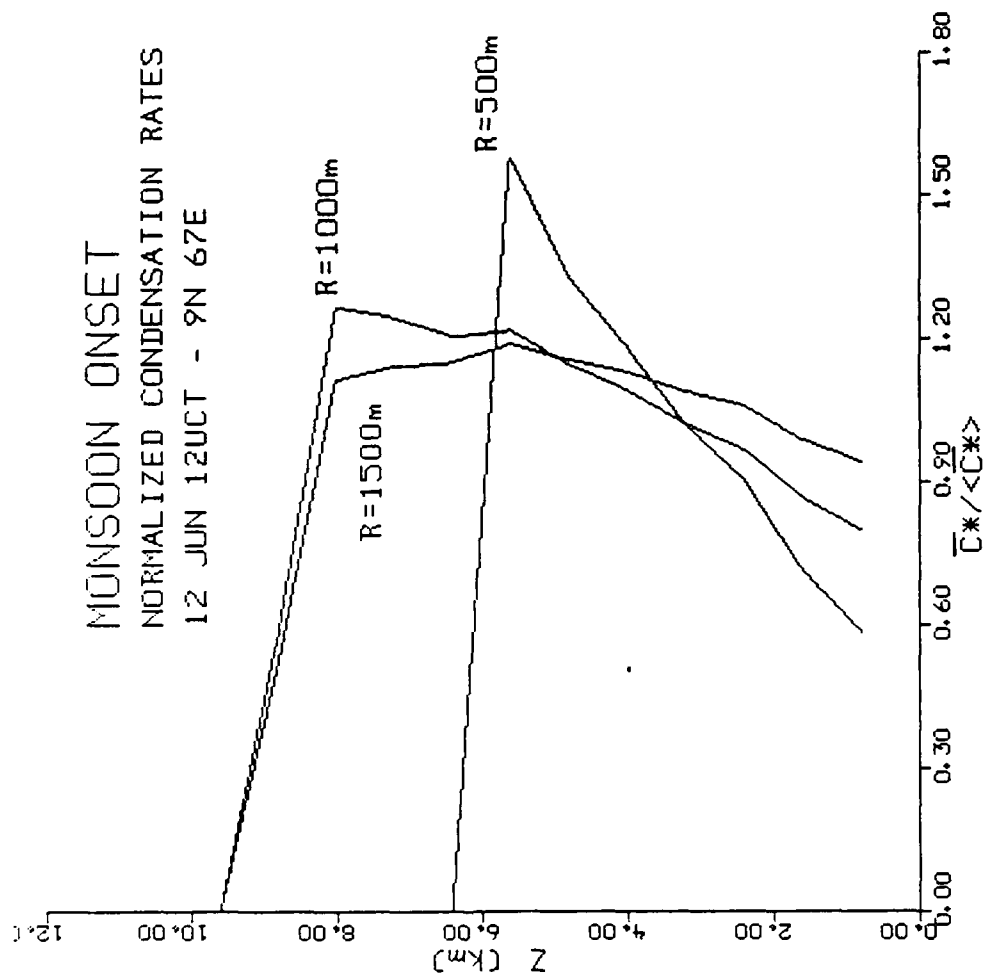
Fig. 7.20 Monsoon Onset (Ship VOLNA) Convective Heating Profiles
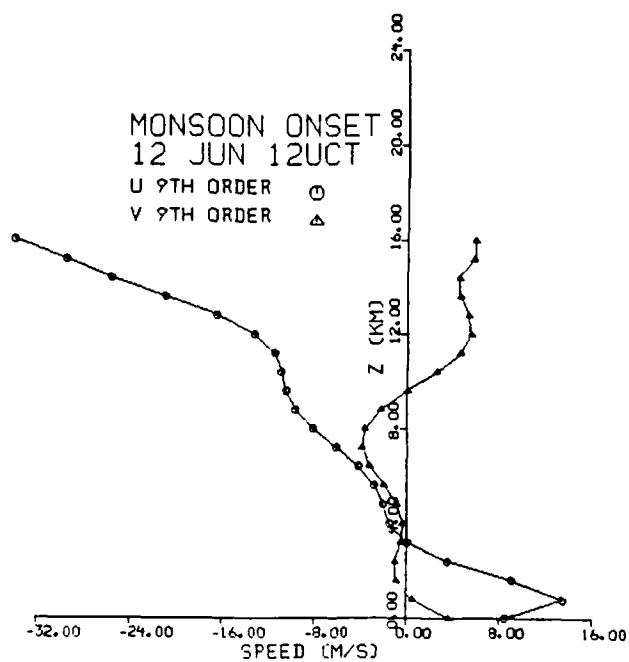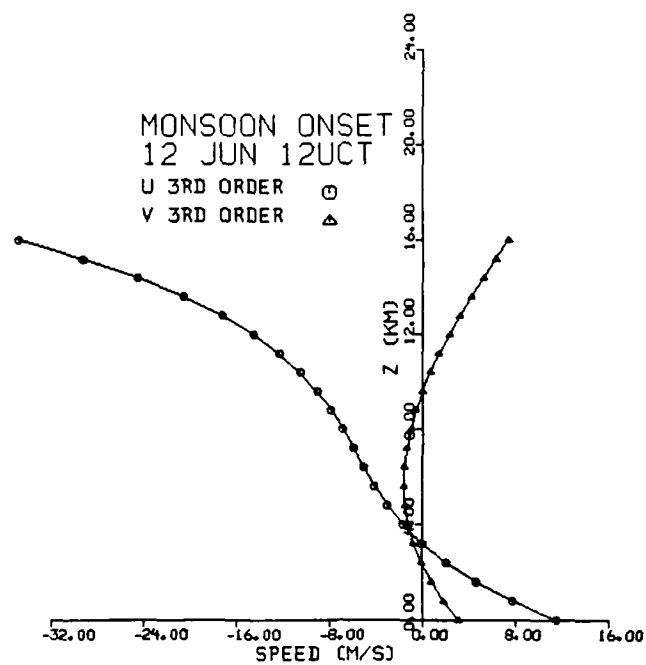
Fig. 7.21 3rd and 9th Order Wind Fits

152

MONSOON ONSET (9N 67E)
BL MOISTURE ACCESSION
12 JUN 12UCT – 3RD ORDER LSQRS
NUZ=32 M**2/SEC – CORE=1000 M
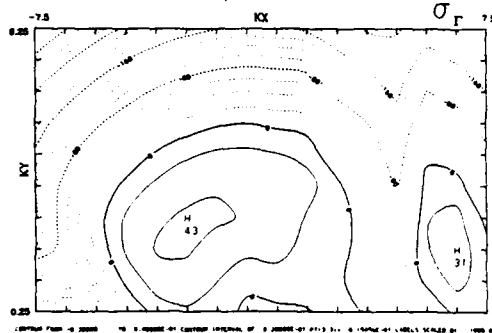
MONSOON ONSET (9N 67E)
BL MOISTURE ACCESSION
12 JUN 12UCT – 3RD ORDER LSQRS
NUZ=32 M**2/SEC – CORE=1000 M
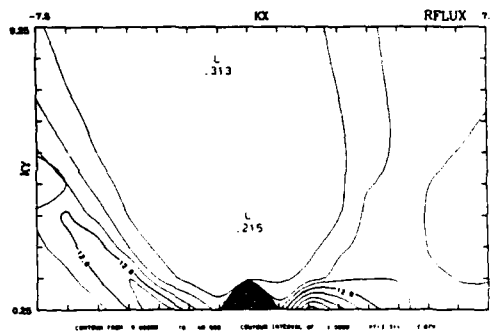
MONSOON ONSET (9N 67E)
BL MOISTURE ACCESSION
12 JUN 12UCT – 9TH ORDER LSQRS
NUZ=32 M**2/SEC – CORE=1000 M
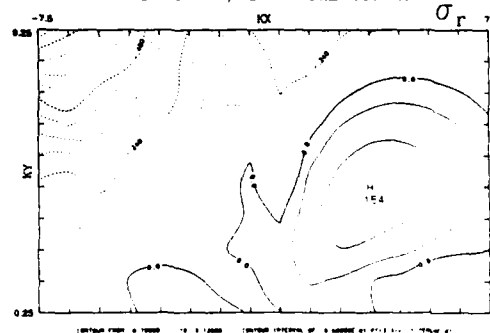
Fig. 7.22 Growth Rate and Rflux (3rd and 9th
Order) P = 1.0/BL/ R = 1000

MONSOON ONSET (9N 67E)
CLOUD DEPTH MOISTURE ACCESSION
12 JUN 12UCT – 3RD ORDER LSQRS
NUZ=32 M**2/SEC – CORE=1000 M

MONSOON ONSET (9N 67E)
CLOUD DEPTH MOISTURE ACCESSION
12 JUN 12UCT – 3RD ORDER LSQRS
NUZ=32 M**2/SEC – CORE=1000 M

MONSOON ONSET (9N 67E)
CLOUD DEPTH MOISTURE ACCESSION
12 JUN 12UCT – 9TH ORDER LSQRS
NUZ=32 M**2/SEC – CORE=1000 M

MONSOON ONSET (9N 67E)
CLOUD DEPTH MOISTURE ACCESSION
12 JUN 12UCT – 9TH ORDER LSQRS
NUZ=32 M**2/SEC – CORE=1000 M

Fig. 7.23 Growth Rate and Rflux (3rd and 9th Order)
P=1.0/CD/R=1000

Fig. 7.24 Longitudinal/9th Order/P=1.5/CD/R=1000
Eigenfunctions
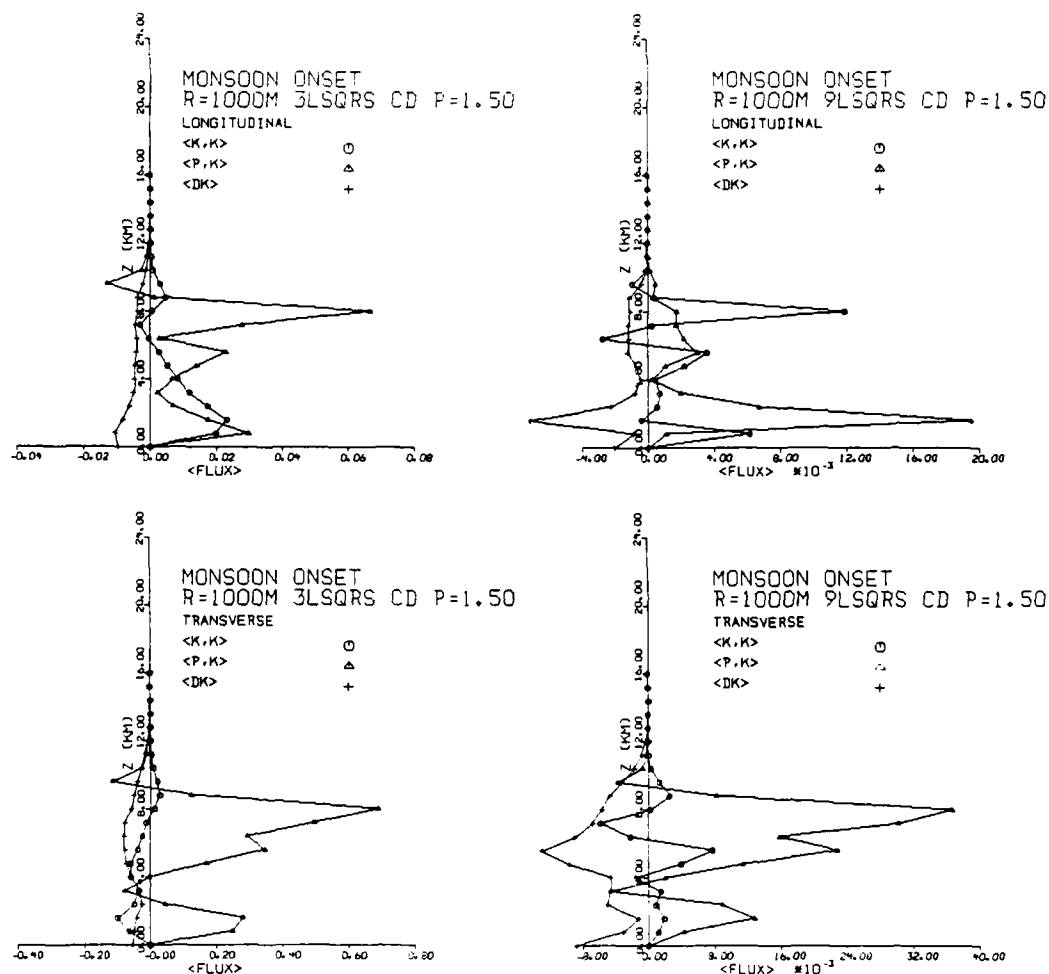
Fig. 7.25 Longitudinal and Transverse Mode Energy Transfers (3rd & 9th Order)
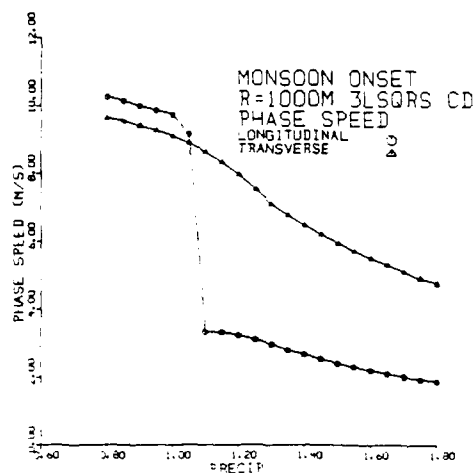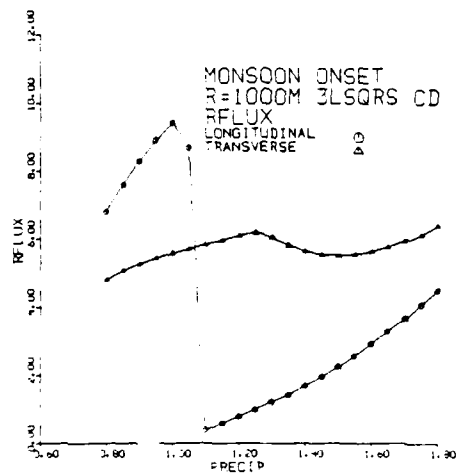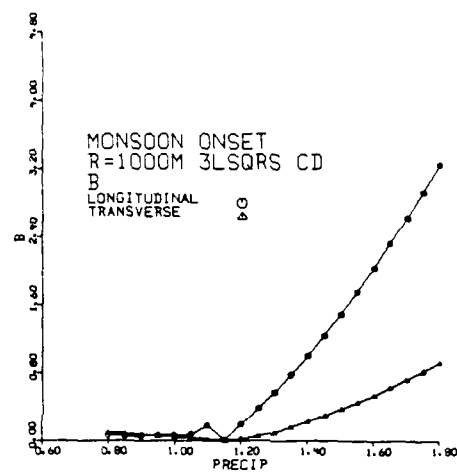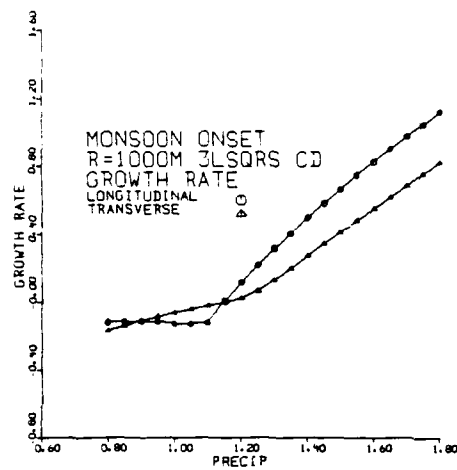
**Fig. 7.26 Longitudinal and Transverse Mode
Behavior as f(P)**

f. Grossman Convective Composite

Another base state studied where the wind was not allowed to turn with height is the Grossman convective composite developed by Grossman and Durran (1984). The determination of this composite sounding was discussed in Chapter VI. The sounding's θ_e profile is relatively similar to the Grossman stable θ_e profile with the exception that it does not possess the strong θ_e minimum of the stable composite near 3.2 km. A cursory glance at the mixing ratio distribution reveals an 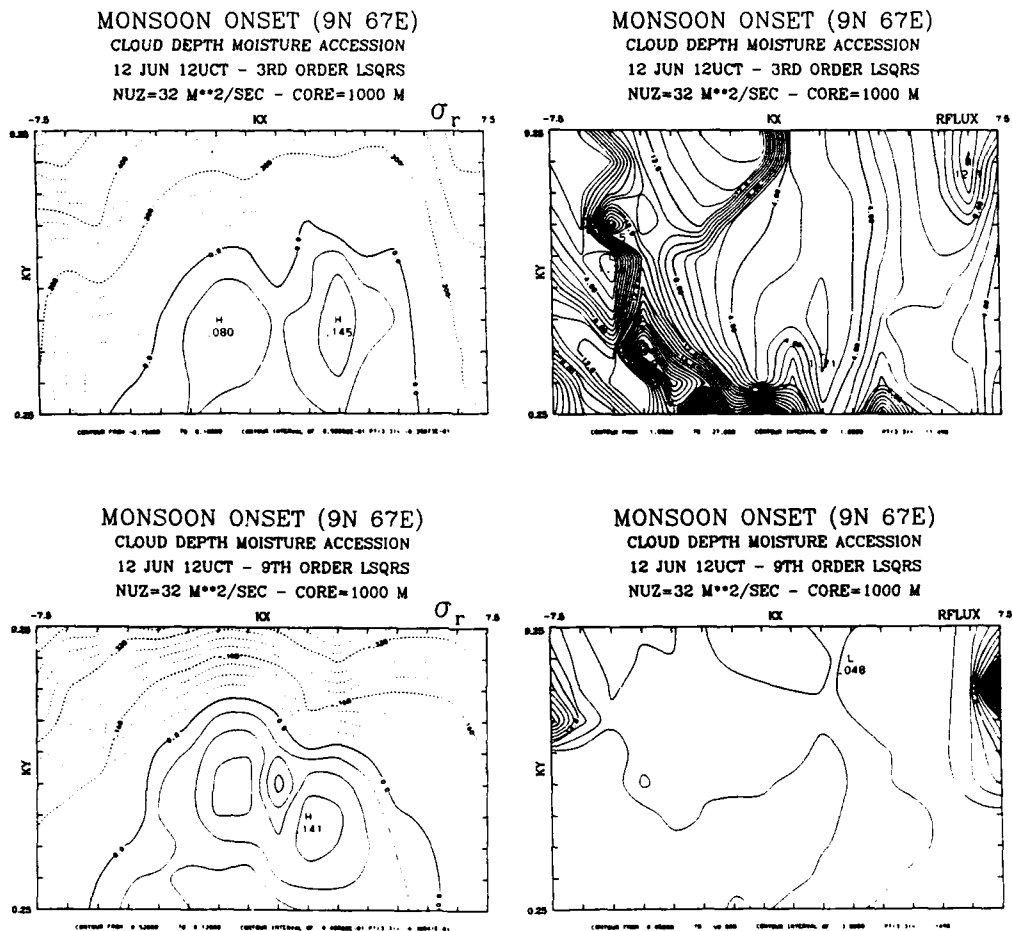excess of 1 - 2 g/kg of vapor for the convective sounding versus the stable sounding between 2.8 and 8.0 km. The moisture differential may be crucial to facilitating deeper convection. Both the steady state and time dependent cloud models show deeper convection is favored (Fig. 7.27). However, growth above the freezing level does not begin until about 30 minutes into the numerical integration.

Examining Table 7.5, an immediate conclusion is that the combinations producing a dominant longitudinal mode are associated with a 9th order fit and 1000 m core radius. Also, all longitudinal modes are associated with CD accession except for one case. However, this one case is a very weak mode (e.f. time = 688.4 min). Changing the vertical viscosity coefficient between 10 - 40 m**2/s does not alter the orientation angle significantly but increases the e.f. time by 110 min. and increases the band spacing by about 20 km. The transverse mode, on the other hand, is either associated with more shallow

convection (500 m) or deeper convection (1000 m) and BL mois-
ture accession. In no instance was there a longitudinal mode
associated with 500 m cores as was the case with the Grossman
stable composite. This comparison, then, contradicts the
notion that more shallow clouds are likely to produce a longi-
tudinal mode for any given base state. A longitudinal mode may
result from deeper convection while more shallow modes will
favor the transverse mode for a give precipitation efficiency.
However, in this instance, the longitudinal mode possesses a B
< 1.0.

Examining now the eigenfunctions for the longitudinal CD
mode (R=1000 m), two maxima appear -- one near 3.2 km and
another around 11.2 km (Fig. 7.28). Here, the W and Θ fields
are 90° out-of-phase while the W and Z fields are ~180° out-
of-phase. Also, the WU flux is primarily confined to the lower
troposphere with the strongest values observed ~3.2 km. The
temperature vertical transport pattern is somewhat deeper with
the maximum transport occurring at 4.8 km. For a more
transverse dominant mode (albeit smoother wind profile), the
primary maxima are located higher in the troposphere. Also,
the strongest vertical transports of U are now located at 7.2
km with a weak secondary maximum at 2.4 km (Fig. 7.29).

The largest mean eigenfunctions associated with the dom-
inant modes show a preference for the entire spectrum of N-S
bands. The primary exceptions to this rule are the U and V
components. The U component maximum values favor noticeably

the longer wavelength E-W modes. The strongest V perturbations are associated with NW-SE (NE-SW) bands (Fig. 7.31).

The behavior of dominant longitudinal and transverse modes as the precipitation efficiency is increased displays critical points and jump behavior as in the previous base states. However, the critical points for the Grossman convective base state are considerably higher for both the longitudinal and transverse bands than for those of the Grossman stable base state (1.30, 1.35 versus .80,.95). In addition to examining the flux Richardson number ratio, the real part of both correlation spectra are plotted for both longitudinal and transverse modes (Fig. 7.32). For the longitudinal mode, the Rflux jump at 1.30 is due to a drop in $\langle P,K'\rangle$ and a corresponding increase in $\langle \bar{K},K'\rangle$. Correspondingly, the flux Richardson number jump at 1.35 in the transverse mode is due to a correspondingly large drop in $\langle \bar{K},K'\rangle$ to slightly negative values and a corresponding increase in $\langle P,K'\rangle$.

It is interesting to examine the vertical profiles of the secondary flow energy conversion terms (real part of the correlation spectra) on both sides of the critical point (Fig. 7.30). For the longitudinal mode, it is evident that the $\langle P,K'\rangle$ term at P=1.2 dominates the $\langle \bar{K},K'\rangle$ term while at P=1.5, $\langle \bar{K},K'\rangle$ is equal to or greater than $\langle P,K'\rangle$ throughout the depth of the fluid. Conversely for the transverse mode, the $\langle \bar{K},K'\rangle$ term dominates (at least in the positive sense) throughout the entire depth while at P= 1.50, $\langle \bar{K},K'\rangle$ is weakly negative or

subordinate to $\langle P,K'\rangle$ throughout the depth. These plots provide further support for the conclusion reached using the vertically-integrated correlation spectra which define the flux Richardson number --i.e., there is a marked change in the energy transfer behavior on either side of the critical point.

TABLE 7.5   GROSSMAN CONVECTIVE COMPOSITE

NUZ	MA	R	LSQ	SHREPS	DESCR	MODE	DIFF	LMAX	EFTIME
9.1	BL	500	3	90	Transv.	19.7	70.3	27.0	238.7
9.1	BL	500	9	90	NW	132.7	57.3	24.1	74.9
22.1	CD	1000	3	90	NW	42.0	48.0	29.9	97.9
22.1	CD	1000	9	90	Long.	81.3	8.7	30.6	112.4
40.0	CD	1000	9	90	Long.	102.5	12.5	43.6	183.8
10.0	CD	1000	9	90	Long.	84.6	5.4	19.1	74.0
22.1	BL	1000	9	90	Supp.	--	--	--	
22.1	BL	1000	3	90	Supp.	--	--	--	
9.1	CD	500	9	90	NW	42.9	47.1	21.0	48.7
9.1	CD	500	9	90	Transv.	12.8	77.2	17.8	63.2
22.1	CD	1000*	9	90	Long	98.7	8.7	30.6	69.9
22.1	CD	1000*	3	90	NW	56.3	33.7	37.2	63.4
22.1	CD	1000**	3	90	NW	39.8	50.2	51.5	312.6
22.1	BL	1000**	9	90	Supp.	--	--	--	
22.1	BL	1000*	9	90	Supp.	--	--	--	
22.1	BL	1000*	3	90	Supp.	--	--	--	
22.1	BL	1000**	9	90	Long.	102.5	12.5	43.6	688.4
22.1	CD	1000***	9	90	Long.	93.9	3.9	13.8	16.6
22.1	CD	1000	1	90	NW	56.3	33.7	37.2	

* P=1.2   ** P=0.8   *** P=1.5

CD=cloud depth moisture accession

BL=boundary layer moisture accession

NUZ=vertical eddy diffusion coefficient (m**2/s)

SHREPS=cloud layer shear orientation in k domain

DIFF=angle magnituded between MODE and SHREPS

LMAX=band spacing in km.

EFTIME=reciprocal of mode growth rate in minutes

R=cloud radius in meters

LSQ=order of fitted wind polynomial
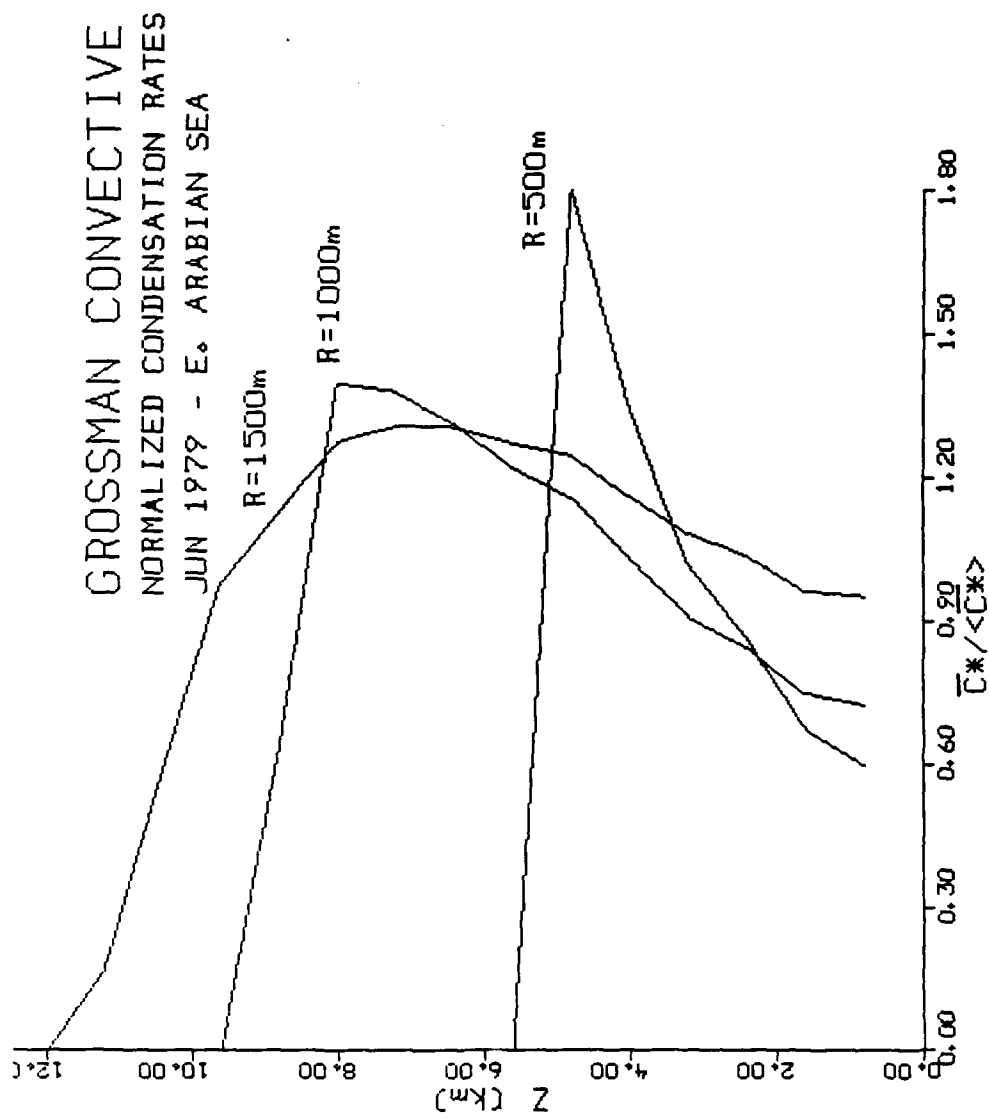
Fig. 7.27 Grossman Convective Heating Profiles

W EIGENFUNCTION
L=30.6 KM -- N

T EIGENFUNCTION
L=30.6 KM -- N

Z EIGENFUNCTION
L=30.6 KM -- N

WU EIGENFUNCTION
L=30.6 KM -- N

Fig. 7.28 Longitudinal/9th Order/P=1.0/CD/R=1000
Eigenfunctions

W EIGENFUNCTION
L=29.9 KM -- NE

T EIGENFUNCTION
L=29.9 KM -- NE

Z EIGENFUNCTION
L=29.9 KM -- NE

WU EIGENFUNCTION
L=29.9 KM -- NE
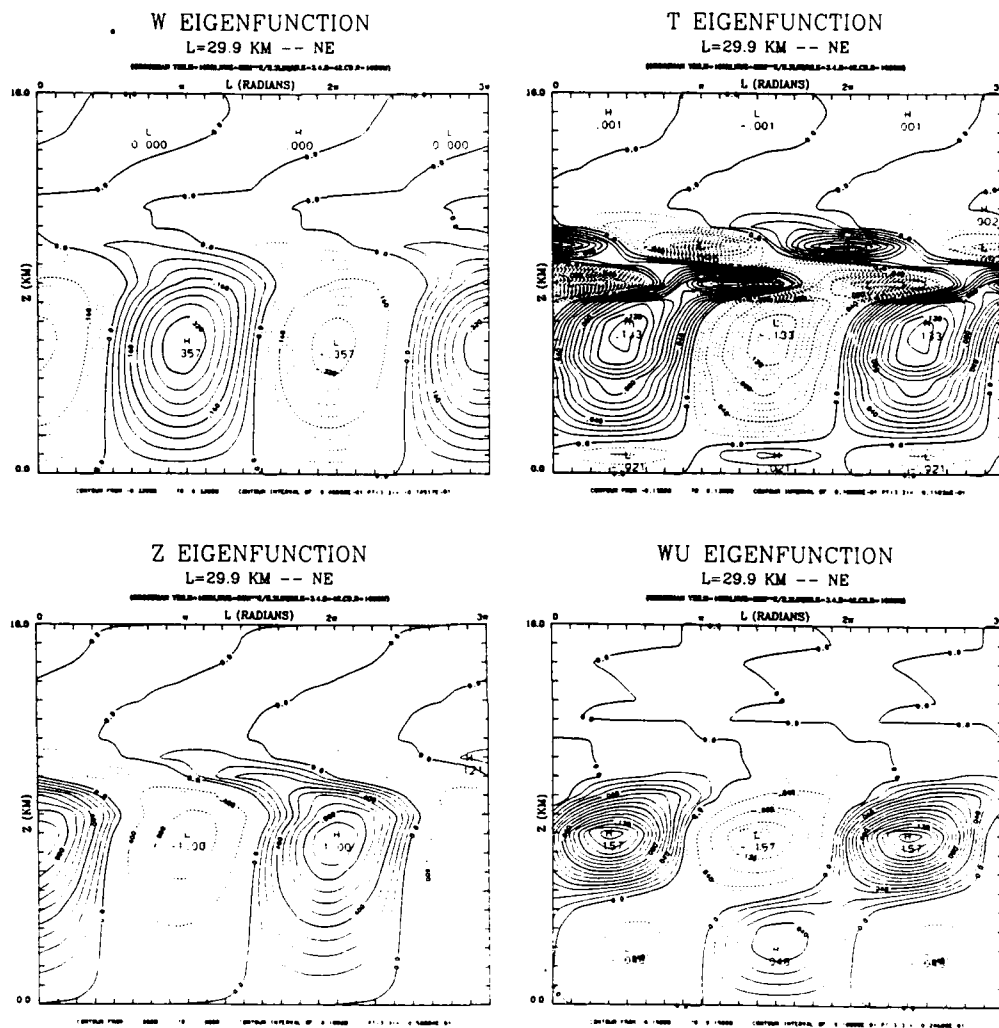
Fig. 7.29   Transverse/3rd Order/P=1.0/CD/R=1000
Eigenfunctions
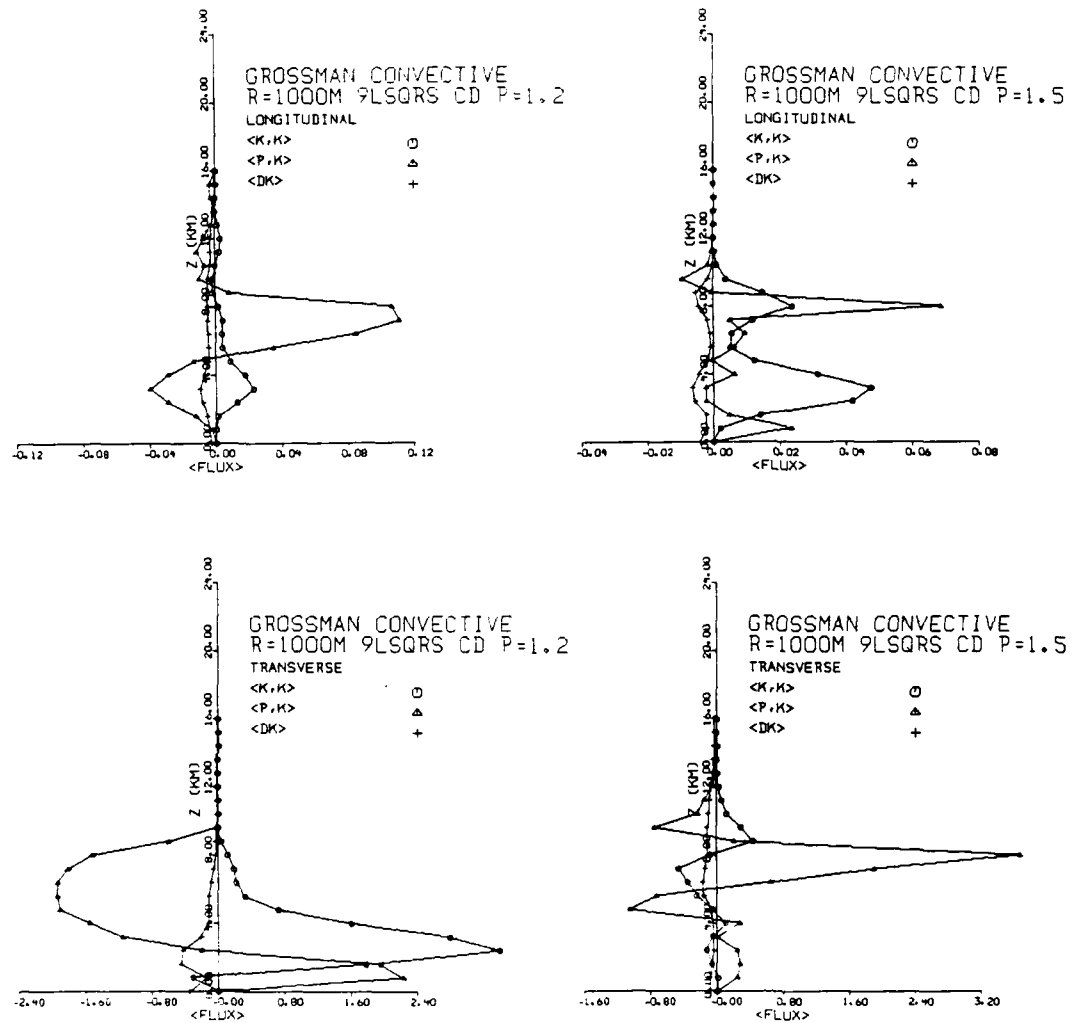
Fig. 7.30 Longitudinal and Transverse Mode Energy Transfers (P=1.20, P=1.50)

GROSSMAN COMPOSITE
CLOUD DEPTH MOISTURE ACCESSION
JUN 1979 - 9TH ORDER LSQRS - P=1 5
NUZ=22 M**2/SEC - CORE=1000 M

GROSSMAN COMPOSITE
CLOUD DEPTH MOISTURE ACCESSION
JUN 1979 - 9TH ORDER LSQRS - P=1 5
NUZ=22 M**2/SEC - CORE=1000 M

GROSSMAN COMPOSITE
CLOUD DEPTH MOISTURE ACCESSION
JUN 1979 - 9TH ORDER LSQRS - P=1 5
NUZ=22 M**2/SEC - CORE=1000 M

Fig. 7.31 Dominant Modes' Mean Eigenfunction
Amplitudes

Fig. 7.32 Longitudinal and Transverse Mode
Behavior as f(P)

g. Eastern Arabian Sea

The eastern Arabian Sea base state is characterized by deep convective instability through 6 km with convective stability above. This is the deepest convective instability of the base states examined in this study. Unlike the other four base states examined, the results of the 1DSS and 1DTD cloud models tend to disagree. The 1DSS results (see Table 6.1, Chapter VI and Fig 7.33) suggest deep convection is facilitated by this sounding, even more so for the smaller core radii than the Grossman convective composite. However, the 1DTD model shows no propensity for growth at the upper levels (Chapter VI fig. 6.5). There is a "rain-out" during the first 20 minutes for levels below 3 km. The lack of growth in the 1DTD model above the freezing level may be attributed to lower specific humidities between 4 and 8 km relative to the Grossman convective base state. When the humidity was increased by 1 to 2 g/kg between 6.4 and 8.0 km, vigorous growth developed at and above the freezing level.
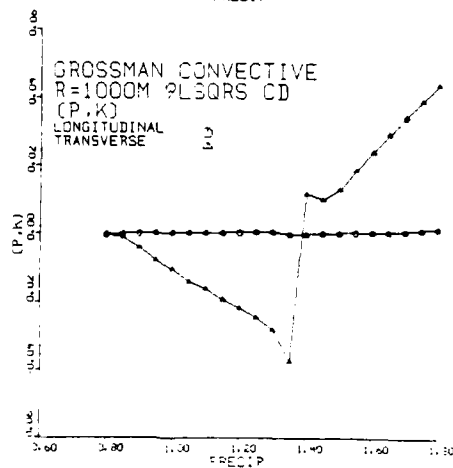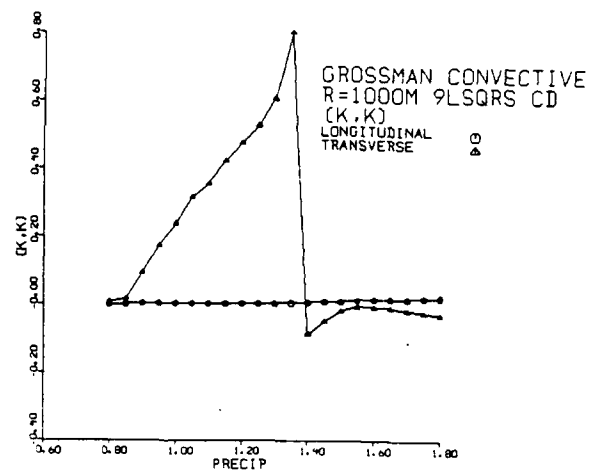
The base state u, v wind field for the model shows the characteristic bimodal u and the S-N turning of the wind field with a 4 km high v maximum. The 9th order fit retains both the u and v maxima. However, the 3rd order fit greatly smoothes the field; especially the u component. The effect of the different fits will be shown subsequently in the discussion.

Table 7.6 suggests that longitudinal modes are favored by

cloud depth moisture accession and 9th order fits while the purely transverse modes are associated with 3rd order fits and CD moisture accession. However, for the 9th order fits and P< 1.2, all modes are propagating. For 3rd order fits with CD moisture accession and P=1.0, a stationary mode (although not necessarily dominant) is observed, however, along with a non-dispersive phase field in the vicinity of the stationary modes. For a linear fit even with a 1500 m radius and P=1.0, a dominant stationary mode develops. This suggests that for the east Arabian Sea base states where wind turns strongly with height, the smoothness of the profile facilitates a longitudinal mode dominance.

For augmented moisture, strong longitudinal modes develop for 1st and 3rd order fits while only weak stationary modes develop for the 9th order fit. While a 9th order fit does induce stationarity as indicated in the B field, the longitudinal mode here is not the dominant mode. It is interesting to compare the difference between the BL and CD accession methods for the 3rd order fit (Figs. 7.34 and 7.35). For BL accession, the σ_r field is polarized and weaker with a weakly dominant stationary mode. The phase speed field is virtually non-dispersive with the zero speed line coincident with the longitudinal mode axis. The cloud depth moisture accession produces stronger growth with a non-polarized growth field and a prominent stationary mode. However, the phase speed lines exhibit less non-dispersion especially in the < 90° domain. In both

instances, the flux Richardson number exhibits a strong minimum in and around the longitudinal modes. For a 1st order fit and CD accession, the growth rate field bears some resemblance to the 3rd order results except that it tends to be a little weaker on the short wavelength fringes. Overall, the phase speed field is less non-dispersive for the linear fit when compared to the 3rd order fits.

Examining next the distribution of the mean vertically-integrated eigenfunctions associated with the dominant modes in the k domain, the strongest vertical velocities and temperature perturbations are associated with the NNW-SSE modes (Fig. 7.36). These are in effect the transverse modes. The Z field though does not show this preference. The U field, as was the case, with the Ogura wind favored somewhat the E-W modes especially at the longer wavelengths. Similar to W, the WU correlation spectrum favored longer wavelength NW-SE modes.

The vertical cross-section of eigenfunctions associated with a propagating longitudinal mode and a stationary longitudinal mode for the E.A.S. base state are compared (Figs. 7.37 and 7.38). The propagating mode associated with no precipitation augmentation (P=1.0) shows poor phase agreement between W and T with two vertically-separated maxima of Z --one near 2.4 km and one near 8 km. A similar bi-modal distribution of U and WU is also observed. For the augmented precipitation case (P=1.5) associated with the stationary longitudinal mode, the vertical velocity and temperature eigenfunctions are in phase

with vertical velocity maxima at 5.6 km and temperature pertur-
bation maxima at cloud base (0.8 km) and 5.6 and 8.8 km. The Z
eigenfunctions are no longer bi-modal but display a strong max-
imum at 6.4 km. Likewise, the U fields as well as WU and WV
display a single strong maximum near 6.4 km. Perhaps, the most
striking difference between the propagating and stationary
eigenfunction cross-sections is the erectness and lack of
"tilt" in the moisture-augmented stationary patterns.

The behavior of selected dominant longitudinal and
transverse band configurations display a similar jump confi-
guration as in the previous discussions (Fig. 7.39). However,
there tends to be little or no lag between the longitudinal and
transverse modes. Furthermore, the critical or jump point
occurs at a lower threshold than for the other deep convection
base states. Here, that threshold is about P=0.95 (b=.05).
This is not only confirmed by the amplitude of the flux
Richardson number and phase speed terms but also in the real
part of the Rflux numerator and denominator.

The secondary energy transfers to the right of the jump
(b=-.20) for both longitudinal and transverse dominant modes
are shown. Relatively speaking, $\langle P,K' \rangle$ dominates the other
terms ($\langle \overline{K},K' \rangle$, $\langle DK' \rangle$) for the transverse mode when compared
with the longitudinal mode while it is generally negative
throughout the depth for the transverse mode. This is con-
sistent with the previous findings for deep convective base
states.

A likely question to be raised is whether the jump observed is due to the numerical method or due to the analytical formulation of the governing equations. As mentioned earlier in Chapter V, a second method for obtaining all the eigenvalues and eigenvectors for the complex eigenvalue problem is the QZ algorithm. The QZ algorithm, unlike the LZ algorithm which used complex operands, employs programmed complex arithmetic on real operands. Using both methods for particular modes associated with the EAS base states produced virtually identical results as P was varied. This suggests that the observed jump behavior in the eigenvalues and eigenvectors is a result of the analytical formulation rather than the particular numerical method used.

Another interesting question is what response might be generated when the eastern Arabian Sea thermodynamic base state is paired with the Ogura E-W wind profile. The results resemble in part those of the Grossman convective composite paired with the same E-W profile. However, the stationary longitudinal component increases in dominance and stationarity as the cloud depth is increased for a 9th order wind profile (Fig. 7.40). This is not the case for the other fit for the same EAS base state where a stationary but not dominant longitudinal mode instead develops as the cloud depth or core radius is increased. Furthermore, this result indicates that in special cases (such as with an E-W low level jet), increasing the cloud depth or vertical heating distribution may enhance the develop-

ment of a stationary longitudinal mode.

TABLE 7.6   EASTERN ARABIAN SEA

NUZ	MA	R	LSQ	SHREPS	DESCR	MODE	DIFF	LMAX	EFTIME
39.4	CD	1000	3	118.1	Transv.	19.7	98.4	27.0	46.8
12.4	CD	500	9	106.7	Long.	83.2	23.5	23.5	24.6
76.7	CD	1500	9	101.7	Long.	102.5	0.8	43.6	42.7
39.4	CD	1000	1	117.1	NW	65.2	51.9	28.1	52.5
39.4	BL	1000	1	117.1	Supp.	--	--	--	
12.4	BL	500	3	117.0	NW	70.6	46.4	22.3	84.4
100.	CD	1000	9	102.7	Long.	102.5	.2	43.6	44.1
76.7	BL	1500	9	101.7	SW	138.0	36.3	29.9	48.8
12.4	BL	500	9	106.7	Long.	115.5	8.8	17.3	22.8
39.4	BL	1000	9	102.7	Long.	127.6	24.9	24.5	32.9
76.7	BL	1500	3	118.1	Supp.	--	--	--	
39.4	BL	1000	3	118.1	Supp.	--	--	--	
76.7	CD	1500	3	118.1	Transv.	4.1	114.0	28.7	38.9
12.4	CD	500	3	117.0	Transv.	42.9	74.1	21.0	24.1
39.4	CD	1000	9	102.7	Long.	114.8	12.1	28.1	29.1
39.4	BL	1000*	3	118.1	Long.	129.5	11.4	18.3	21.5
39.4	CD	1000*	3	118.1	Long.	123.7	5.6	15.9	7.4
39.4	CD	1000*	1	117.1	Long.	115.5	1.6	17.3	7.4
39.4	CD	1000**	9	102.7	NW	59.5	43.2	20.4	18.9
76.7	CD	1500	1	117.1	Long.	114.8	2.3	28.1	38.4
39.4	CD	1000***	9	102.7	NW	69.3	33.4	10.2	17.9

* P=1.5   ** P=1.2   *** Isotropic Diffusion

CD=cloud depth moisture accession

BL=boundary layer moisture accession

NUZ=vertical eddy diffusion coefficient (m**2/s)

SHREPS=cloud layer shear orientation in k domain

DIFF=angle between MODE and SHREPS

LMAX=band spacing in km.

EFTIME=reciprocal of mode growth rate in minutes

R=cloud radius in meters

LSQ=order of fitted wind ploynomial

Fig. 7.33 Eastern Arabian Sea Convective Heating Profiles

EASTERN ARABIAN SEA
CLOUD DEPTH MOISTURE ACCESSION
20 JUN 06UCT – 3RD ORDER LSQRS – P=1.5
NUZ=39 M**2/SEC – CORE=1000 M

EASTERN ARABIAN SEA
CLOUD DEPTH MOISTURE ACCESSION
20 JUN 06UCT – 3RD ORDER LSQRS – P=1.5
NUZ=39 M**2/SEC – CORE=1000 M

EASTERN ARABIAN SEA
CLOUD DEPTH MOISTURE ACCESSION
20 JUN 06UCT – 3RD ORDER LSQRS – P=1.5
NUZ=39 M**2/SEC – CORE=1000 M

EASTERN ARABIAN SEA
CLOUD DEPTH MOISTURE ACCESSION
20 JUN 06UCT – 3RD ORDER LSQRS – P=1.5
NUZ=39 M**2/SEC – CORE=1000 M

Fig. 7.34 Growth Rate, B, Rflux, Phase Speed/3rd Order/
CD/P=1.5/R=1000

EASTERN ARABIAN SEA
BL MOISTURE ACCESSION
20 JUN 06UCT – 3RD ORDER LSQRS – P=1 5
NUZ=39 M**2/SEC – CORE=1000 M

EASTERN ARABIAN SEA
BL MOISTURE ACCESSION
20 JUN 06UCT – 3RD ORDER LSQRS – P=1 5
NUZ=39 M**2/SEC – CORE=1000 M

EASTERN ARABIAN SEA
BL MOISTURE ACCESSION
20 JUN 06UCT – 3RD ORDER LSQRS – P=1 5
NUZ=39 M**2/SEC – CORE=1000 M

EASTERN ARABIAN SEA
BL MOISTURE ACCESSION
20 JUN 06UCT – 3RD ORDER LSQRS – P=1 5
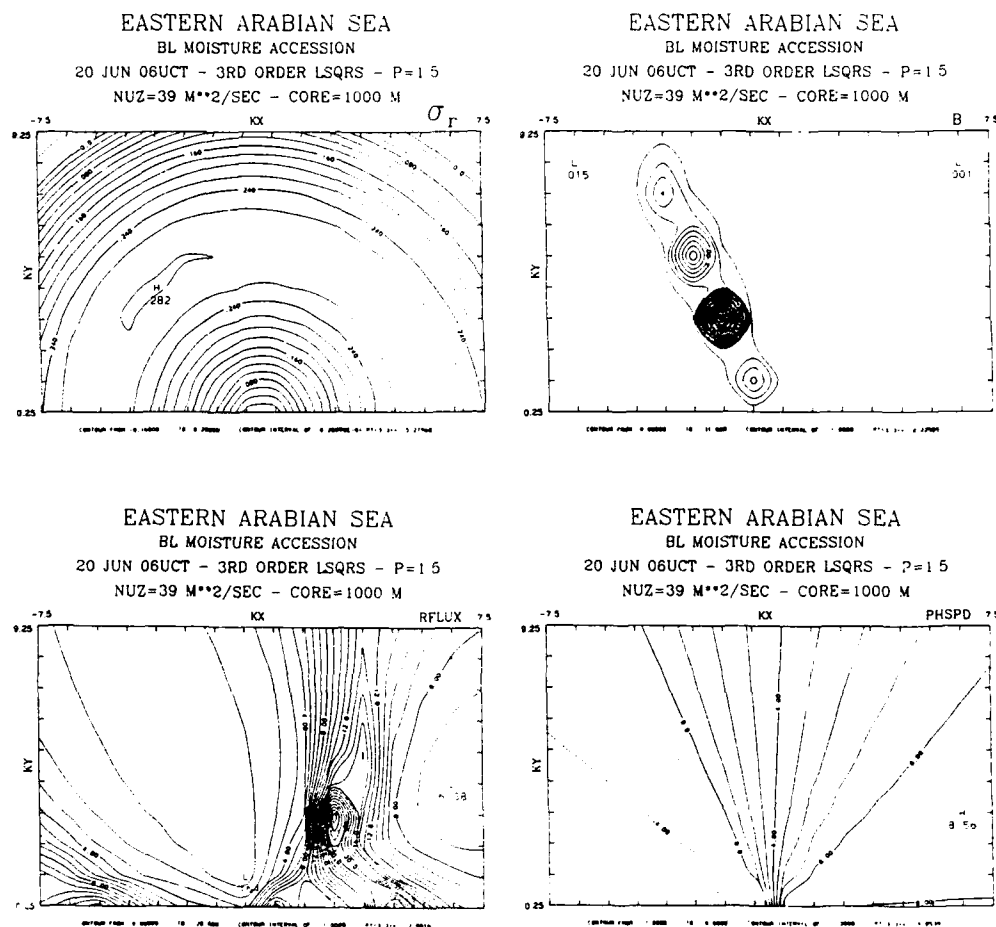NUZ=39 M**2/SEC – CORE=1000 M

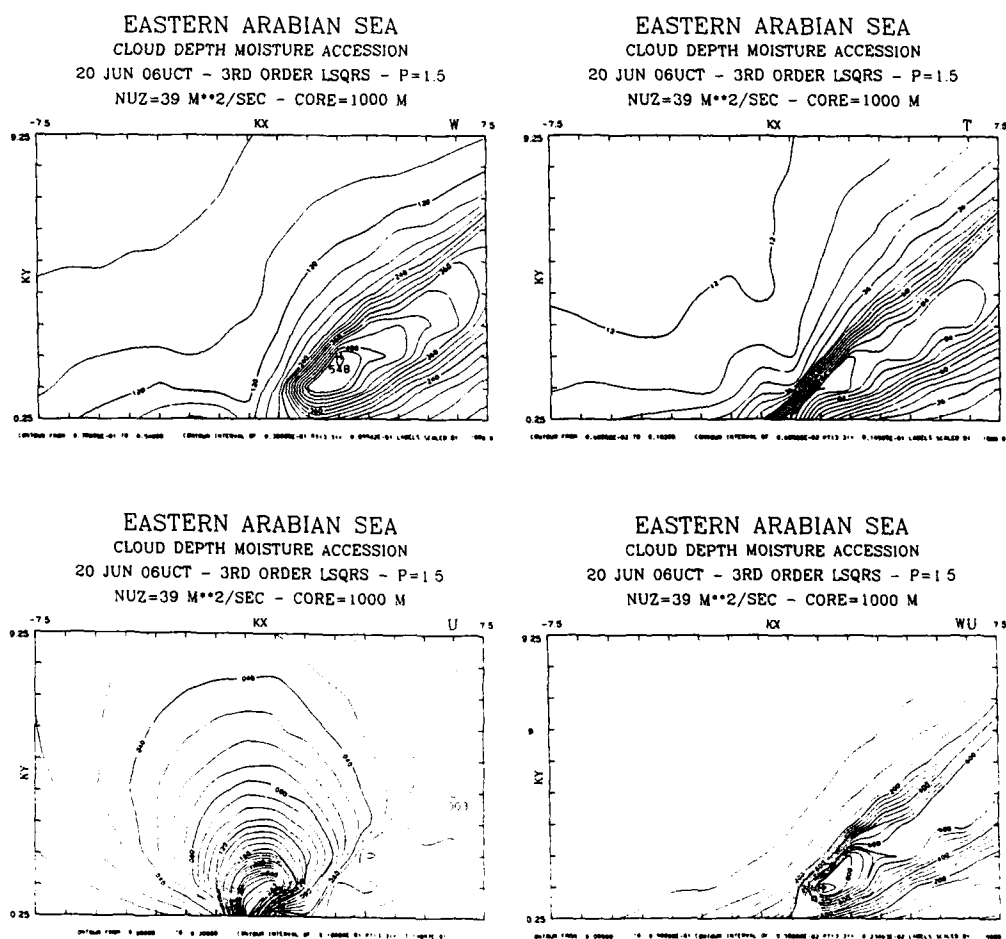Fig. 7.35   Growth Rate, B, Rflux, and Phase Speed/3rd
Order/ BL/P=1.5/R=1000

173

Fig. 7.36 Dominant Modes' Mean Eigenfunction Amplitudes

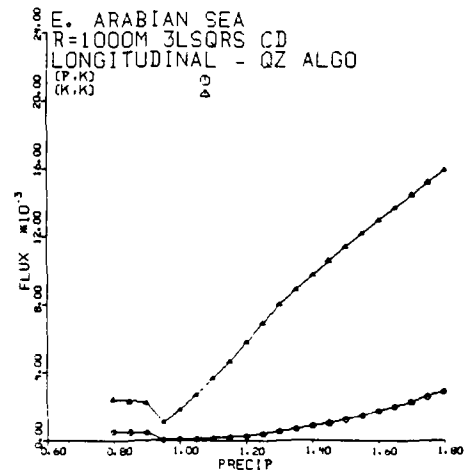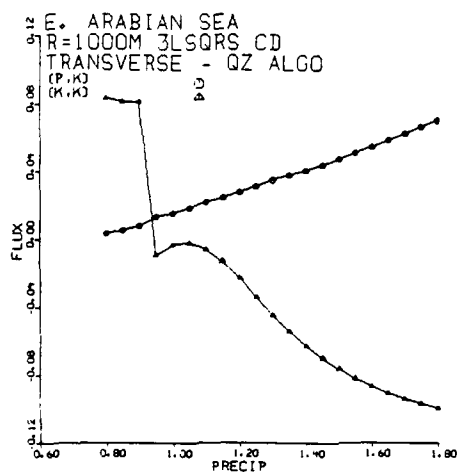Fig. 7.37 Longitudinal/9th Order/P=1.0/CD/R=1000
Eigenfunctions

Fig. 7.38 Longitudinal/3rd Order/P=1.5/CD/R=1000
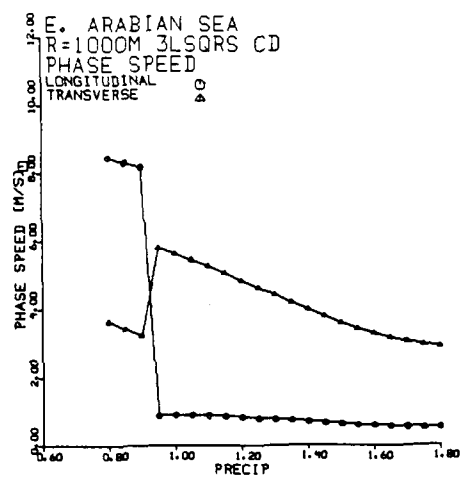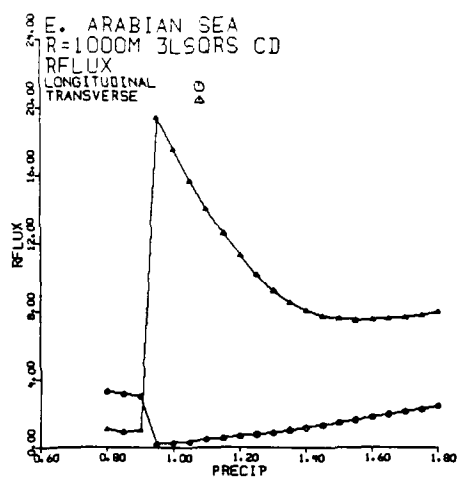Eigenfunctions

Fig. 7.39 Longitudinal and Transverse Mode
Behavior as f(P)

132

EASTERN ARABIAN SEA (E-W WIND)
CLOUD DEPTH MOISTURE ACCESSION
20 JUN 06UCT - 9TH ORDER LSQRS
NUZ=12 M**2/SEC - CORE=500 M
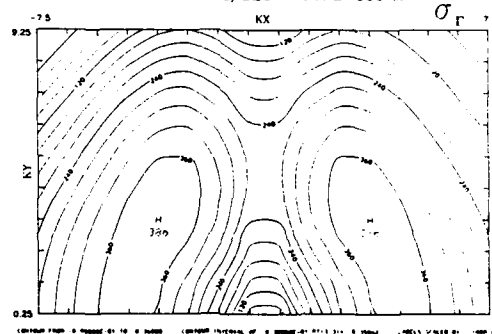
EASTERN ARABIAN SEA (E-W WIND)
CLOUD DEPTH MOISTURE ACCESSION
20 JUN 06UCT - 9TH ORDER LSQRS
NUZ=39 M**2/SEC - CORE=1000 M
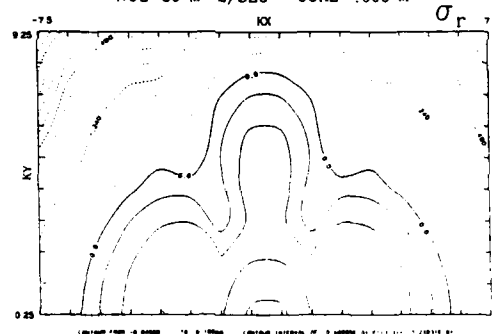
EASTERN ARABIAN SEA (E-W WIND)
CLOUD DEPTH MOISTURE ACCESSION
20 JUN 06UCT - 9TH ORDER LSQRS
NUZ=77 M**2/SEC - CORE=1500 M

Fig. 7.40 EAS/Ogura Wind Growth Rate:
R = 500,1000,1500m P = 1.0/CD/9th Order

h. Inclusion of Effects of Sensible Heating by Clouds on the
    Environment

While the dominant contribution to the vertical distribu-
tion of convective heating is due to condensational heating or
release of latent heat, recent studies have shown that the
transport of eddy fluxes of sensible heat within a cloud
through updrafts or downdrafts is non-negligible for deep con-
vection and should probably not be ignored in a complete param-
eterization scheme (Kuo and Anthes, 1984; Kuo and Raymond,
1980). Accordingly several base states used in the previous
runs were selected for inclusion of sensible heating in addi-
tion to the condensational heating in determining the vertical
heating profile. The effects on the solutions due to inclusion
of sensible heating will be discussed by comparison of results
with and without sensible heating. The governing equations and
their implementation in the cumulus parameterization scheme
were shown previously in Chapter IV.

First, it is essential to view how the normalized vertical
profiles are altered by including the sensible heating. One
general feature observed in the attached diagrams is that the
sensible heating tends to cool the lowest layers and warm the
upper layers (Figs. 7.41 - 7.43). In general, the sensible
heat transports are most significant in the upper third of the
cloud layer. Also, their contributions to the total heating
rate is greatest for the larger core radii (1500 m). While the
condensational heating rate is normally dominant, the sensible
heating rate exceeds the condensational heating rate for the

eastern Arabian Sea (20 June 06UTC) base state near cloud top for the 1000 m and 1500 m core radii. The net effect, then of inclusion of sensible heating, is to shift a greater fraction of the total convective heating to the upper half of the cloud layer.

How are the solutions altered by including sensible heat in the parameterization scheme? One dramatic effect for the Grossman stable composite (R = 500 m) with inclusion of the low level jet is to destroy the dominant longitudinal stationary mode (Fig. 7.45). Not only are the dominant modes shifted from longitudinal to transverse but the bands acquire a propagating character. Even increasing the precipitation efficiency to P= 1.2 fails to establish a dominant longitudinal mode (although evidence of longitudinal stationarity becomes apparent in the B and Rflux fields). Ironically, the low order (3rd order fit) becomes more likely to produce a longitudinal stationary mode (Fig. 7.44). The stationarity becomes very evident in the B and phase speed diagrams. Hence, the sensible heating forces the relatively shallow convective cores to behave more in a similar fashion to the deep convective profiles discussed ear- lier by exhibiting more stationarity in the presence of smoother wind profiles. This is accomplished through shifting a greater portion of the convective heating to the upper cloud layers.

The behavior of the deeper convective base states seem less sensitive to the sensible heating role. For the EAS base

state (9 CD 1000), the sensible heating increases the growth rate slightly but maintains the propagating dominant longitudinal mode. For strong moisture convergence (P=1.5) and smooth wind profile (3 CD 1000 1.5), the stationary longitudinal mode is maintained although the growth rate is cut by 50%. Likewise, the Grossman convective composite (Gross 9 CD 1000 1.0) maintains an essentially longitudinal propagating mode when sensible heat is included as was the case with only condensational heating.

The vertical character of the eigenfunctions is also changed, albeit slightly for deep convection. For the EAS base state with strong moisture augmentation (3 CD 1000 1.5), the sensible heating shifts the vertical velocity maximum height by 1.6 km. Similar responses are noted in the Z, U, and V fields. Also, the divergence magnitude in the upper levels relative to the lower levels is greater for the sensible heat inclusion. Here the U, V, and Z amplitude maxima are located at 8 km while the divergence and perturbation pressure maxima are observed at 9.6 km just beneath cloud base. Also, there is general phase agreement between W and Θ fields as well as the divergence and perturbation pressure fields. For the less deep convection associated with the Grossman stable base state, several subtle differences appear when the sensible heating is introduced. First, the greatest vertical velocity amplitude shifts to the upper part of the cloud layer (3.2 km). Likewise, the strongest/heating cooling amplitudes in the perturbation poten-

tial temperature fields also shift higher. As was seen with the deep convective base state, the divergence amplitude near cloud top increases relative to the amplitudes (of opposite sign) observed at the surface. The correlation quantities also exhibit a similar behavior for the Grossman base state.

How does the inclusion of sensible heat affect the critical point or jump behavior of the model? For the one case examined (Grossman Stable 500 m 9LS BL) the longitudinal jump is greatly delayed when sensible heating is included (from $P=0.85$ to $P=1.15$, $\Delta P=.3$) while the transverse mode jump is more muted when the sensible heating is included (Fig. 7.46). Thus, the inclusion of sensible heat delays the onset of the stationary longitudinal mode and slightly advances the onset of the more transitive mode for this particular base state.

TABLE 7.7   INCLUSION OF SENSIBLE HEAT TRANSPORTS

NUZ	MA	R	LSQ	SHREPS	DESCR	MODE	DIFF	LMAX	EFTIME
100	CD	1000E	9	102.7	Long.	102.5	.2	43.6	31.9
22	CD	1000GC	3	90	NW	42.0	48.0	29.9	59.7
22	CD	1000GC	9	90	Long.	114.8	24.8	28.1	80.1
22	BL	1000GC	3	90	Supp.	--	--	--	
14	BL	500GS	3	90	Supp.	--	--	--	
14	BL	500GS	9	90	Transv.	4.1	85.9	28.7	99.9
22.	BL	1000GC	9	90	Supp.	--	--	--	
22	CD	1000GC*	9	90	Long.	98.7	8.7	30.6	40.2
39	CD	1000E	9	102.7	Long.	98.7	4.0	30.6	21.4
39	CD	1000E*	9	102.7	Transv.	26.6	76.2	20.0	14.3
39	CD	1000E	3	118.1	Long.	98.7	19.3	30.6	37.2
39	CD	1000E*	3	118.1	Long.	120.5	2.4	20.4	15.5
22	CD	1000GS*	3	90	SW	123.7	33.7	15.9	32.7
14	BL	500GS**	9	90	Transv.	3.2	86.8	22.3	62.4
14	BL	500GS**	3	90	Long.	95.4	19.1	19.1	183.7

* P=1.5   ** P=1.2

CD=cloud depth moisture accession

BL=boundary layer moisture accession

NUZ=vertical eddy diffusion coefficient (m**2/s)

SHREPS=cloud layer shear orientation angle in k domain

DIFF=angle magnitude between MODE and SHREPS

LMAX=band spacing in km.

EFTIME=reciprocal of mode growth rate in minutes

R=cloud radius (m) and base state
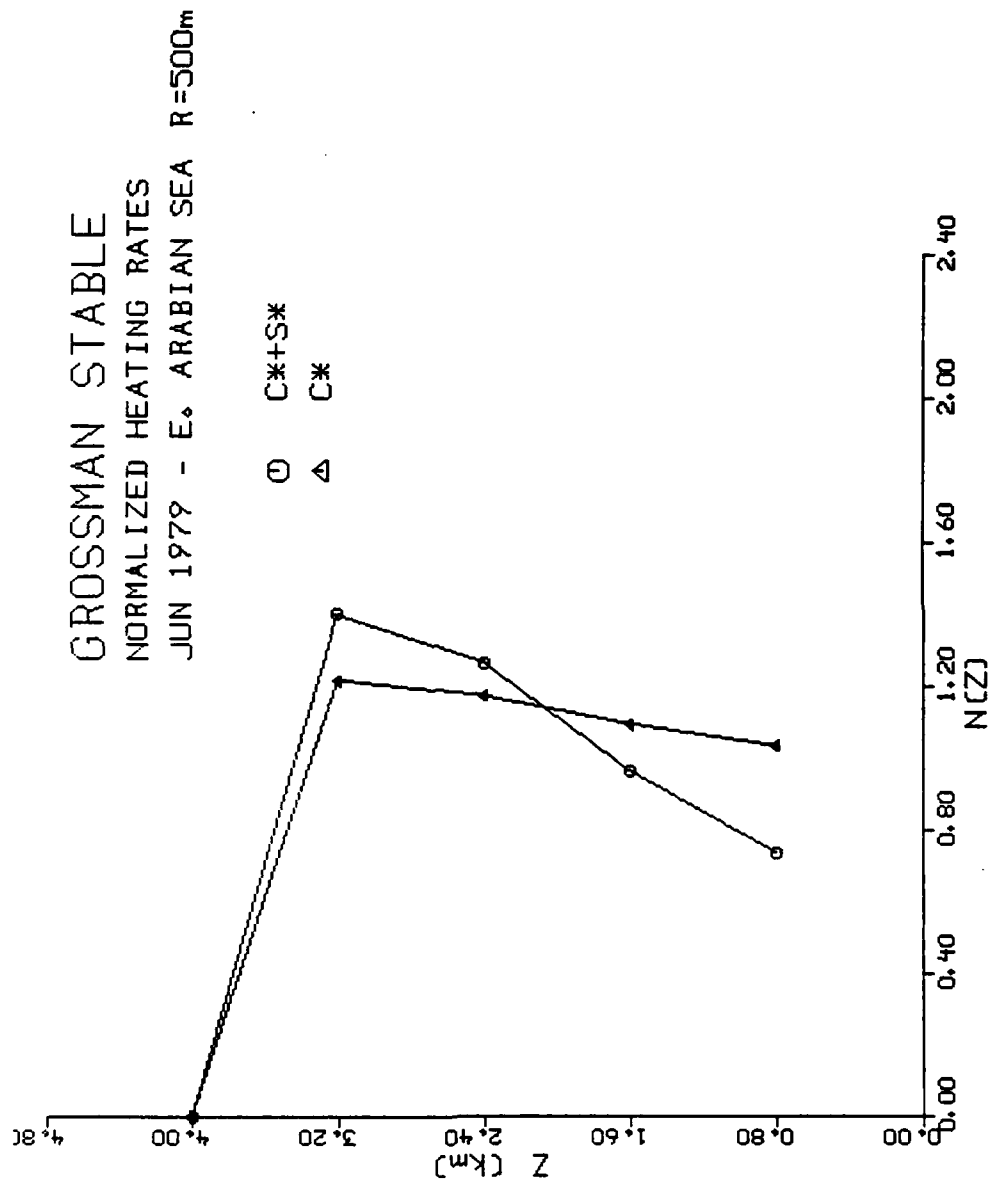
LSQ=order of fitted wind polynomial

188

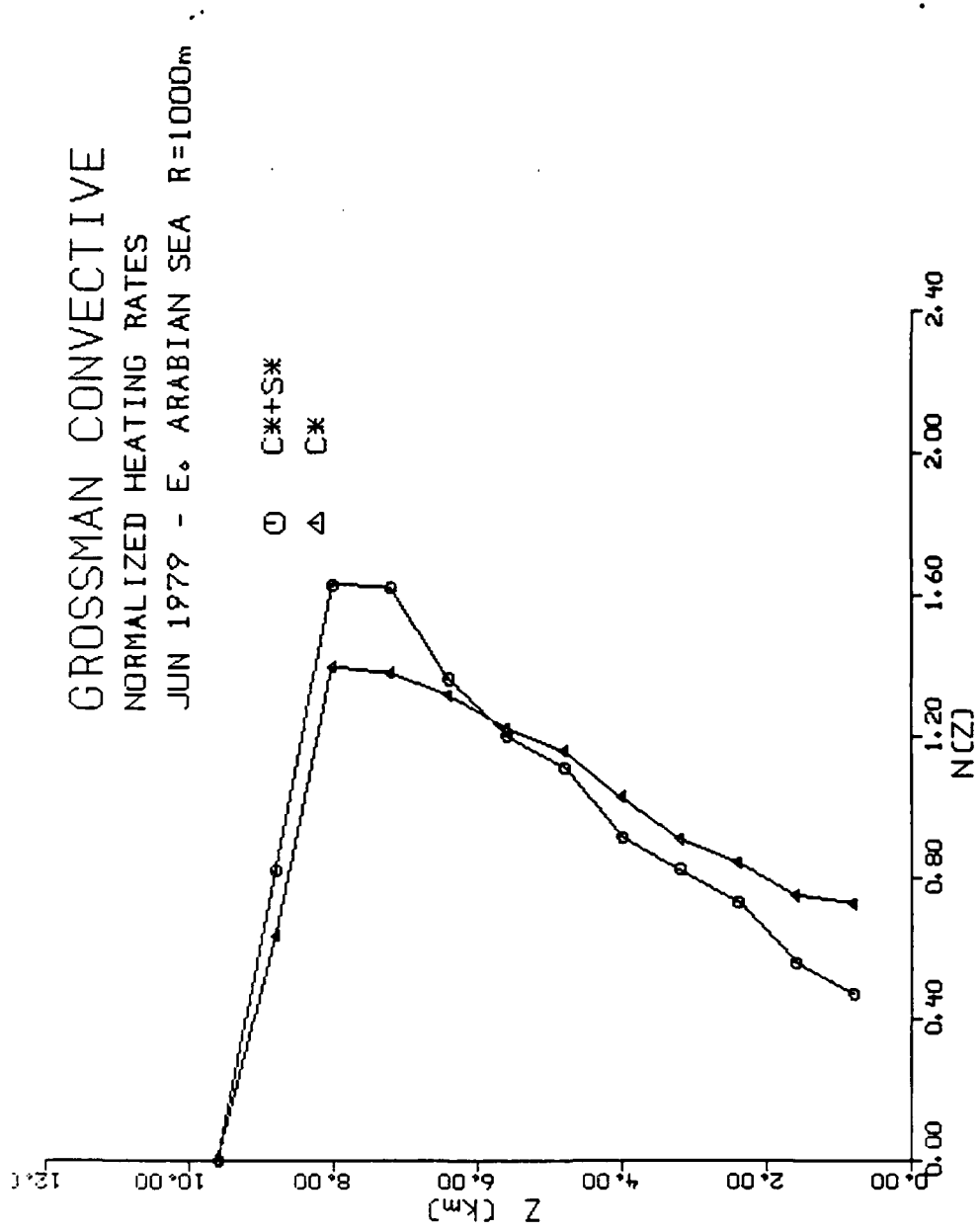Fig. 7.41 Grossman Stable Convective and Total Heating Profiles

189

Fig. 7.42 Grossman Convective and Total Heating
Profiles

190

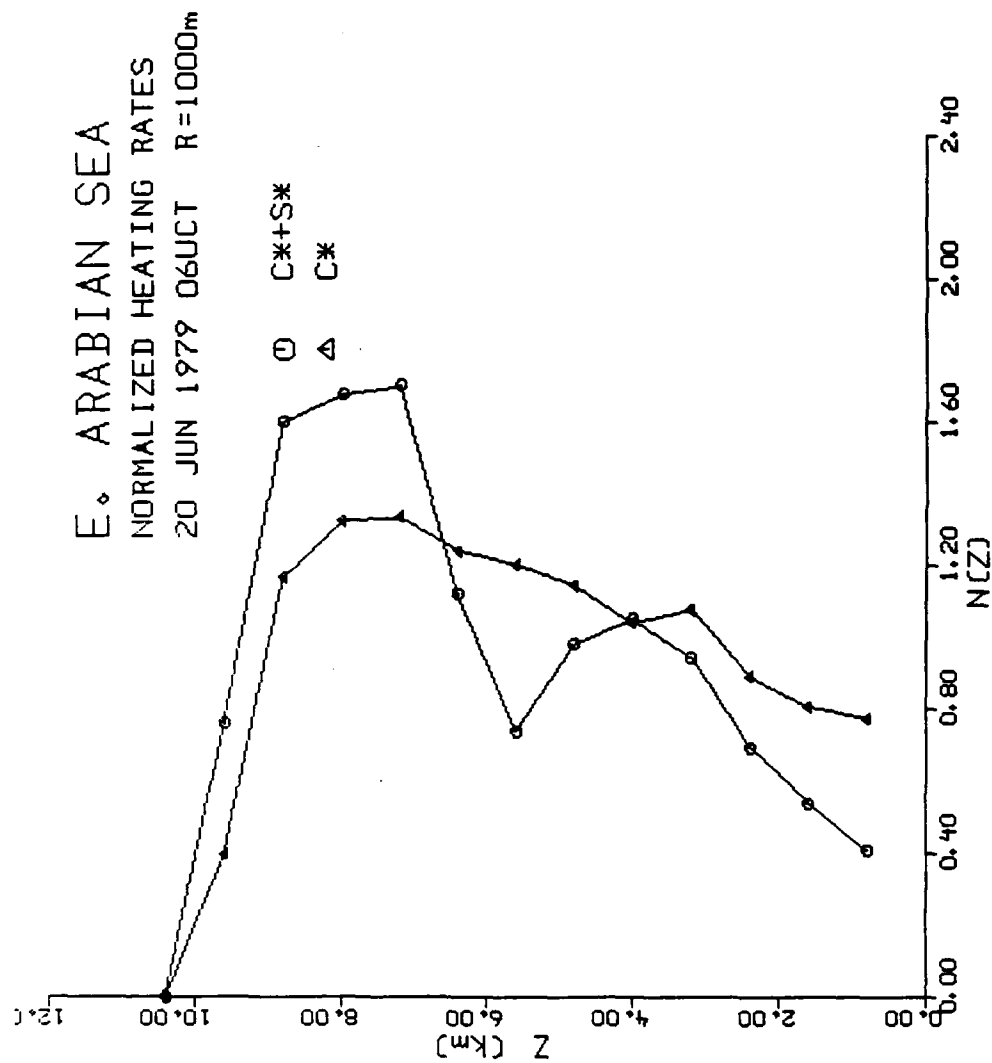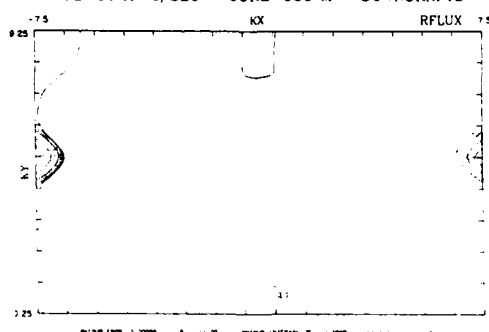Fig. 7.43 Eastern Arabian Sea Convective and Total Heating Profiles

GROSSMAN COMPOSITE (STABLE)
BL MOISTURE ACCESSION
JUN 1979 - 3RD ORDER LSQRS - P=1.2
NUZ=14 M**2/SEC - CORE=500 M - DOWNDRAFTS

σ_r

GROSSMAN COMPOSITE (STABLE)
BL MOISTURE ACCESSION
JUN 1979 - 3RD ORDER LSQRS - P=1.2
NUZ=14 M**2/SEC - CORE=500 M - DOWNDRAFTS

PHSPD

GROSSMAN COMPOSITE (STABLE)
BL MOISTURE ACCESSION
JUN 1979 - 3RD ORDER LSQRS - P=1.2
NUZ=14 M**2/SEC - CORE=500 M - DOWNDRAFTS

RFLUX

Fig. 7.44 Grossman Stable 3rd Order/BL/P=1.2/
R=500 (Growth Rate, Phase Speed,
and Rflux)

GROSSMAN COMPOSITE (STABLE)

BL MOISTURE ACCESSION

JUN 1979 – 9TH ORDER LSQRS – P=1 0

NUZ=14 M**2/SEC – CORE=500 M – DOWNDRAFTS

σ_r

GROSSMAN COMPOSITE (STABLE)

BL MOISTURE ACCESSION

JUN 1979 – 9TH ORDER LSQRS – P=1.0

NUZ=14 M**2/SEC – CORE=500 M – DOWNDRAFTS

PHSPD

GROSSMAN COMPOSITE (STABLE)

BL MOISTURE ACCESSION

JUN 1979 – 9TH ORDER LSQRS – P=1.0

NUZ=14 M**2/SEC – CORE=500 M – DOWNDRAFTS

RFLUX

Fig. 7.45 Grossman Stable 9th Order/BL/P=1.0/
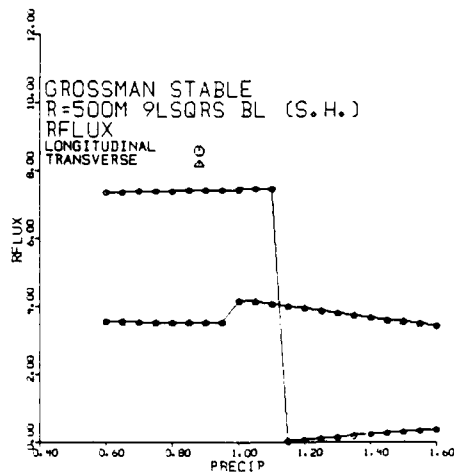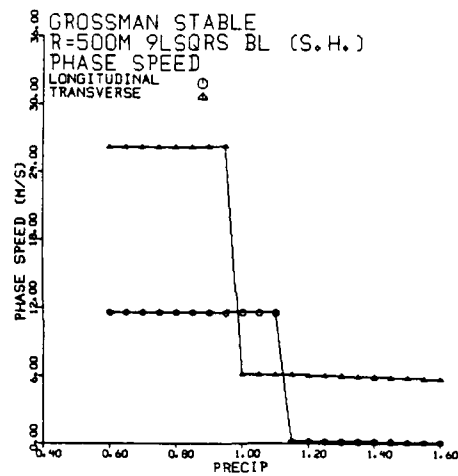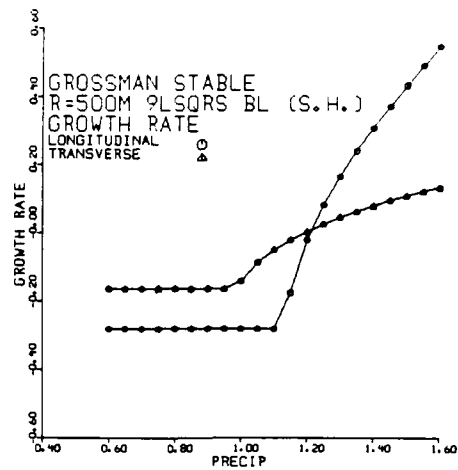R=500(Growth Rate, Phase Speed,
and Rflux)

Fig. 7.46 Individual Mode Behavior as f(P)

i. Critical "b"s for Individual Base States

By examining the individual mode behavior as the precipi-
tation efficiency or heating is increased, we may determine the
points of discontinuity or jumps associated with the transition
to a more "stationary" mode. The phase speed (relative to the
mean wind) is a good parameter for determination of the jump
point. Discontinuities are often present in the growth rates
and propagation frequencies. However, in some instances they
are not discernible.

Here, the critical "b" is defined as the value of precipi-
tation where the jump or discontinuity begins as P, the precip-
itation efficiency, is increased. Table 7.8 lists the jump
points for the base states for both longitudinal and transverse
modes. In four instances, no jump was discernible in any of
the analyzed variables. Some immediate conclusions may be
drawn from Table 7.8. First, in nine out of 12 instances, the
transition occurred first in the transverse mode relative to
the cloud layer shear. Second, jumps in the longitudinal modes
where P exceeded 1.0 tended to occur for deep convection cases.
In the one instance for a shallow or small core with net dry-
ing, downdrafts had shifted the normalized heating profiles to
higher levels within the cloud (see previous discussion). This
second observation seems consistent with Sun's (1978) results
although no discontinuity was discussed in his work.

However, what seems significant about these jumps is that

they are associated with a change in the character of the energy transfer and momentum fluxes. In Fig. (7.47), the change of sign for both the longitudinal and transverse modes' momentum fluxes is evident as the critical points (P=1.30 and P=.90, respectively) are surpassed. Furthermore, these changes in character of the transfers do not occur simultaneously over the wavenumber domain -- there seem to be lags between the transverse and longitudinal modes. Bear in mind these conclusions are based only on the relatively few runs shown in Table 7.8. A full investigation as the problem is currently constructed is very time-consuming from a computing standpoint. At least, the above is suggested by the initial results.

TABLE 7.8   CRITICAL Bs FOR BASE STATES

BASE	MA	LSQRS	R	LBc	TBc	DIFF
EAS	CD	3	1000	+.05	+.10	+.05
CAS	BL	3	500	+.05	+.35	+.30
GS	BL	9	500	+.20	.00	-.20
GSSH	BL	9	500	-.10	+.05	+.15
MO*	CD	9	1000	-.30	-.20	+.10
GC	CD	9	1000	-.30	-.35	-.05
MO	CD	3	1000	-.10	--	--
EAS	CD	9	1000	--	--	--
GS	BL	3	500	+.20	+.25	+.05
GC	CD	3	1000	-.30	+.10	+.40
CAS	BL	9	500	--	+.30	--
MO*	CD	9	1000	-.30	-.15	+.15
EASSH	CD	9	1000	--	-.10	--
EASSH	CD	3	1000	-.35	-.20	+.15
GC	BL	3	1000	-.25	-.25	0

* nuz=60 m**2/s

CD=cloud depth moisture accession

BL=boundary layer moisture accession

R=cloud radius in meters

GC=Grossman Convective

GS=Grossman Stable

EAS=Eastern Arabian Sea

MO=Monsoon Onset

CAS=Central Arabian Sea

--SH=sensible heat included in vertical heating profile

LBc=critical longitudinal; TBc=critical transverse
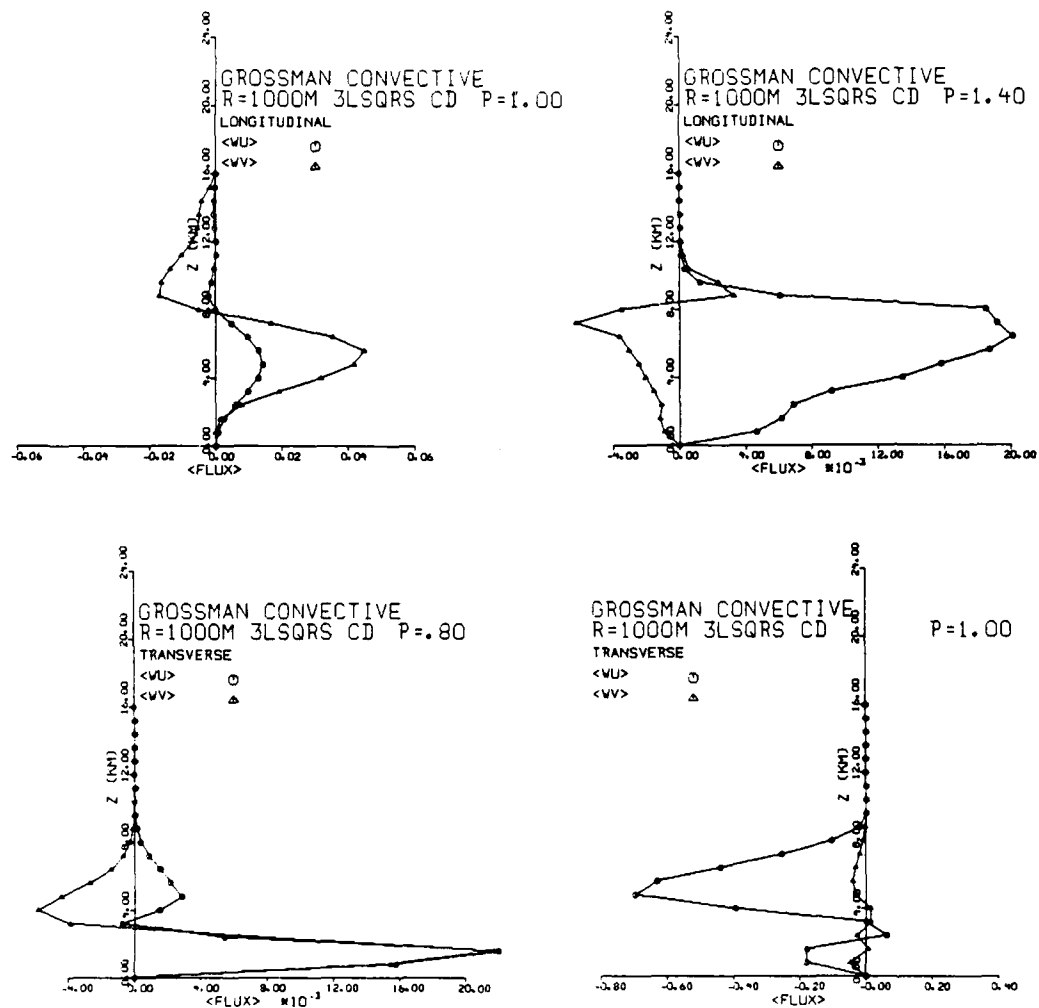
DIFF= TBc-LBc

Fig. 7.47 Momentum Fluxes Before and After Critical Point

j.   Updating Asai's Energy Flow Diagram

Asai (1970a) presented a diagram showing the energy flows for unstable perturbations (Fig. 7.48). The gist of this diagram is that while both transverse and longitudinal secondary circulations receive energy from the upward transport of heat (release of potential energy), the energy flow between the kinetic energy of the secondary circulation and the kinetic energy of the mean (base state) flow differs in sign depending on the mode. Specifically, the longitudinal mode receives energy from the mean flow while the transverse mode actually supplies energy to the mean flow. This result is rather striking.

Since both Asai's (1970) and the present study are posed as infinite domain horizontal boundary value problems (open, homogeneous boundary conditions as x, y --> ∞) we may study the transfer of energy between the large area-averaged base states and the smaller band -scale perturbations within the bounded fluid depth.

Employing the results from the linear model used in this study, we can fashion a similar diagram which is applicable to the monsoon base states studied here. Slight modifications will be made, however. Since unstable modes occur before as well as after the jump or critical point, the energy flows should be specified in both cases. Also, for both the longitudinal and transverse modes, it is useful to generalize the

relative magnitudes of the energy flow between each box before and after the jump.

In the initial case before the jump, both transverse and longitudinal modes show energy flow from potential to perturbation kinetic energy and from the mean kinetic energy to the perturbation kinetic energy. In both instances, $\langle P,K'\rangle$ dominated $\langle \bar{K},K'\rangle$. After the jump and increasing in trend as the precipitation efficiency increases, the longitudinal flow from mean to perturbation kinetic energy increases while the transfer of $\langle P,K'\rangle$, while still positive, decreases relative to $\langle \bar{K},K'\rangle$. For the transverse bands, a different situation exists after the jump. Here, $\langle P,K'\rangle$ increases relative to the magnitude of $\langle \bar{K},K'\rangle$. Furthermore, $\langle \bar{K},K'\rangle$ gradually reverses sign throughout the depth as subgrid moisture is increased, indicating energy transfer from the secondary circulation to the mean flow. One should note that for strong longitudinal stationarity, the supply of buoyant potential energy to the secondary circulation dominates the kinetic energy transfers for the transverse mode while the longitudinal mode secondary circulation is fed almost equally by both the potential energy release of the upward heat transport and the kinetic energy of the mean flow. This is consistent with the flux Richardson number distribution in the horizontal wavenumber domain.

Fig. 7.49 shows schematically the above conclusions as an update to Asai's 1970 diagram. Some of the individual mode behavior diagrams suggest a lag between the transverse and

longitudinal modes. In this case, one might speculate on the longitudinal mode behavior as being a response to the change in energy flow pattern which occurred at the lower jump point in the transverse mode.
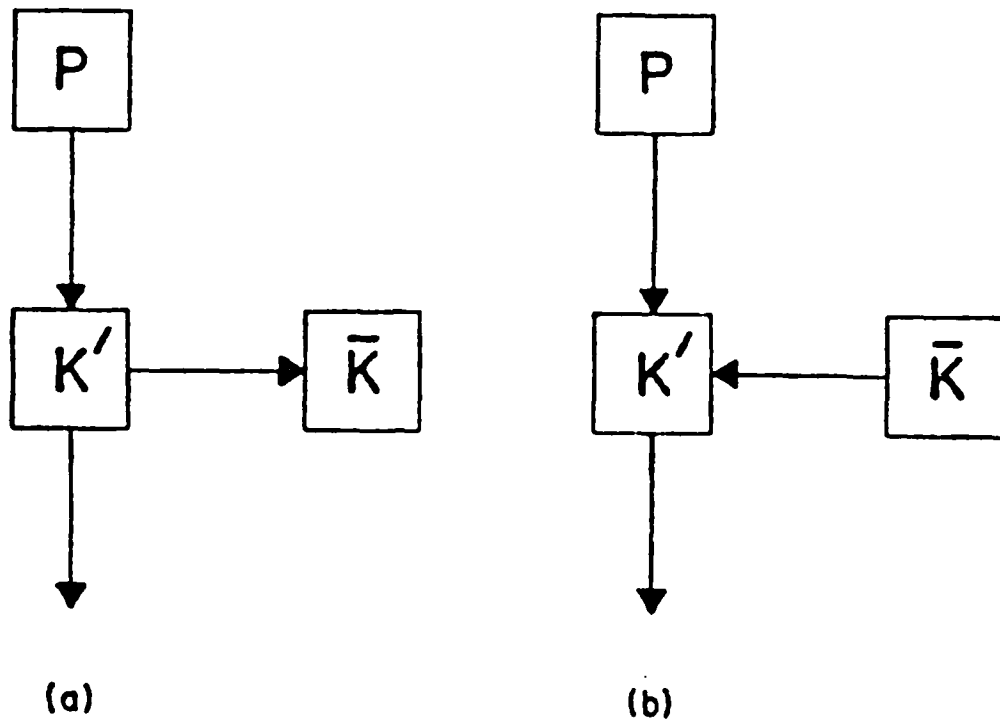
(a)   (b)

Fig. 11. Energy flow diagram for unstable per-
turbations. The arrows indicate the
direction of the transformations. (a)
transverse mode, (b) longitudinal mode.

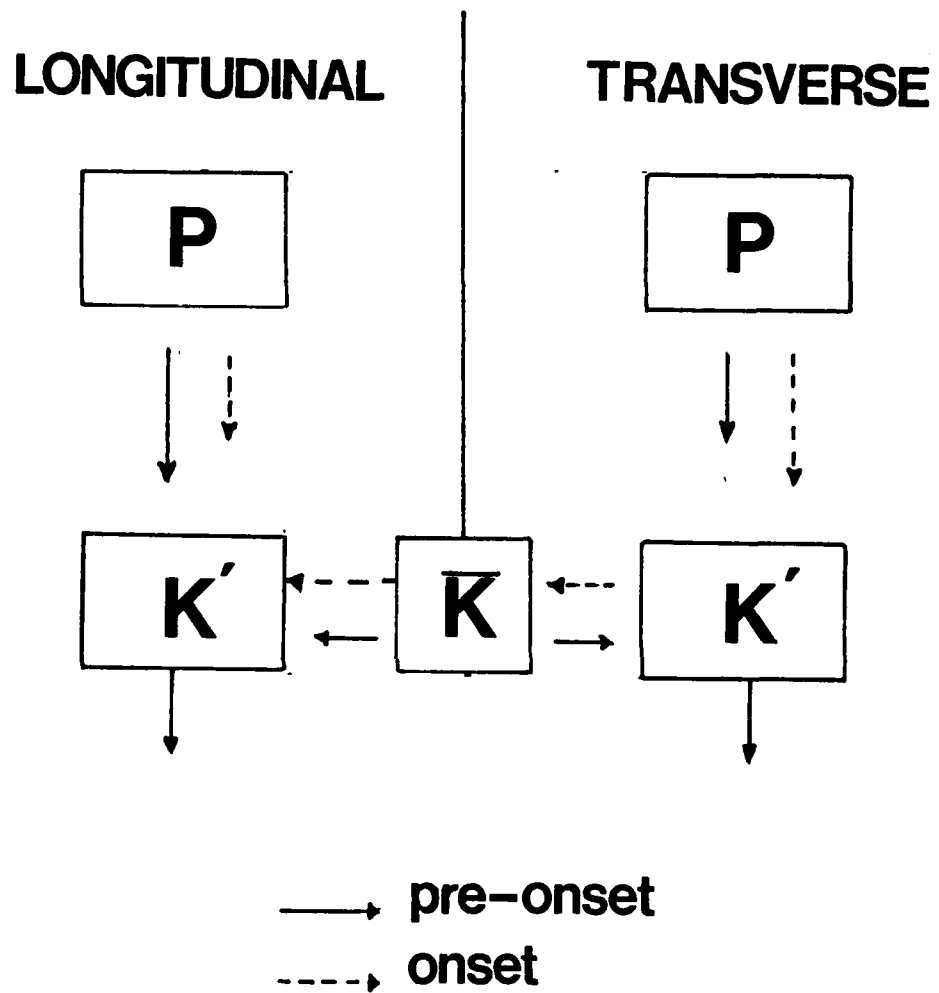Fig. 7.48 Energy Flow Diagram for Unstably-Stratified Fluid (Asai,
1970)

Fig. 7.49 Energy Flow Diagram for Monsoon Base States

VIII. Comparison of Results with Observations

A principle motivation for this study was the observa-
tional results of Benson and Rao (1987). They noted the
existence of several quasi-stationary (speed ~ 2 - 3 m/s) con-
vective bands in the eastern Arabian Sea. While the bands were
parallel to the low-level jet (oriented SW-NE), above 900 mb
the band tangential components were ~ 10 m/s. This was consid-
erably higher than the tangential components observed for the
GATE stationary bands. (Barnes and Sieckman, 1984).

a. Radar, Satellite, and Aircraft Photography

A major restriction on observing the orientation, struc-
ture, and movement of the Arabian Sea precipitation bands is
the lack of radar data during SMONEX. Some limited data were
obtained from the Bombay (19N 73E) S-band (10 cm) radar. While
this location is removed somewhat from the area of analyzed
soundings, some characteristic banding features were observed
offshore on 24 June 1979 (Fig. 8.1). For the PPI scope on 24
June (~202 UTC) with a range of 200 km, NE-SW banding is
clearly evident over the water with enlargement of the bands as
they extend over the land. Band spacing is about 25 km. Asso-
ciated RHI presentations (5 km height marker interval in fig.
8.2) suggest that these bands consist of deep (~5-10 km tall)
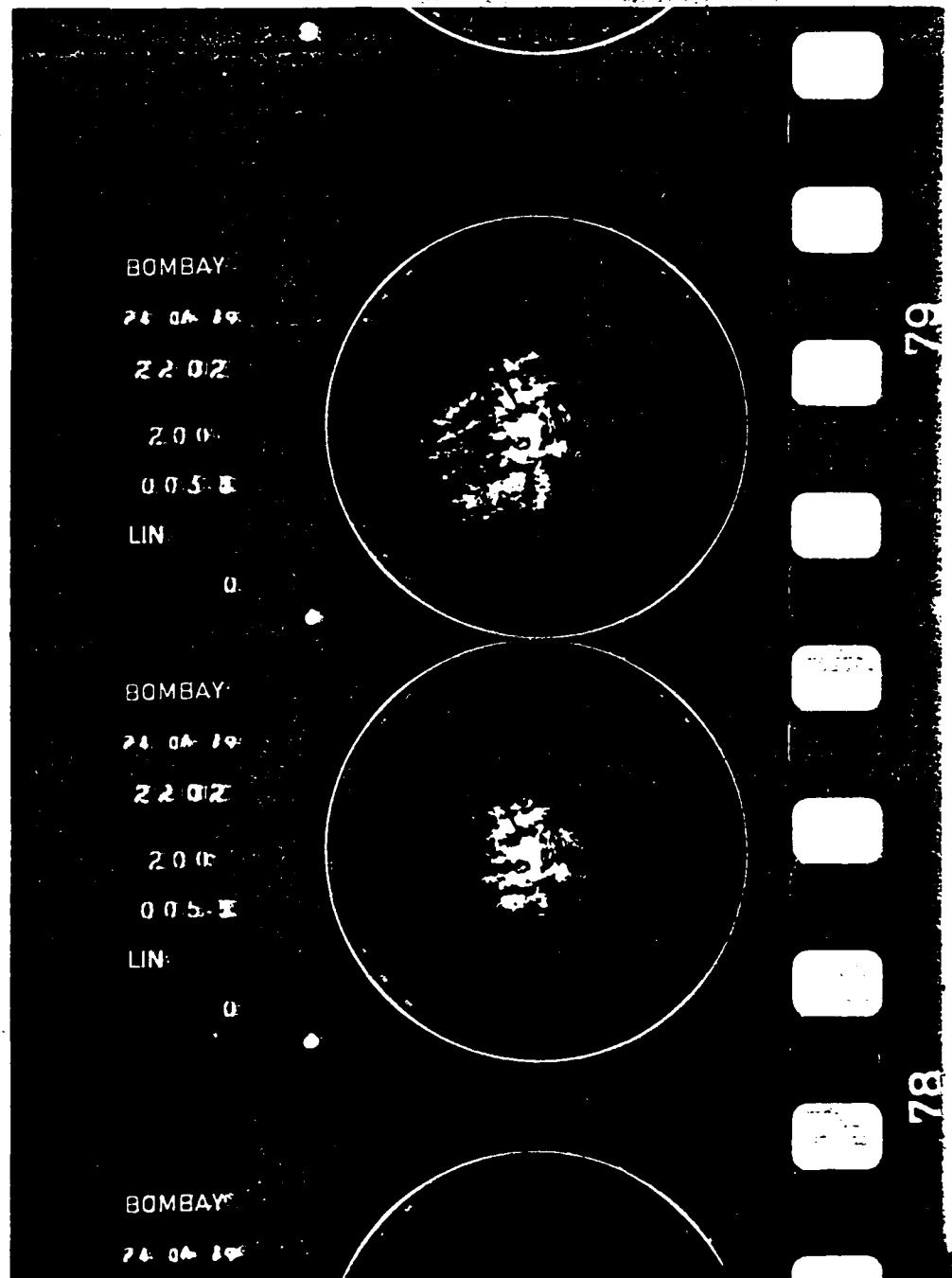precipitating shafts.

.

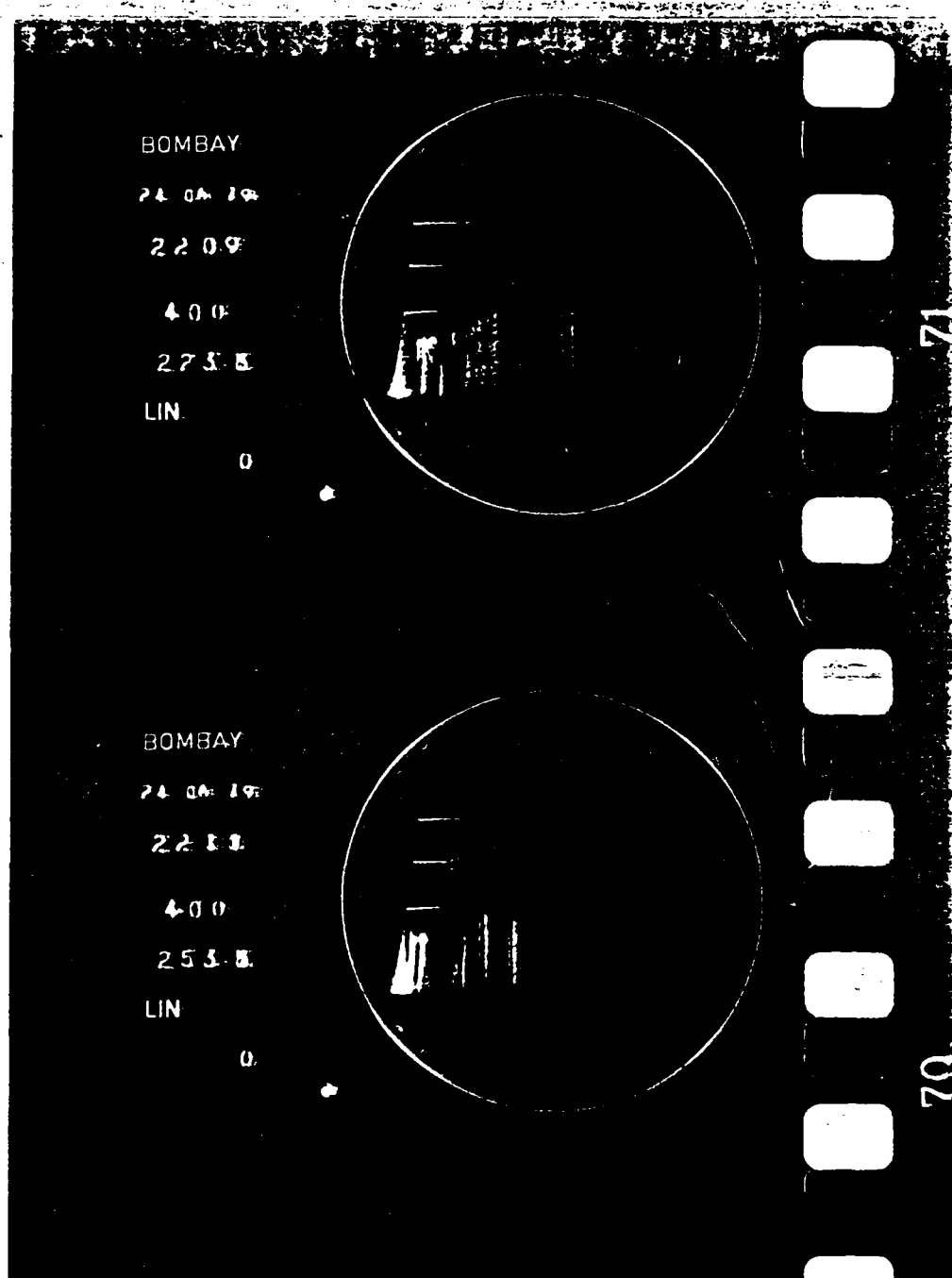Fig. 8.1 Bombay S-Band PPI - 24 June 1979 (Range = 200 km)

Fig. 8.2 Bombay S-Band RHI - 24 June 1979 (Range = 400 km)

Somewhat better satellite data exists. High resolution
DMSP visual data for a similar seasonal period but different
year (19 June 0451 UTC 1986, fig. 8.3) indicate deep convection
off the western coast of India. The imagery suggests an E-W
orientation for the deep convection bands. However, this is
difficult to determine with certainty since extensive cirrus
debris associated with the Tropical Easterly Jet may falsely
convey this impression. It is evident that to the north of
this convection area the shallow cumulus is aligned into E-W
rows. Another DMSP visual pass (20/0130 UTC June 1979, Fig.
8.4) indicates several protruding band tops near 11N 73E sug-
gesting alignment into E-W patterns. This is the same location
from which the dropsonde -Amini/east Arabian Sea composite
sounding for 20 June was taken. The estimated spacing of the
bands based strictly on cloud top data was about 40 km. The
corresponding IR image (not shown) confirms through the display
of warmer air temperatures between the clouds the band presence
and character. Towards the northwest near 15N 66E, the E-W
orientation of the more shallow cumulus is quite evident.
Additional evidence for E-W banding over the eastern Arabian
Sea is provided by DMSP IR imagery 24 June 0618 UTC (Fig. 8.6).
Again, the cold white tops stacked N-S and aligned E-W suggest
a more-or-less E-W band alignment. For the monsoon onset
period (12 June 1979) at 9N 66E 0100 UTC, DMSP IR imagery
(Fig. 8.5) does not provide a clear picture of band orienta-
tion. Large mesoscale convective complexes lie about 4 degrees
east and south of the sounding area near 9 N 66E. While the
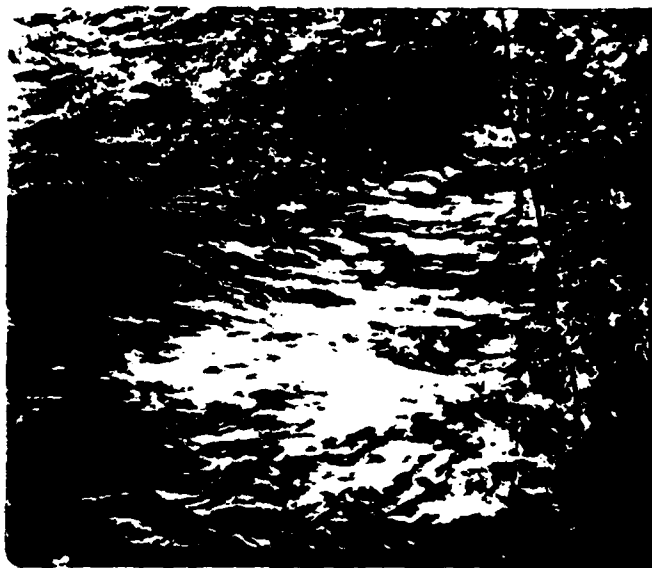
DMSP VISUAL 14 JUNE 1986 0451 UTC

Fig. 8.3 DMSP Visual 14 June 0451 UTC 1986
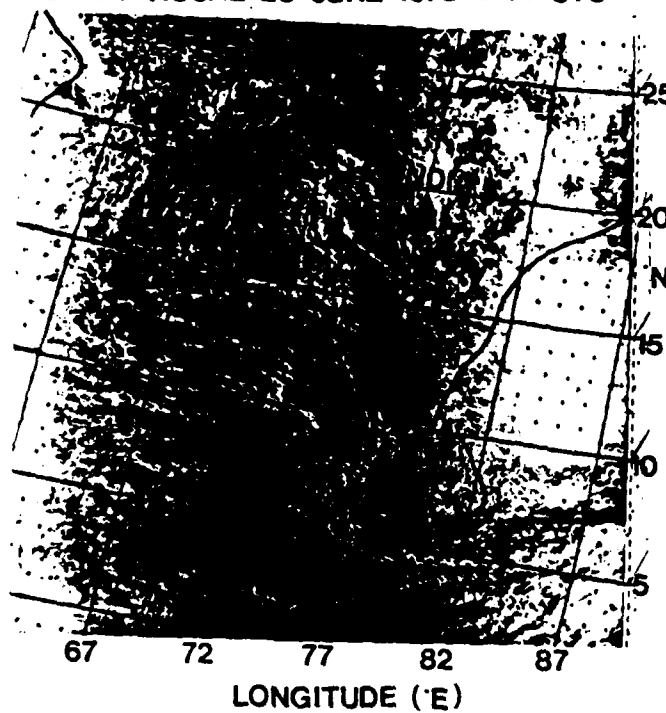
DMSP VISUAL 20 JUNE 1979 0130 UTC

Fig. 8.4 DMSP Visual 20 June 0130 UTC 1979
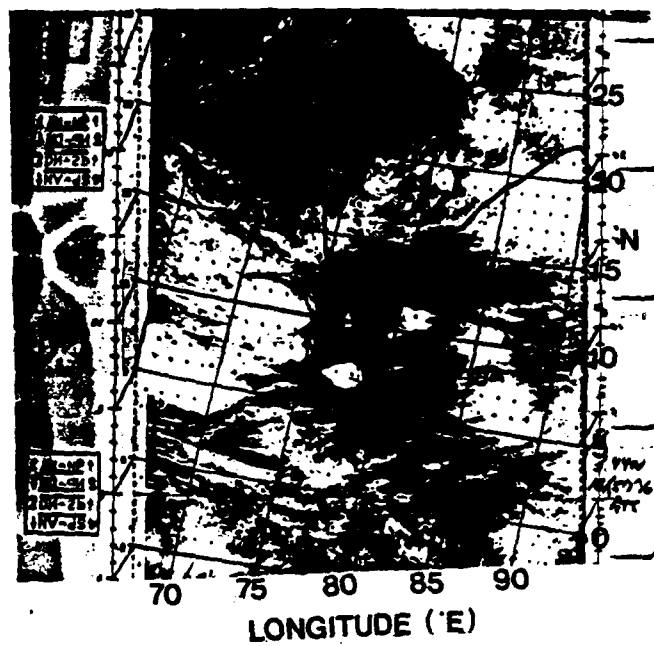
DMSP IR 12 JUNE 1979 0108 UTC

Fig. 8.5 DMSP IR 12 June 0108 UTC 1979

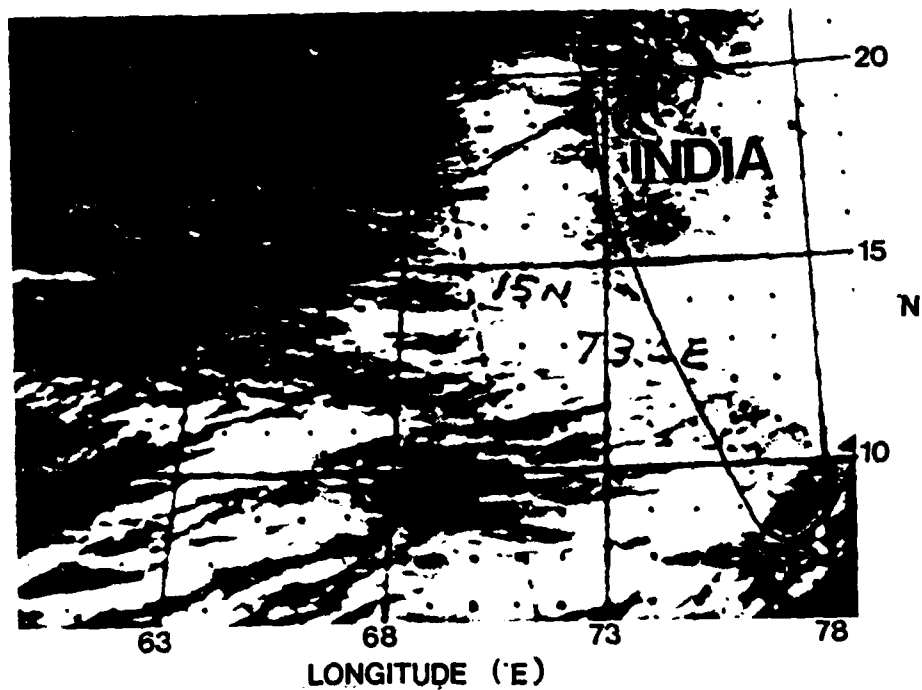**DMSP IR 24 JUNE 1979 0618 UTC**

Fig. 8.6 DMSP IR 24 June 0618 UTC 1979

convective alignment near Ship Volna hints at an E-W mode, transverse banding of convection is also suggested farther north near 20N 80E.

Although radar data was lacking and the usefulness of visual or infrared satellite imagery was limited for deep convection, the aircraft film provided a more reliable source of band orientation, depth, and, in some instances, spacing. High quality Ektachrome 16 mm movie film for both left side, right side, and nose cameras was taken by the NCAR Electra on the missions of 20 and 24 June. Similar movies were made by the NOAA P-3 research aircraft for the 24 June mission to the western Arabian Sea. These films have provided in-situ visual observations of the convective environment. Using a stop-action movie projector, Fujichrome (ISO 50) slide film was used to record the convective highlights as a function of location, aircraft altitude, aircraft heading, and time. In addition to height orientation and spacing of the clouds, the vertical tilt of the individual convective towers or cores could also be determined.

Fig. 8.7 from NOAA P-3 movies (13.5N 56.4E) on 24 June shows vividly both the shallow band orientation and spacing over the western Arabian Sea. Here, the cloud rows are oriented (025-205°) NNE-SSW with an estimated spacing of 5 km. Using other frames from a "sawtooth" run, the cloud top was estimated at 1100 m and cloud base ~ 900 m. Since these observed rows are parallel to the cloud layer shear, they are

211

longitudinal. Another example of NW-SE alignment near 8.2N 59.4E (Fig. 8.8) illustrates the increased vertical development as one proceeds southeastward from Fig. 8.7. However, farther north (16.4N, 55.6E, Fig. 8.9) and closer to the Arabian peninsula, the haze associated with a stronger inversion and a subsequent lack of cloud orientation is observed. Recalling the model results of Chapter VII, the linear model produced a transverse mode unless either (1) the cloud depth was increased beyond 300m or (2) the surface heat flux was increased. While the observed results contradict the linear results for the observed specification of cloud depth, they do, however, corroborate the trend --i.e. increased/decreased stability favors a transverse/longitudinal mode. Also, there is approximate agreement between observed (5 km) and computed (6-7 km) wavelength of the cloud rows. Fig. 8.10 (13.2 N 56.7E) shows the response of the sea surface to incredibly strong winds present near the surface in the western Arabian Sea beneath the longitudinal rows.

For the Central Arabian Sea (24 June) near ship Deepak (15.0N 65E), less detailed film of the convection is available. Fig. 8.11 (15.0N 67.5 E) indicates a stable region with a shallow convective band in the distance (tops ~4 km) oriented 070°/250° Another frame south of Deepak (Fig. 8.12; 13.9N 66.1E) shows somewhat deeper convection (tops ~6 km) with a similar orientation as the previous figure. With respect to the vertical orientation of the smaller convection, Fig. 8.13

Fig. 8.7 NOAA P-3 24 June 0851 UTC 13.5N 56.4E View toward 250°
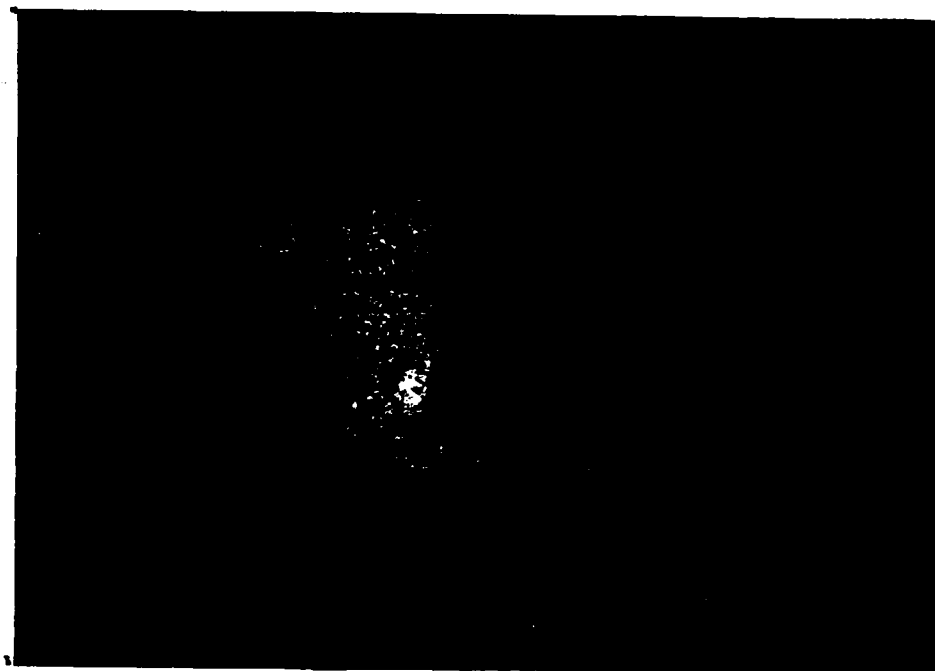

Fig. 8.8 NOAA P-3 24 June 1020 UTC 8.2N 59.4E View toward 070°

212

Fig. 8.9 NOAA P-3 24 June 0800 UTC 16.4N 55.6E View toward 238°

Fig. 8.10 NOAA P-3 24 June 0859 UTC 13.2N 56.7E View toward 071°

Fig. 8.11 NOAA P-3 24 June 1225 UTC 15.0N 67.5E View toward
141°

Fig. 8.12. NOAA P-3 24 June 1205 UTC 13.9N 66.1E View toward
140°

(16.4N 64.2E) suggests a lean of the weak shallow convective cores (tops ~ 1.6 km) towards the SSE (150°). A similar lean was computed for the lower portions (below 2.4 km) or the E-W oriented bands in the linear model.

For the eastern Arabian Sea in the vicinity of the Electra dropsonde (20 June 1979 06 UTC) near 11N 71E, extensive dense cirrus cover obscures visually many of the details of deep convection. However, some cursory features may be estimated. Fig. 8.14 (12.4N 71.3E) indicates a stable E-W cloud free "channel" just north of a band shelf with a weak cumulus line occurring as the BL is fed moisture from the surface. Fig. 8.15 (12.6N 71.3E) shows the north end of the channel and more young cumuli assisting the BL recovery. These two figures combined suggest a 36 km spacing between the lower cloud shelves associated with the bands. Also, extensive, high cirrostratus cover is present above the aircraft. Since the aircraft altitude is 5500 m in these figures, one may infer that the cirrostratus base is no lower than about 6 km.

Other imagery available from the P-3 runs and Electra runs showed in considerable detail the cloud tilt at various locations in the Arabian Sea. Fig. 8.16 (19.3N, 70.0E) suggests a strong tilt of cloud tops near 5 km towards the SSW. This is confirmed by other imagery near the same location. Farther west, Fig. 8.17 (19.8N 64.4E) indicates bands oriented 290°/110° with cloud tops ~ 3 - 4 km. Proceeding even farther west, Fig. 8.18 (19.3N 59.9E) indicates very shallow banding

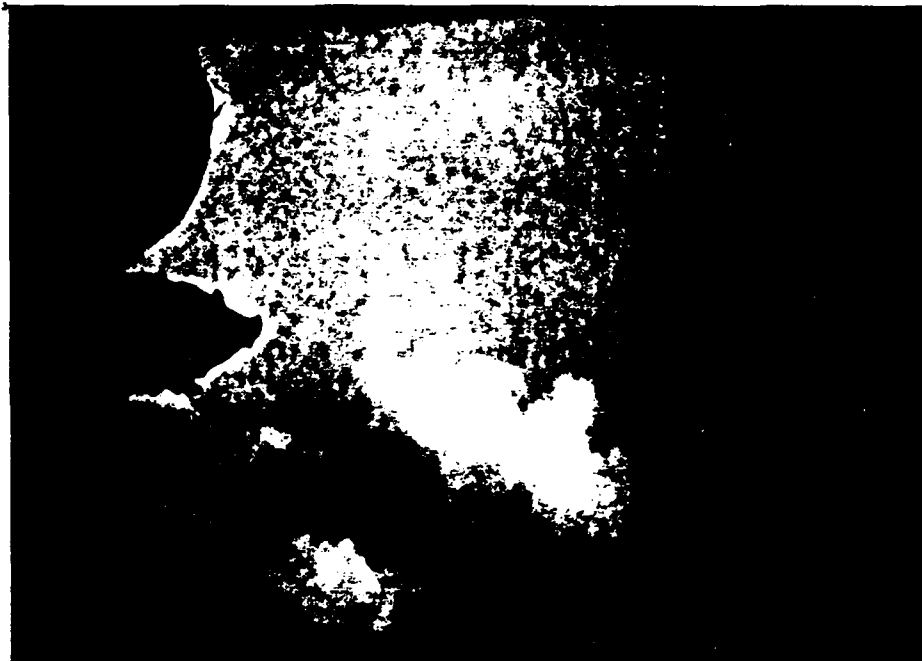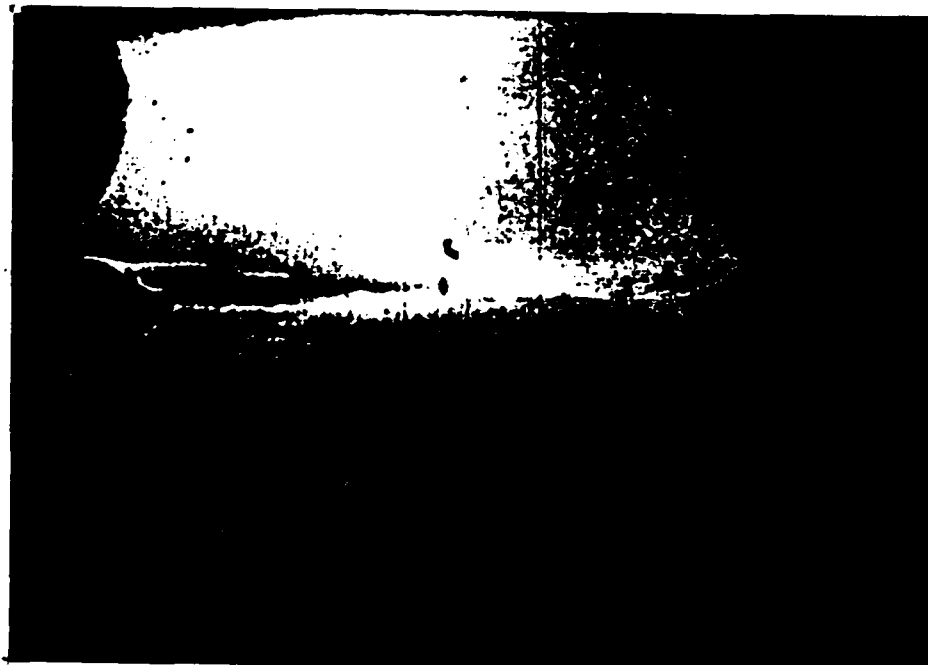Fig. 8.13. NCAR Electra 24 June 0811 UTC 16.4N 64.2E View toward 230°

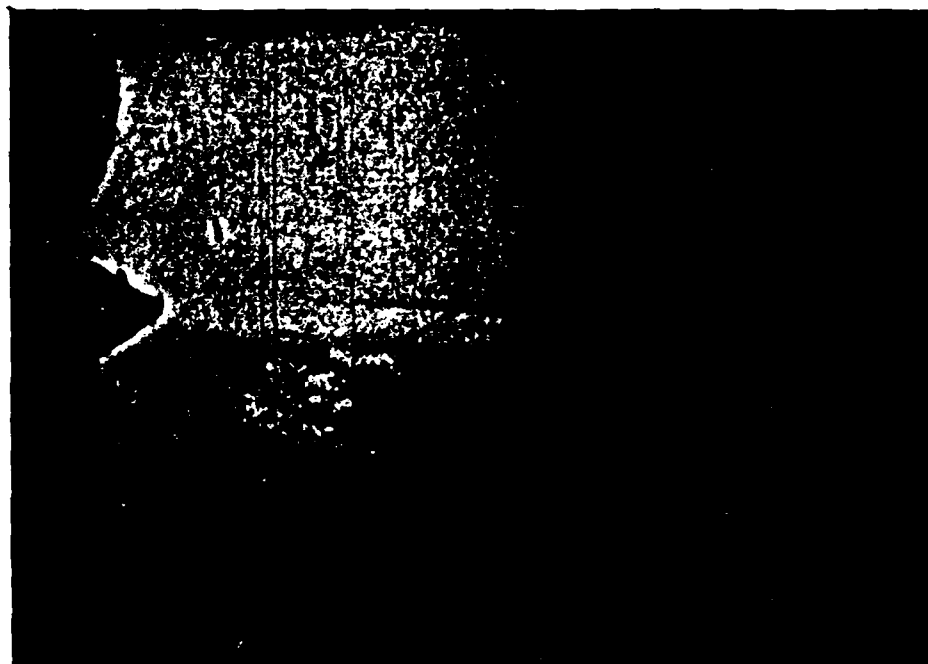Fig. 8.14. NCAR Electra 20 June 0526 UTC 12.4N 71.3E View toward 108°

Fig. 8.15. NCAR Electra 20 June 0521 UTC 12.6N 71.3E View toward 108°

Fig. 8.16. NOAA P-3 24 June 0520 UTC 19.3N 70.0E View toward 007°

217

Fig. 8.17. NOAA P-3 24 June 0620 UTC 19.8N 64.4E View toward
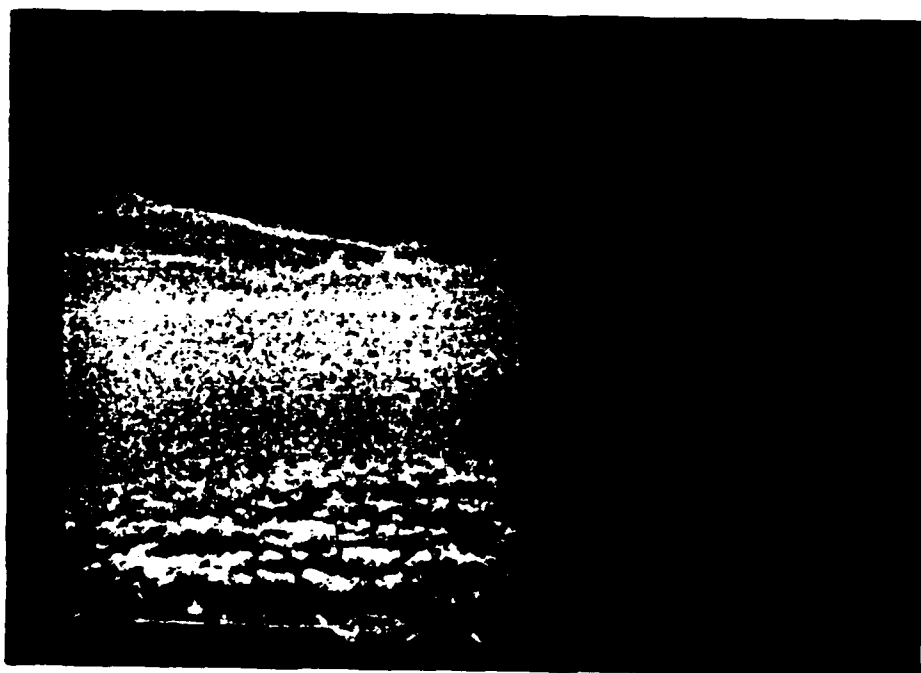006°

Fig. 8.18. NOAA P-3 24 June 0708 UTC 19.3N 59.9E View toward
258°

070°/250°) with cloud tops ~ 2 km. Fig. 8.19 (9.5N 61E) and Fig. 8.20 (10.4N 62E) on 24 June shows the increasing depth of cumulus (tops ~ 3 km) as one proceeds northeast into the Arabian Sea. The cumulus tilt is also quite dramatic --below 2 km a lean of SW-NE and above 2 km a lean in the opposite direction. This tilt is probably caused in part by the low level westerly jet. In the more disturbed area to the NE, Fig. 8.21 (17.7N 70.9E) exhibits a roughly E-W cloud line with cloud top tilted to the WSW (250°).

Using the Electra/P-3 movie film observations, a map on which cloud band orientation/tops are plotted can be constructed. From this map (Fig. 8.22), it is evident that a SW-NE band orientation is favored for the central and southern Arabian Sea. A NNE-SSW band orientation is favored for the western Arabian Sea. An E-W band orientation is favored for the eastern Arabian Sea and a NW-SE band orientation is favored for the moderately deep convection over the northern Arabian Sea. The orientation of the very deep bands over the eastern Arabian Sea are not readily determined from the movie film. An E-W orientation is suggested by the channels seen in the film. Benson and Rao (1987) imply that the deep band orientation is ~ 240/060° .

b. Verification of the Linear Model Results with Respect to Band Orientation and Vertical Tilt

This topic discussion will be by base state.

Fig. 8.19. NOAA P-3 24 June 1047 UTC 9.5N 61.0E View toward
139°

Fig. 8.20. NOAA P-3 24 June 1103 UTC 10.4N 62.0E View toward
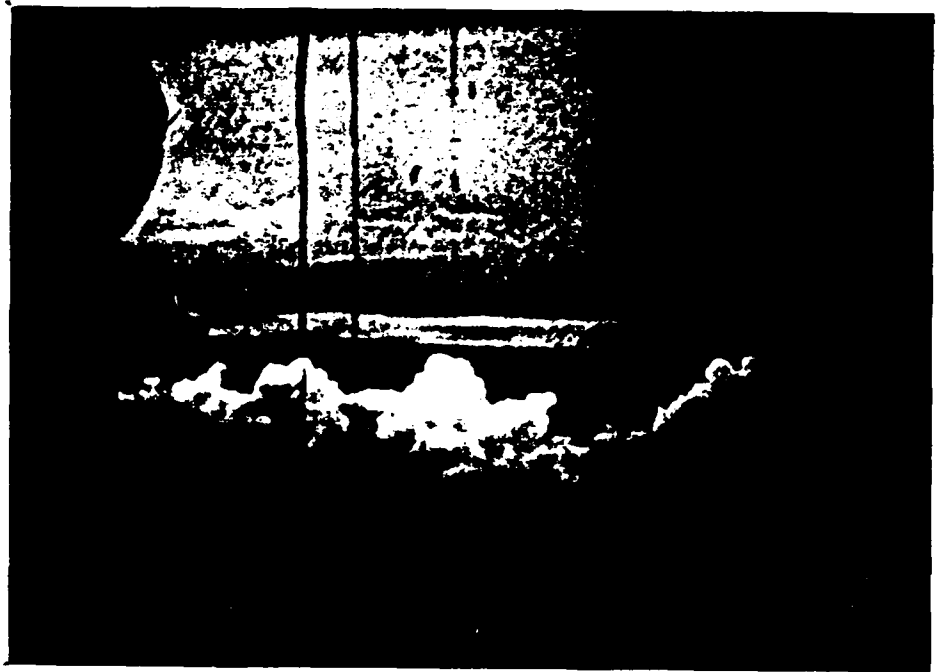140°

Fig. 8.21. NCAR Electra 24 June 0435 UTC   17.7N 70.9E   View toward 140°
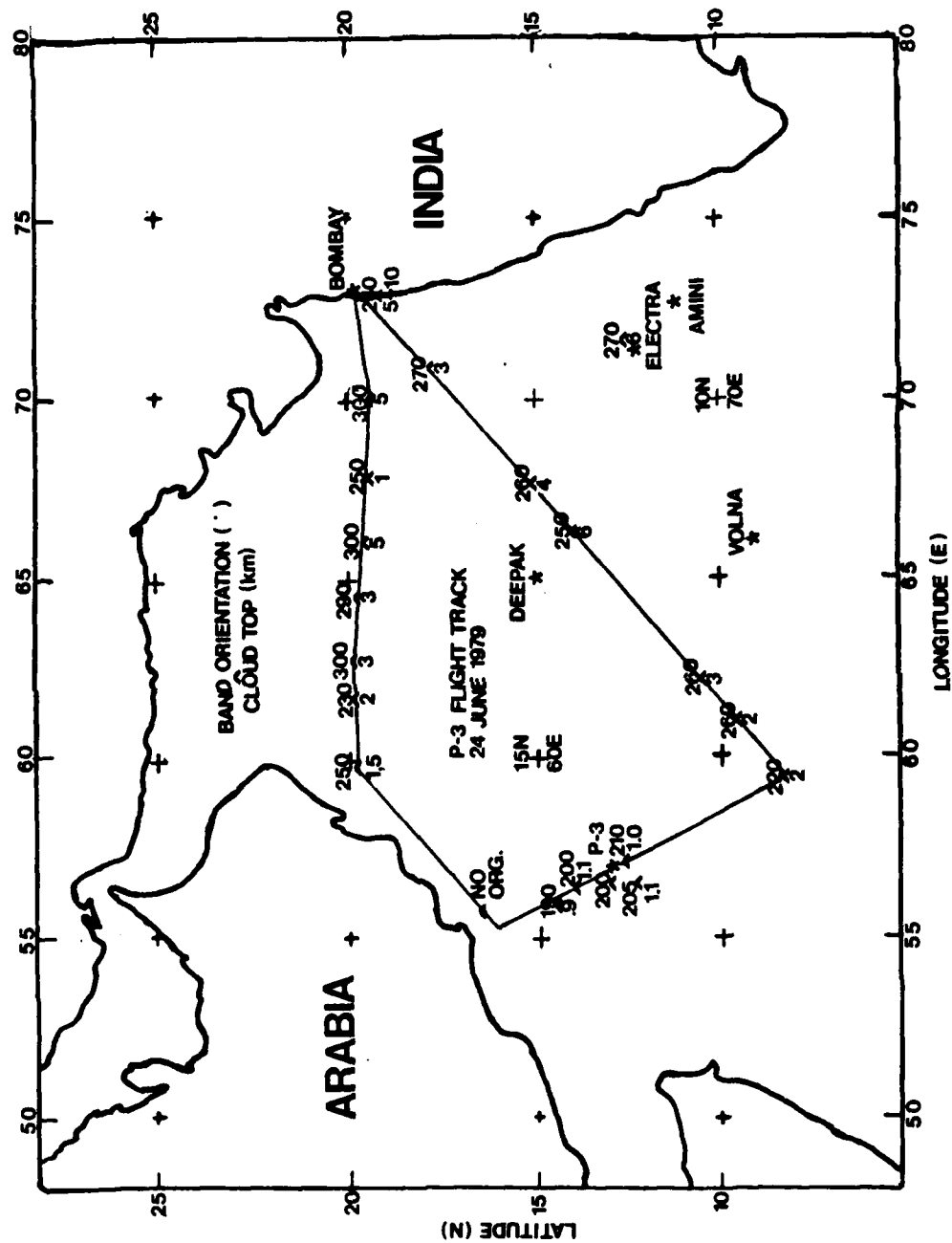
Fig. 8.22. Observed Cloud Band Orientation and Height for 24 June
1979 from P-3 film

(1) Western Arabian Sea

As noted above, all cloud rows observed south of 15N and west of 60E possessed a longitudinal orientation while the model diagnosed transverse orientations predominantly. The only longitudinal orientation produced by the model was for a 5 level (600 m deep cloud). This suggests the linear model underestimated the surface heat flux or the perturbation heating associated with the shallow cloud layer itself which seems essential for producing a longitudinal mode. In general, the model was 45-90° off of the observed orientation angles. The smallest discrepancy was for the 3rd order fit with only a 45° discrepancy. The observed cloud rows were almost exactly parallel to the cloud layer shear of the LaSeur composite (1981) wind profile at 13N 57E which was used as the base state for these model runs.

The (observed from an elevation of 1000 m) cloud tilt was from north to south. The vertical velocity eigenfunctions associated with a NW-SE longitudinal mode showed only a slight tilt towards the north. The temperature, relative vorticity, and U fields all suggested a tilt towards the south, however.

(2)   Central Arabian Sea

The distinguishing feature of the linear model response to the Central Arabian Sea base state was (1) its suppression of growth for bands associated with larger core radii and (2) its favoring transverse modes for all wind fits and even with

enhanced precipitation efficiency (P > 1.0). While there were
no band observations in the immediate vicinity of Deepak,
observations of bands ~ 100-200 km east and south of Deepak
showed band orientation about 070/250° and parallel to the
cloud layer shear. However, these observations were for some-
what deeper clouds (6 and 4 km estimated tops). Aircraft
observations near 16N 64E suggest cloud tops are ~1.5 km agree-
ing more with the results of the one dimensional cloud model.
While band spacing or orientation is difficult to observe, Fig.
8.13 observed at 16.4N 64.2E shows a 1.6 km top leaning
strongly towards the SSW. This agrees with the linear model
results for both longitudinal and transverse modes.

The momentum fluxes and energy transfers were computed for
the Central Arabian Sea for some dominant modes using the
linear model. For relatively shallow bands (tops ~ 3 km) aug-
mented by sub-grid scale moisture convergence (P=1.25) W^*U and
W^*V have strong maxima in the cloud layer and both are posi-
tive. For the transverse modes, W^*U is positive but W^*V is
strongly negative for the cloud layer. The energy transfer
from the mean to secondary flow is positive while the transfer
of buoyant energy to the secondary flow is also positive. Con-
versely, $\langle \overline{K}, K' \rangle$ is negative for the transverse mode in the
cloud layer. Hor (1988) using fast response aircraft tur-
bulence measurements reported an up-scale kinetic energy
conversion (i.e. $\langle \overline{K}, K' \rangle < 0$) in the Central Arabian Sea cloud
bands. In the linear model, such a transfer is associated with

the dominant transverse bands (Chapter VII, Fig. 7.10).

Hor also discussed the up-gradient momentum transfer; i.e. does K theory require the eddy viscosity coefficient to be negative? He noted that the $\overline{u'w'}$ (transverse band-parallel momentum flux) profile was up-gradient in the Central Arabian Sea. We see that for the linear model in the transverse mode, the band parallel fluxes $\overset{*}{W}V$ are up-gradient in the cloud layer while the band normal fluxes $\overset{*}{W}U$ are down-gradient. The model results are in disagreement with LeMone's (1983) observations which show band perpendicular momentum fluxes to be up-gradient. However, the linear results here apply more to convection in an incipient or formative stage while LeMone's results are applicable to observed deep convective lines. For longitudinal modes, both $\overset{*}{W}U$ and $\overset{*}{W}V$ are down-gradient in the cloud layer.

In summary for the central Arabian Sea, the linear model produces down-gradient momentum transfer and energy from the mean flow feeding the secondary flow for longitudinal modes. For transverse modes, the band-parallel momentum transfer is up-gradient and the large-scale flow is receiving kinetic energy from the secondary circulations. Assuming these results are applicable to the observational area, Hor's observational analyses suggest transverse modes are dominant in the vicinity of ship Deepak on 24 June.

(3) Eastern Arabian Sea

As discussed earlier, satellite imagery from the 20th as well as radar data show the eastern Arabian Sea is dominated by E-W deep cloud band patterns which are parallel to the deep cloud layer shear vector. The linear model results agree roughly with the observed orientation and spacing of bands provided sufficient moisture and a relatively smooth (low order polynomial) wind profile are fed into the model. Even in the case of non-augmented moisture and high detail wind profiles, longitudinal but propagating waves are produced by the model.

Hor (1988) contrasted the observed momentum flux and energy transfers of the eastern Arabian Sea with those of the central Arabian Sea. For the EAS, the $\overline{u'w'}$ momentum flux was up-gradient only below 3 km. Furthermore, $\langle \overline{K}, K' \rangle$ was positive in the eastern Arabian Sea cloud bands. Results of the linear model for a smooth wind profile (3rd order fit) and augmented moisture accession (P=1.20) show distinct differences between the longitudinal and transverse modes. For the longitudinal mode, computations of $\overset{*}{W}U$ show a strong down-gradient momentum flux through the depth. For the transverse mode, $\overset{*}{W}U$ is strongly up-gradient through 6.4 km. This is contrasted with $\overset{*}{W}V$ in the central Arabian Sea (transverse band parallel) which was up-gradient in the cloud below 3 km (Fig. 8.23).

The computed energy transfers of $\langle P,K' \rangle$ for both longitudinal and transverse modes showed transfer in the cloud depth
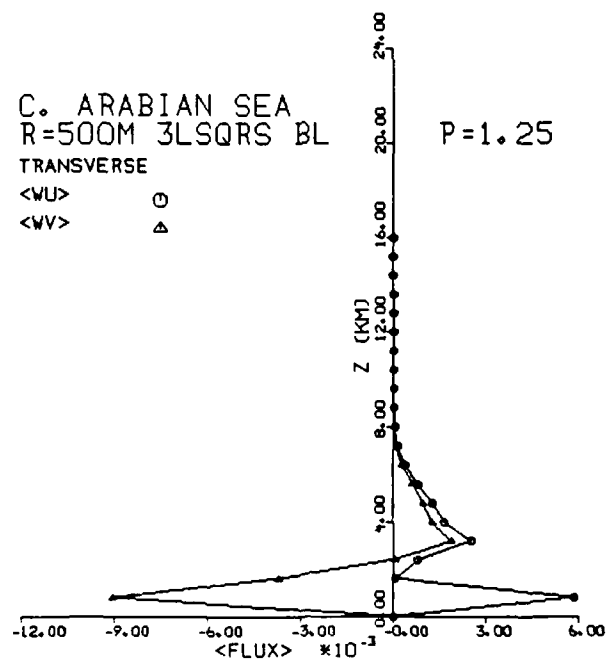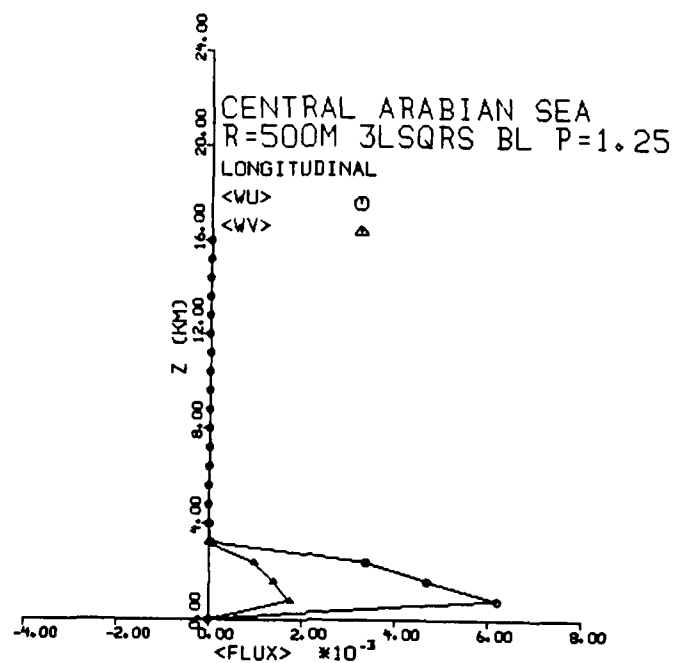
Fig. 8.23. C.A.S. Longitudinal and Transverse Mode Momentum
Fluxes

227

228

from the buoyant energy to the secondary flow. For the transverse mode, the $\langle P,K'\rangle$ term is more dominant relative to the $\langle \overline{K},K'\rangle$ term, however. More significantly, a shift in sign of $\langle \overline{K},K'\rangle$ occurs between longitudinal and transverse modes. For the longitudinal modes, $\langle \overline{K},K'\rangle$ is positive through the fluid depth except for near zero values at the surface and 4.8 km. However, the transverse mode shows $\langle \overline{K},K'\rangle$ negative from the surface through 5.6 km. Hor noted that above 3 km, $\langle \overline{K},K'\rangle$ was positive for the EAS bands. Since satellite data and previous studies suggest dominant longitudinal modes, and considering Hor's observation of transfers of kinetic energy from the base state to the perturbed flow for bands over the E. Arabian Sea, we may consider the analytical model results a further confirmation of longitudinal mode dominance in this area.

As a final note, the Grossman convective composite with Ogura wind for the same base state settings (3LS CD R=1000) produces similar results for the energy transfer and momentum fluxes when applicable features are compared to the EAS convective base state.

IX.   Summary and Conclusions
                    .

        This study has investigated the response of a linearized

system of anelastic perturbation equations to diabatic forcing

as well as wind profiles and temperature profiles consistent

with base states found during the Arabian Sea monsoon. The

diabatic forcing or convective heating has been determined

using a steady-state cloud model-based cumulus parameterization

scheme (Anthes, 1977). Wind and temperature profiles have been

determined from rawinsonde, dropwindsonde, and composite sound-

ings developed by other researchers (Grossman and Durran,

1984). Least squares curves of varying orders have been fit to

the u, v profiles. Potential temperature profiles have been

adjusted to eliminate super-adiabatic layers. Estimates of

eddy viscosity were provided by the one-dimensional steady

state (1DSS) cloud model.   A one-dimensional time-dependent

(1DTD) non-linear cloud model was used as a check of the 1DSS

microphysical formulation and deep convection potential.

        The linear system was written for 21 equally-spaced levels

in the vertical and solved as the generalized complex eigen-

value problem ($A\bar{x} - \sigma B\bar{x} = 0$). The primary algorithm used for

solution was the LZ algorithm (Kaufman, 1975) which requires

complex operands.   The QZ algorithm (Garbow, 1978) which

employs programmed complex arithmetic on real operands was also

tested and produced virtually identical results for   the

229

eigenvalues of a given base state over a wide range of diabatic forcing. Non-dimensional output from the model runs included growth rates, oscillation frequencies, and eigenfunctions over a mesoscale horizontal wavenumber domain. In addition, diagnostic techniques including the correlation theorem were used to compute perturbation variables such as pressure, horizontal divergence, and Reynolds fluxes. Energy transfers between the base state and secondary flows were computed using standard definitions (Brown, 1970, Asai, 1970, and Chandrasekhar, 1961). A flux Richardson number was then computed (Asai, 1970, Sun, 1978) using the moduli of these results.

Two methods of moisture accession in the linear model were employed. One method (Ooyama, 1964 and Syono and Yamasaki, 1966) involved coupling the vertical velocity at cloud base with the available boundary layer moisture supply. An argument for this method is that deep convection is fed primarily by the mass flux from the well-mixed boundary layer and into the convective towers above. The other method (Molinari, 1985) considered the vertically-integrated moisture accession over the entire cloud depth by multiplying the vertical velocity with the base state specific humidity vertical gradient. This is analogous to the vertical moisture advection term and has been cited as being closely related to the observed rainfall rate (Kuo and Anthes, 1984; Krishnamurti et al., 1983). A similar approach may also be derived from the anelastic perturbation continuity equation for moisture.

The normalized convective heating profiles are determined
by using a Kuo-type parameterization scheme developed by Anthes
(1977). Lateral entrainment as a function of cloud core radius
is considered in both the driving cloud model and the condensa-
tion rate determination. Sensible heat transports incorporat-
ing the effects of convective towers on their environment and
adjacent moist downdrafts are included in the manner suggested
by Kuo and Raymond (1980) using data provided by the 1DSS cloud
model. Thus in this cumulus parameterization scheme, the
determination of the cloud size or spectrum of clouds is criti-
cal to the vertical distribution of heating.

Non-precipitating shallow convection is parameterized
using the Betts (1973) two layer scheme for shallow trade
cumuli. In this procedure, the model vertical velocity is cou-
pled with a hypothetical distribution of lapse rate within a
pre-determined cloud layer such that the mean cloud layer lapse
rate is equivalent to the base state lapse rate. A sign rever-
sal between upper and lower layers of the vertical velocity
distribution produces the desired results --i.e., warming in
the lower half and cooling in the upper half such that the
thermal perturbations associated with the shallow clouds are
simulated.

Estimates of vertical diffusion coefficients for the
linear model are determined from the 1DSS model using a
Smagorinsky-type deformation formula (Cotton, 1975) for isotro-
pic diffusion. Assumptions of this method are that the

232

estimates are valid for the central convective core towers and the vertically-averaged vertical velocities are equivalent to the vertical velocities of the 1DSS cloud model. This latter assumption is supported by Simpson (1971) who describes the 1DSS vertical velocities and other in-cloud variables as mean properties of the active tower as it rises through the cloud model level. This diffusion coefficient method estimation allows for a crude linkage between the cloud characteristics, the base state thermodynamic properties, and the linear model. Perhaps an even more important assumption is the 100:1 horizontal to vertical diffusion ratio (Priestley, 1962; Agee, 1975). This assumption assists the short wave cut-off and introduces smoothness and order into the band growth rates defined in the wave number domain.

Surface heat fluxes are incorporated for the shallow non-precipitating convection by specifying a surface temperature perturbation in terms of a cloud base (or higher) temperature perturbation (Haltiner, 1967) and then employing this perturbation in a bulk formula which includes a surface wind speed differential.

All computations on the MASSCOMP (double precision) and Cray (single precision) used 64 bit length words to minimize round-off error.

a.   Summary of Results

The following summarizes the most important results of the linear model runs.

k domain results:

1) Augmented moisture supply (P >1.0) appears necessary for stationary longitudinal bands to develop in the model when deep convection is favored. However, propagating longitudinal modes can occur when b is greater than or equal to 0.

2) Growth rates of deep convective modes are favored by cloud depth moisture accession. Conversely, boundary layer moisture accession favors the growth of stationary but not so deep bands.

3) For an E-W shearing flow (no turning with height), the inclusion of a low level westerly jet considerably enhances the dominance of the stationary longitudinal mode for both deep and shallow convection relative to the transverse mode.

4) Stationary longitudinal modes, whether shallow or deep, are associated with a minimum of Richardson flux in the wave number domain.

5) The linear model suppresses growth for bands with large core radii (>1000 m) for more stable base states but favors growth for large core radii for more convectively unstable base states.

6) The ground-relative phase speed tends to become non-dispersive in the wave number domain once the stationary longitudinal mode is fully established.

7) High order polynomial (9th order) flow turning with height establishes more than one significant mode in the wavenumber domain for deep moisture-augmented convection. This does not preclude the formation of a dominant stationary mode.

8) For base state settings which produce a stationary E-W longitudinal mode, SW-NE oriented bands possess a phase speed directed (relative to the mean flow) towards the SE. NW-SE oriented bands have a phase speed directed towards the NE.

9) For the dominant modes, eigenfunctions with the largest mean moduli favor the transverse modes especially at larger wavelengths. An exception to this rule is the U eigenfunction whose greatest amplitudes are associated with long wavelength ($\tilde{}$100 km) E-W modes.

10) For shallow non-precipitating convection in the w. Arabian Sea as parameterized, a 300 m deep cloud establishes a dominant transverse mode.

11) Increasing the shallow cloud depth or including surface heat flux strengthens the longitudinal mode and its stationarity.

12) Varying the vertical eddy diffusion adjusts the dominant mode wavelength and growth rate but does not seem to alter the

"character" of the eigenvalue pattern or eigenfunction structure.

13) However, decreasing the horizontal/vertical diffusion ratio towards isotropy significantly alters the eigenvalue fields in the k domain in addition to eliminating the short wave cut-off.

--Individual Mode Behavior

14) The inclusion of sensible heat transports in the convective parameterization scheme delays the onset of the stationary longitudinal mode but slightly advances the onset of the transitive transverse modes.

15) For an E-W shearing flow (no turning with height), the inclusion of a low level westerly jet (LLWJ) for deep convection (top=9.6 km) delays the growth of the transverse mode relative to the longitudinal mode.

16) With the onset of the stationary longitudinal mode (usually after the transverse modes), distinct jumps (drops or increases) occur in the flux Richardson number and phase speed magnitudes for all modes.

17) The observed drop in the longitudinal mode flux Richardson number at the onset of the stationary mode is associated with a small drop in the transfer of potential energy to kinetic energy of the secondary flow and an increase in the transfer of mean to perturbation kinetic energy.

18) As heating or precipitation efficiency is increased, the transverse modes' flux Richardson number (Rflux) either increases or is steady --primarily due to a decrease or steadiness in the mean to secondary flow kinetic energy transfer.

19) For turning shear flows in deep convection, high detail wind profiles (9th order) delay the onset of (or prevent) the stationary longitudinal mode dominance. Hence, smoother wind profiles for deep convection enhance stationary longitudinal mode dominance.

20) In all cases, increased precipitation efficiency or heating past a certain critical point reduces sharply longitudinal and to a lesser extent, transverse mode phase speed relative to the mean wind. In the case of the transverse mode, however, the phase speed may be temporarily increased at the jump discontinuity.

21) For the one case examined, doubling the vertical diffusion does not shift the onset of the stationary mode. Also, the assumption of isotropy in the diffusion coefficients does not shift the onset of the stationary mode.

--Vertical Profile of Cross-Correlation Quantities for Individual Modes

22) After the onset of stationarity, $\langle \bar{K}, K' \rangle$ is greatly reduced or becomes negative (i.e. the mean flow receives energy from the secondary flow) for the transverse modes. However, $\langle \bar{K}, K' \rangle$

tends to increase for the longitudinal mode relative to $\langle P,K'\rangle$ as the precipitation efficiency and stationarity increase.

23) Conversely, $\langle \dot{P},K'\rangle$ --the transfer of potential energy to perturbation kinetic energy decreases relative to $\langle \overline{K},K'\rangle$ for the stationary longitudinal mode but increases relative to $\langle \overline{K},K'\rangle$ for the transverse mode as convective heating is increased. Items (21) and (22) explain the behavior of the flux Richardson number over the wave number domain as a stationary longitudinal mode is established.

24) For deep convective base states characterized by dominant stationary longitudinal modes, $\overset{*}{W}U$ momentum flux is predominantly down-gradient for the longitudinal mode but strongly up-gradient for the transverse modes. For the less deep convective cases examined, $\overset{*}{W}U$ is down-gradient predominantly in both the longitudinal and transverse modes. The former result is in agreement with LeMone's (1983) observations but the latter result for shallow transverse (N-S) modes is not in agreement with her results. Dudhia and Moncrieff (1987) in their numerical simulation of a stationary longitudinal band observed that the momentum transport is primarily down-gradient thus agreeing with the linear model results for deep convection.

25) For the transverse mode, $\overset{*}{W}U$ changes sign abruptly (down-gradient to up-gradient) at the onset of the phase speed and flux Richardson number jumps.

--Eigenfunction Cross-Sections

26) D (divergence) and P (pressure) eigenfunctions are in phase for stationary longitudinal modes and 90° out-of-phase for transverse modes and transitive longitudinal modes.

27) Likewise, W and T eigenfunctions are approximately in-phase for stationary longitudinal modes but 90° out-of-phase for the other dominant modes.

28) Deep convective base states generate a mid-layer (~8 km) U maximum for stationary longitudinal modes. If a low level jet is present in the base state, a lower level (~3.2 km) U maximum is also produced.

29) For weaker convection or transverse modes, divergence and P field maxima are lifted above the surface. For stationary longitudinal modes, both D and P maxima lie at or are "attached" to the surface.

30) Stationary longitudinal modes, especially w.r.t. the W eigenfunction, are erect --i.e., they display little phase tilt with height.

31) W and Z eigenfunctions are 90° out-of-phase for longitudinal modes but 180° out-of-phase for transverse modes.

32) For the western Arabian Sea shallow non-precipitating convection, the more longitudinal modes possess roots at the surface in D and P. The transverse modes are characterized by

relatively weak roots or eigenfunctions in the subcloud layer with no roots (divergence maxima) at the surface.

33) "Noisy" θ eigenfunctions for deep convection are common. This may be due to inclusion of a non-smooth theta base state vertical profile. Such noise also tends to be characteristic of the stationary mode.

Other less tangible observations are in order, also. First, BL moisture accession for deep convection introduces a smoothness and elongation along a particular wave number in the growth rate field. Meanwhile, the BL accession growth rate fields for stationary convection align in a decidedly more non-dispersive pattern (along the wave number angle radius) than the cloud depth accession even though both methods tend in that direction.

Also these results suggest it is possible if sufficient heating is shifted to the upper part of the cloud (say through sensible heat transports) to have a dominant stationary mode form in the presence of a detailed shear profile. This is seen in EAS (SH 9 CD 1000) where stationarity vigorously begins at P=1.0 in the transverse mode. Hence, the transverse mode, while favored by upper level heating, is not always a transitive or propagating mode.

c. Finis

In summary, this study has shown the critical influence of

convective parameterization, moisture accession, and base state wind on the linear system results. The convective parameterization is especially crucial since the all-important vertical distribution of heating is sensitive to the microphysical and cloud dynamical characteristics --areas of limited knowledge. The limitation of a 1DSS cloud model in simulating these factors --especially ice phase behavior and the subsequent dynamic response is well known (Orville, 1986). However, the great merit of the 1DSS approach is that they are useful predictors of cloud top height for protected cores (Cotton, 1986) which is a fundamental requirement for Kuo-type scheme closures. The response to the method of moisture accession was shown to be quite sensitive to the cloud depth of a particular environment. The concept of a moist mass flux across an invisible membrane produced strong growth for smaller core radii in relatively stable base states but could not sustain high growth for the larger core radii with higher tops. Also, a noticeably dominant longitudinal mode as observed by Benson and Rao (1987) for deep convection seems facilitated by CD moisture accession.

The inclusion of wind was varied by polynomial order. In previous studies, "smooth" profiles have often been used (e.g. Raymond, 1975). Some data analysis texts recommend in practice using no higher than a 5th order fit. In practice, the base state wind profile determination is a subjective argument --the best fit determination should be made based upon review of the available fits consistent with the wind "representative" of the

convective area and convection depth. However, it seems necessary to include sufficient detail (high enough order) that significant peaks such as the low- level westerly jet are resolved as demonstrated by the dramatic response of the Grossman Stable composite.

Also, if one were to attempt a similar problem in the future, I would recommend attempting to fit the base state potential temperature profiles with a polynomial before insertion into the linear model. This perhaps might reduce the "noise" (frequent change in sign with height) of the θ eigenfunction for the propagating modes. However, compatibility with the cloud model profile which uses the "raw" sounding would have to be resolved. Another by-product of this study is that carefully formulated 1DSS cloud models should probably be a regular tool of tropical sounding analysis --given their skill in predicting cloud top height and minimal computing overhead.

As this study has evolved, it becomes readily apparent that the most important factor is the determination of the critical point "b" --the value of moistening (or drying) at which the stationary mode onsets. In turn, this is highly dependent on the cumulus parameterization scheme and the vertical heating profile. The behavior of the eigenfunctions and their phase relationships at and in the vicinity of the critical point should be further investigated. Also, the determination of appropriate cumulus parameterizations will require

extra effort and study for as long as they are required.

The most surprising results were the minimum of flux Richardson number associated with the stationary longitudinal mode and the sharp discontinuity in the flux Richardson number and phase speed fields as heating is increased for a particular mode. While the onset of stationarity in linear theory has been shown to be discontinuous by Chandrasekhar (1961) with respect to Nusselt number as a function of Rayleigh number, this topic does not seem prevalent in the meteorological literature. The results presented here strongly confirm Asai's (1970) hypothesis concerning energy transfers between the base state and secondary flows. In addition, these results suggest that the achievement of Asai's hypothesis may be represented by a three stage process -- pre-onset, transition, and onset phases where the transition phase is the lag between the transverse and longitudinal jump conditions. The model also qualitatively simulated the correct phase speed direction as observed by Benson and Rao if a SW-NE band is oriented counter-clockwise of the cloud depth shear vector. Implications also exist concerning the interaction of the cumulus tower scale and cloud band scale behavior. Since feedback from the band scale to the tower scale is not allowed here, any discussion would be purely speculative. However it is evident that deeper cloud cores may enhance a mode's stationarity and growth rate under certain base states in the linear model. The further investigation of important factors such as the role of

the surface downdrafts and their feedback on convective band behavior will require investigation of finite amplitude convection by a nonlinear numerical time integration.

.

BIBLIOGRAPHY

Agee, E. M., 1975: Some inferences of eddy viscosity associated with instabilities in the atmosphere. J. Atmos. Sci., 32, 642-645.

Anthes, R. A., 1977: A cumulus parameterization scheme utilizing a one- dimensional cloud model. Mon. Wea. Rev., 105, 270-286.

Asai, T., 1970a: Three-dimensional features of thermal convection in a plane Couette flow. J. Meteor. Soc. Japan, 48, 18-29.

Asai, T., 1970b: Stability of a plane parallel flow with variable vertical shear and unstable stratification. J. Meteor. Soc. Japan, 48, 128-138.

Asai, T., 1972: Thermal instability of a shear flow turning the direction with height. J. Meteor. Soc. Japan, 50, 525-532.

Asai, T., and A. Kasahara, 1967: A theoretical study of the compensating downward motions associated with cumulus clouds. J. Atmos. Sci., 24, 487-496.

Barnes, G. M., and K. Sieckman, 1984: The environment of fast- and slow- moving tropical mesoscale convective lines. Mon. Wea. Rev., 112, 1782-1794.

Benson, C. L., and G. V. Rao, 1987: Convective bands as structural components of an Arabian Sea cloud cluster. Mon. Wea. Rev., 115, 3013-3023.

Betts, A. K., 1973: Non-precipitating cumulus convection and its parameterization. Quart. J. R. Meteor. Soc., 99, 178-196.

Bevington, P. R., 1969: Data Reduction and Error Analysis for the Physical Sciences. McGraw-Hill, St. Louis, 336 pp.

Brigham, E. O., 1974: The Fast Fourier Transform. Prentice-Hall, Englewood Cliffs, N.J., 252 pp.

Brown, R. A., 1970: A secondary flow model for the planetary boundary layer. J. Atmos. Sci., 27, 742-757.

Chandrasekhar, S., 1961: Hydrodynamic and Hydromagnetic Stability. Dover, New York, 652 pp.

Chang, C. P., and R. T. Williams, 1974: On the short-wave

cutoff of CISK. J. Atmos. Sci., 31, 830-833.

Charney, J. G., and A. Eliassen, 1964: On the growth of the hurricane depression. J. Atmos. Sci., 21, 68-75.

Cotton, W. R., 1972: Numerical simulation of precipitation development in supercooled cumuli --Part II. Mon. Wea. Rev., 100, 764-784.

Cotton, W. R., 1975: On parameterization of turbulent transport in cumulus clouds. J. Atmos. Sci., 32, 548-566.

Cotton, W. R., 1986a: Testing, implementation, and evaluation of seeding concepts -- a review. Precipitation Enhancement - A Scientific Challenge. R. Braham, Jr., Ed., Amer. Meteor. Soc., 139-149.

Cotton, W. R., 1986b: Averaging and the parameterization of physical processes in mesoscale models. Mesoscale Meteorology and Forecasting. P. S. Ray, Ed., Amer. Meteor. Soc., 614-635.

Das, P., 1964: Role of condensed water in the life cycle of a convective cloud. J. Atmos. Sci., 21, 404-418.

Doos, B. R., 1962: The influence of exchange of sensible heat with the earth's surface on the planetary flow. Tellus, 14, 133-147.

Dudhia, J., and M. W. Moncrieff, 1987: A numerical simulation of quasi-stationary tropical convection bands. Q. J. R. Meteor. Soc., 113, 929-967.

Emmanuel, K. A., 1988: The maximum intensity of hurricanes. J. Atmos. Sci., 45, 1143-1154.

Eymard, L., 1985: Convective organization in a tropical boundary layer: an interpretation of doppler radar observations using Asai's model. J. Atmos. Sci., 42, 2844-2855.

Frank, W. M., 1983: The cumulus parameterization problem. Mon. Wea. Rev., 111, 1859-1871.

Frank, W. M., 1987: Tropical cyclone formation. International Workshop on Tropical Cylones, Univ. of Chicago Press, 53-90.

Fritsch, J. M., 1986: Modification of mesoscale convective weather systems. Precipitation Enhancement -- A Scientific Challenge. R. Braham, Jr., Ed., Amer. Meteor.

Soc., 77-86.

Garbow, B. S., 1978: Algorithm 535 The QZ algorithm to solve the generalized eigenvalue problem for complex matrices. ACM Trans. Math. Software, 4, 404-410.

Garbow, B. S., Boyle, J. M., Dongarra, J. J., and C. B. Moler, 1977: Matrix Eigenvalue Routines -- EISPACK Guide Extension. Lecture Notes in Computer Science. Springer-Verlag, Heidelberg.

Gerald, C. F., and P. O. Wheatley, 1985: Applied Numerical Analysis. Addison-Wesley, Reading, Mass., 579 pp.

Grossman, R. L., and D. R. Durran, 1984: Interaction of low-level flow with the western Ghat Mountains and offshore convection in the summer monsoon. Mon. Wea. Rev., 112, 652-672.

Haltiner, G. J., 1967: The effects of sensible heat exchange on the dynamics of baroclinic waves. Tellus, 19, 183-198.

Haltiner, G. J., 1971: Numerical Weather Prediction. John Wiley, New York, 317 pp.

Holt, T., and S. SethuRaman, 1985: Aircraft and ship observations of the mean structure of the marine boundary layer over the Arabian Sea duing MONEX 79. Bound. Layer Meteor., 33, 259-282.

Hor, T. H., 1988: Momentum Transport in Monsoon Convective Cloud Bands -- Observed and Simulated. Ph.D. dissertation, St. Louis University, 189 pp.

Kaufman, L., 1975: Algorithm 496 The LZ algorithm to solve the generalized eigenvalue problem for complex matrices. ACM Trans. Math. Software, 1, 271-281.

Koss, W. J., 1976: Linear stability analysis of CISK-induced disturbances: Fourier component eigenvalue analysis. J. Atmos. Sci., 33, 1195-1222.

Krishnamurti, R., 1975: On cellular cloud patterns. Part 3: Applicability of the mathematical a laboratory models. J. Atmos. Sci., 107, 1373-1383.

Krishnamurti, T. N., S. Low-Nam, and R. Pasch, 1983: Cumulus parameterization and rainfall rates II. Mon. Wea. Rev., 111, 815-828.

Kuettner, J. P., 1971: Cloud bands in the earth's atmosphere.

Observations and theory. Tellus, 23, 404-425.

Kuo, H. L., 1963: Perturbations of plane Couette flow in stratified fluid and origin of cloud streets. Phys. Fluids, 6, 165-211.

Kuo, H. L., 1965: On formation and intensification of tropical cyclones through latent heat release by cumulus convection. J. Atmos. Sci., 22, 40-63.

Kuo, H. L., 1974: Further studies of the parameterization of the influence of cumulus convection on large-scale flow. J. Atmos. Sci., 31, 1232-1240.

Kuo, H. L., and W. H. Raymond, 1980: A quasi-one-dimensional cumulus cloud model and parameterization of cumulus heating and mixing effects. Mon. Wea. Rev., 108, 991-1009.

Kuo, H. L., and K. L. Seitter, 1985: Instability of shearing geostrophic currents in neutral and partly unstable atmospheres. J. Atmos. Sci., 42, 331-345.

Kuo, Y. H., and R. A. Anthes, 1984: Semiprognostic tests of Kuo-type cumulus parameterization schemes in an extratropical convective system. Mon. Wea. Rev., 112, 1498-1509.

LaSeur, N. E., 1981: The structure of a well-developed Somali jet. International Conference on Early Results of FGGE and Large Scale Aspects of its Monsoon Experiment., Tallahassee, Fla., 12-59 – 12-62.

LeMone, M. A., and E. J. Zipser, 1980: Cumulonimbus vertical velocity events in GATE. Part I: diameter, intensity, and mass flux. J. Atmos. Sci., 37, 2444-2457.

LeMone, M. A., 1983: Momentum Transport by a Line of Cumulonimbus. J. Atmos. Sci., 40, 1815-1834.

LeMone, M. A., G. M. Barnes, and E. J. Zipser, 1984: Momentum flux by lines of cumulonimbus over the tropical oceans. J. Atmos. Sci., 41, 1914-1932.

Levine, J., 1959: Spherical vortex theory of bubble-like motion in cumulus clouds. J. Meteor., 16, 653-662.

Lilly, D. K., 1962: On the numerical simulation of buoyant convection. Tellus, 14, 148-171.

Lin, Y. J., R. G. Hughes, and R. W. Pasken, 1987: Subcloud-

layer kinematic and dynamic structures of a microburst-producing thunderstorm in Colorado determined from JAWS dual-doppler measurements. Bound. Layer Meteor., 39, 67-86.

Lindzen, R. S., 1974: Wave-CISK in the tropics. J. Atmos. Sci., 31, 157-179.

Lipps, F. B., 1971: Two-dimensional numerical experiments in thermal convection with vertical shear. J. Atmos. Sci., 28, 3-19.

McBride, J. L., and W. M. Gray, 1980: Mass divergence in tropical weather systems Paper II: large-scale controls on convection. Quart. J. R. Meteor. Soc., 106, 517-538.

Malkus, J. S., and H. Riehl, 1964: Cloud structures and distributions over the tropical Pacific Ocean. Tellus, 16, 275-287.

Mak, M., 1981: An inquiry on the nature of CISK. Part I. Tellus, 33, 531-537.

Mak, M., 1983: On moist quasi-geostrophic barotropic instability. J. Atmos. Sci., 40, 2349-2367.

Mathur, M. B. 1975: Development of banded structures in a numerically simulated hurricane. J. Atmos. Sci., 32, 512-522.

Meyer, W. D., and G. V. Rao, 1985: Structure of the monsoon low-level flow and monsoon boundary layer over the east central Arabian Sea. J. Atmos. Sci., 42, 1929-1943.

Molenkamp, C. R., 1968: Accuracy of finite-difference methods applied to the advection equation. J. Appl. Meteor., 7, 160-167.

Ogura, Y., 1964: Frictionally-controlled, thermally-driven circulations in a circular vortex with application to tropical cyclones. J. Atmos. Sci., 21, 610-621.

Ogura, Y., and T. Takahashi, 1971: Numerical simulation of the life cycle of a thunderstorm cell. Mon. Wea. Rev., 99, 895-910.

Ogura, Y., and M. Yoshizaki, 1988: Numerical study of orographic- convective precipitation over the eastern Arabian Sea and the Ghat Mountains during the summer monsoon. J. Atmos. Sci., 45, 2097-2122.

Ooyama, K., 1964: A dynamical model for the study of tropical cyclone development. Geofis. Intern., 4, 187-198.

Ooyama, K., 1969: Numerical simulation of the life cycle of tropical cyclones. J. Atmos. Sci., 26, 3-40.

Orville, H. D., 1986: A review of dynamic-mode seeding of summer cumuli. Precipitation Enhancement - A Scientific Challenge. R. Braham, Jr., Ed., Amer. Meteor. Soc., 43-62.

Pielke, R. A., 1984: Mesoscale Meteorological Modeling. Academic Press, Orlando, 612 pp.

Priestley, C. H. B., 1962: The width-height ratio of large convection cells. Tellus, 14, 123-124.

Pruppacher, H. R., and J. D. Klett, 1978: Microphysics of Clouds and Precipitation. D. Reidel, Boston, 714 pp.

Rao, Y. P., 1976: The southwest monsoon. Indian Meteorological Department Monograph 1/1976. Indian Meteorological Department, 367 pp.

Rao, G. V., and A. W. Hassebrock, 1972: Mesoscale latent heat release and its influence on mid-tropospheric warming. J. Appl. Met., 11, 1271-1283.

Ray, D., 1965: Cellular convection with nonisotropic eddys. Tellus, 17, 434-439.

Raymond, D. J., 1975: A model for predicting the movement of continuously propagating convective storms. J. Atmos. Sci., 32, 1308-1317.

Roadcap, J. R., and G. V. Rao, 1986: Features of thermals in stable wake and neutral stratifications in the disturbed monsoon boundary layer. Bound. Layer Meteor., 36, 133-148.

Rosenthal, S. L., 1979: The sensitivity of simulated hurricane development to cumulus parameterization details. Mon. Wea. Rev., 107, 193-197.

Rosmond, T. E., 1973: Mesoscale cellular convection. J. Atmos. Sci., 30, 1392-1409.

Simpson, J., 1971: On cumulus development and one-dimensional models. J. Atmos. Sci., 28, 449-455.

Simpson, J., and V. Wiggert, 1969: Models of precipitating

cumulus towers. Mon. Wea. Rev., 97, 471-489.

Simpson, J., and V. Wiggert, 1971: 1968 Florida cumulus seeding experiment: numerical model results. Mon. Wea. Rev., 99, 87-117.

Srivastava, R. C., 1967: A study of the effect of precipitation on cumulus dynamics. J. Atmos. Sci., 24, 36-45.

Stark, P. A., 1970: Introduction to Numerical Methods. MacMillan, New York, 334 pp.

Stark, T. E., 1976: Wave-CISK and cumulus parameterization. J. Atmos. Sci., 33, 2383-2391.

Stephens, D. E., and R. S. Lindzen, 1978: Tropical Wave-CISK with a moisture budget and cumulus friction. J. Atmos. Sci., 35, 940-961.

Sun, W. Y., 1978: Stability analysis of cloud streets. J. Atmos. Sci., 35, 466-483.

Sun, W. Y., 1984: Rainbands and symmetric instability. J. Atmos. Sci., 41, 3412-3425.

Sun, W. Y., 1987: Mesoscale convection along the dryline. J. Atmos. Sci., 44, 1394-1403.

Syono, S., and M. Yamasaki, 1966: Stability of symmetrical motions driven by latent heat release by cumulus convection under the existence of surface friction. J. Atmos. Sci., 44, 353-375.

Tamin, R., 1988: Microphysical structure of monsoon clouds during summer MONEX 1979. M.S. Thesis. St. Louis University, pp. 189.

Wang, B., 1987: The nature of CISK in a generalized continuous model. J. Atmos. Sci., 44, 1411-1426.

Wang, B., and A. Barcilon, 1986: Moist stability of a baroclinic zonal flow with conditionally unstable stratification. J. Atmos. Sci., 43, 705-719.

Weinstein, A. I., 1970: A numerical model of cumulus dynamics and microphysics. J. Atmos. Sci., 27, 246-255.

Xu, Q., 1988: A formula for eddy viscosity in the presence of moist symmetric instability. J. Atmos. Sci., 45, 5-8.

Xu, Q., and J. H. Clark, 1984: Wave CISK and mesoscale

convective systems. <u>J</u>. <u>Atmos</u>. <u>Sci</u>. <u>41</u>, 2089-2107.

Yamasaki, M., 1984: Dynamics of convective clouds and 'CISK' in vertical shear flow --with its application to easterly waves and squall-line systems. <u>J</u>. <u>Meteor</u>. <u>Soc</u>. <u>Japan</u>, <u>62</u>, 833-863.

.

VITA AUCTORIS

John Russell Roadcap was ███████████████████████████ ████████████████ He graduated from Varina High School near Richmond in 1972. He attended Virginia Polytechnic Institute from 1972-1974 and Florida State University from 1974-1976 where he received a B.S. in Meteorology. Upon graduation, he was commissioned a 2nd Lt. in the U.S. Air Force. From 1976-1979 he was assigned to Air Force Global Weather Central (Omaha) and was stationed at Kadena Air Base, Okinawa, Japan from 1979-1981. From 1981-1982 he was enrolled in the meteorology program at St. Louis University under the auspices of the Air Force Institute of Technology (AFIT) and received a Master's in Professional Meteorology in 1983. From 1983-1986 he was assigned to Eglin Air Force Base, Florida. He entered the Ph.D. program at St. Louis University under AFIT sponsorship in 1986. He attained his present rank of Major in November 1987.

Major Roadcap is a member of the American Meteorological Society.